NASA TECHNICAL NOTE

NASA TN D-4284

NASA TN D-4284

THE EXPLORER XXIII MICROMETEOROID SATELLITE

DESCRIPTION AND RESULTS FOR THE PERIOD NOVEMBER 6, 1964, THROUGH NOVEMBER 5, 1965

Compiled by Robert L. O'Neal

Langley Research Center
Langley Station, Hampton, Va.

NATIONAL AERONAUTICS AND SPACE ADMINISTRATION • WASHINGTON, D. C. • JUNE 1968

CONTENTS

THE EXPLORER XXIII MICROMETEOROID SATELLITE

DESCRIPTION AND RESULTS FOR THE PERIOD NOVEMBER 6, 1964, THROUGH NOVEMBER 5, 1965

Compiled by Robert L. O' Neal
Langley Research Center

SUMMARY

The Explorer XXIII (1964 74A) was placed in orbit on November 6, 1964, with a perigee of 464 km and an apogee of 980 km. It carried stainless-steel pressurized penetration detectors, impact detectors, and cadmium sulfide cells to provide data on the near-earth meteoroid environment. In addition, the spacecraft was designed to provide data on the effects of the space environment on the operation of capacitor type of penetration detectors and solar-cell power supplies. The spacecraft operated satisfactorily during the 1-year design life, and the objectives of the mission were accomplished.

The puncture rate in 25-micron stainless steel, derived on the basis of 50 punctures, is 4.1×10^{-6} m^{-2}-sec^{-1}. With 95-percent confidence, the average puncture rate in 25-micron stainless steel lies between 3.0×10^{-6} and 5.4×10^{-6} puncture m^{-2}-sec^{-1}.

The puncture rate in 50-micron stainless steel, derived on the basis of 74 punctures, is 2.4×10^{-6} m^{-2}-sec^{-1}. With 95-percent confidence, the average puncture rate in 50-micron stainless steel lies between 1.9×10^{-6} and 3.0×10^{-6} puncture m^{-2}-sec^{-1}.

The puncture rates obtained for stainless steel on Explorer XXIII are close to the puncture rates obtained for beryllium copper on Explorer XVI. The confidence limits include the data points obtained from Explorer XVI.

A total of two counts were recorded by the capacitor-detector experiment during the 1-year reporting period. No conclusions can be reached concerning the effects of the space environment on the detector operation. The capacitor-detector monitoring circuit indicated that both detectors maintained bias voltage during the 1-year period.

The counting rates on the high- and medium-sensitivity meteoroid-impact-detection systems when converted to equivalent puncture rates gave much higher averages than did the pressurized-cell puncture rates. The data from these two systems appear questionable. Although the converted data from the low-sensitivity system are near the level of pressurized-cell data, little confidence can be placed in the relatively poor statistical sampling of impacts.

The solar aspect sensor and the four solar-cell test groups performed satisfactorily during the mission. The N/P, 1 ohm-cm, silicon solar cells covered with 0.476-cm-thick synthetic fused silica shields degraded approximately 4 percent while the unshielded N/P, 1 ohm-cm, silicon solar cells degraded approximately 16 percent during the mission. The solar-cell degradation rate was not constant over this period. Damage plateaus were observed, with more rapid degradation occurring when apogee was in the southern hemisphere.

By use of the measured puncture rates and Pegasus data, a preliminary meteoroid-penetration model was developed. This model is defined for stainless steel as

$$\log \text{Penetration flux} = -5.9657 + 1.3638(\log \text{Thickness}) - 0.6831(\log \text{Thickness})^2$$

for the thickness range from 9.9 microns to 8.4×10^3 microns.

The cadmium-sulfide-cell meteoroid-penetration experiments were found to be inoperative immediately after launch. Telemetry performance was satisfactory throughout the mission. The temperatures of all systems remained within acceptable limits.

I. INTRODUCTION

By Robert L. O'Neal
Langley Research Center

The Explorer XXIII (1964 74A), previously designated the S-55c micrometeoroid satellite, was placed in orbit on November 6, 1964, by the Scout launch vehicle. This was the third in the series of S-55 micrometeoroid satellites placed in orbit. The primary objective of the S-55 project was to make direct measurements of the meteoroid-penetration hazard in near-earth space. Such measurements provide an accurate estimate of the probability of penetration in spacecraft structures by meteoroids. The description of and the results from the initial S-55 satellites, Explorer XIII and Explorer XVI, are presented in references I-1 to I-5.

Because of the gross uncertainty of the meteoroid environment prior to the launch of Explorer XVI, the largest exposed areas of that spacecraft were assigned to the thinnest penetration test material and the smallest exposed areas were assigned to the thicker penetration test materials. This arrangement of exposed area and test material thickness would better assure getting penetration data in at least one material thickness. During the Explorer XVI flight, punctures were obtained in two thicknesses of the beryllium-copper test material. A much better statistical sample was obtained in the thin test material than in the thick. These measured punctures indicated a much smaller decrease in puncture frequency with increasing material thickness than had been expected. It was believed that this measured trend might be affected by the relatively poor statistical sampling of punctures in the thicker material.

Explorer XXIII was designed to obtain, as a primary objective, a more uniform statistical sample of punctures in two thicknesses of test material and thus to allow a more confident definition of the penetration-flux—material-thickness relation. The Explorer XVI data were used to assign exposed areas to the two thicknesses of test material. After the design of Explorer XVI, an effort was made to fabricate and qualify stainless-steel penetration sensors. This effort was successful and stainless steel was selected as the penetration test material for Explorer XXIII.

The secondary objective of the mission was to collect data on the effects of the space environment on the operation of a capacitor-type meteoroid-penetration detector. Other objectives were to obtain data on meteoroid impacts in three momentum ranges, to obtain data on punctures produced in two thicknesses of poly [ethylene terephthalate] film (PET) by micrometeoroids, and to obtain data on the degradation of N/P solar cells in the space environment. It was an experimental objective to collect data from all experiments for a period of 1 year after spacecraft launch.

The Explorer XXIII spacecraft was similar to the Explorer XIII and Explorer XVI spacecraft described in detail in reference I-1. Differences between Explorer XXIII and these earlier Explorer satellites, where significant, are noted in later sections of this report. Figure I-1 is a photograph of Explorer XXIII, and figure I-2 is a sketch showing the spacecraft in the vehicle heat shield. The spacecraft was built around the fourth stage of the launch vehicle, and the burned-out fourth stage remained as part of the orbiting satellite. The spacecraft was cylindrical in shape, about 61 cm in diameter, and about 234 cm long. Spacecraft mass, the vehicle fourth-stage hardware and motor being neglected, was 96.4 kg. The mass of the assembly placed in orbit after fourth-stage burnout was 134.5 kg.

Reference I-6 presents some of the data obtained during the initial weeks of operation of Explorer XXIII. Much of the information in references I-1 to I-5 describing the spacecraft, systems, and operations have been used directly in this report.

The various parts of the Explorer XXIII program are under several different experimenters and specialists who have contributed the subsequent chapters of this report relating to their particular areas. This report presents a summary of the data obtained from Explorer XXIII during the 1-year period following launch – November 6, 1964, through November 5, 1965.

REFERENCES

I-1. D'Aiutolo, Charles T., coordinator: The Micrometeoroid Satellite Explorer XIII (1961 Chi) – Collected Papers on Design and Performance. NASA TN D-2468, 1964.

I-2. Hastings, Earl C., Jr., compiler: The Explorer XVI Micrometeoroid Satellite – Description and Preliminary Results for the Period December 16, 1962, Through January 13, 1963. NASA TM X-810, 1963.

I-3. Hastings, Earl C., Jr., compiler: The Explorer XVI Micrometeoroid Satellite – Supplement I, Preliminary Results for the Period January 14, 1963, Through March 2, 1963. NASA TM X-824, 1963.

I-4. Hastings, Earl C., Jr., compiler: The Explorer XVI Micrometeoroid Satellite – Supplement II, Preliminary Results for the Period March 3, 1963, Through May 26, 1963. NASA TM X-899, 1963.

I-5. Hastings, Earl C., Jr., compiler: The Explorer XVI Micrometeoroid Satellite – Supplement III, Preliminary Results for the Period May 27, 1963, Through July 22, 1963. NASA TM X-949, 1964.

I-6. O'Neal, Robert L., compiler: The Explorer XXIII Micrometeoroid Satellite – Description and Preliminary Results for the Period November 6, 1964 Through February 15, 1965. NASA TM X-1123, 1965.

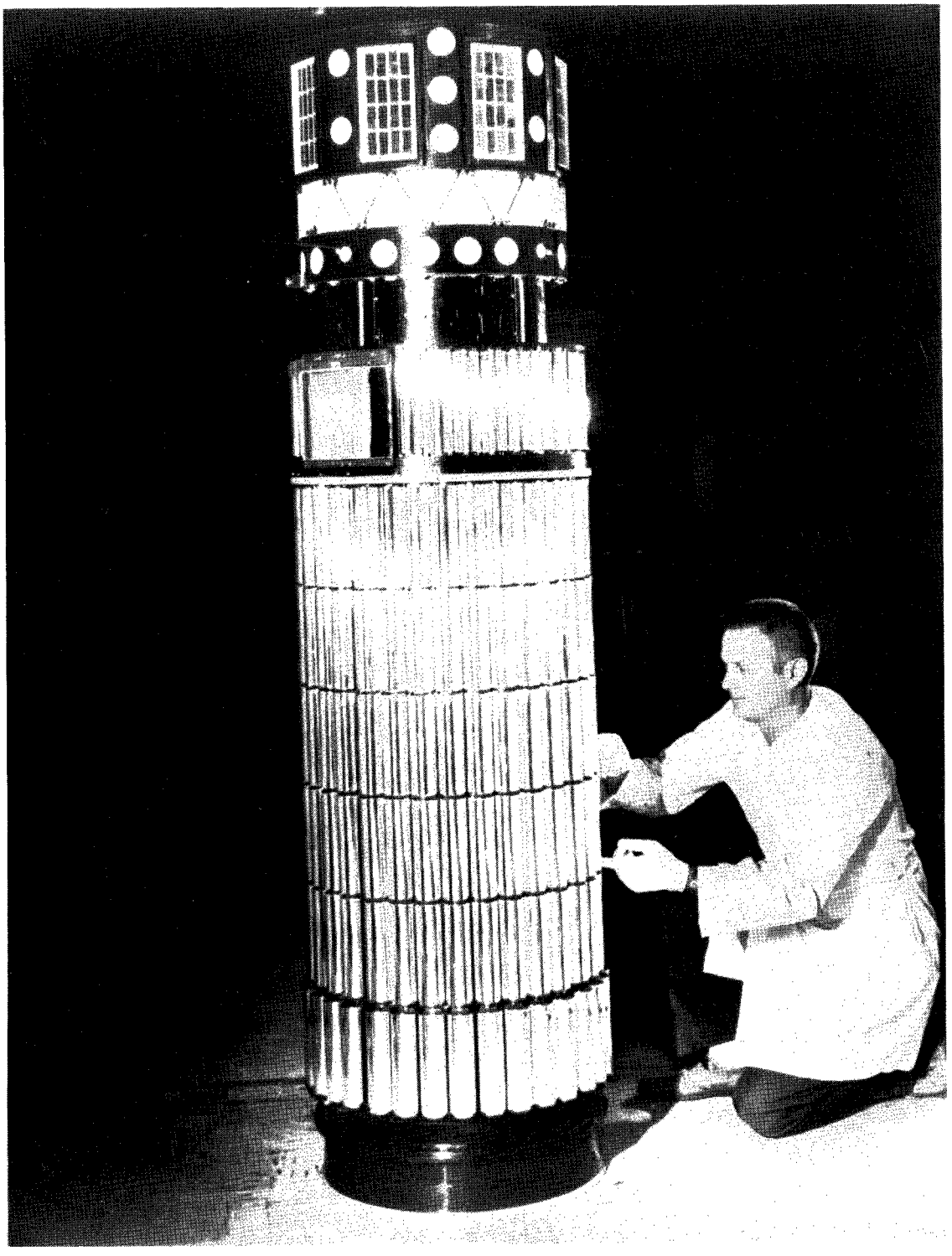

Figure I-1.- Photograph of Explorer XXIII.

L-64-8758

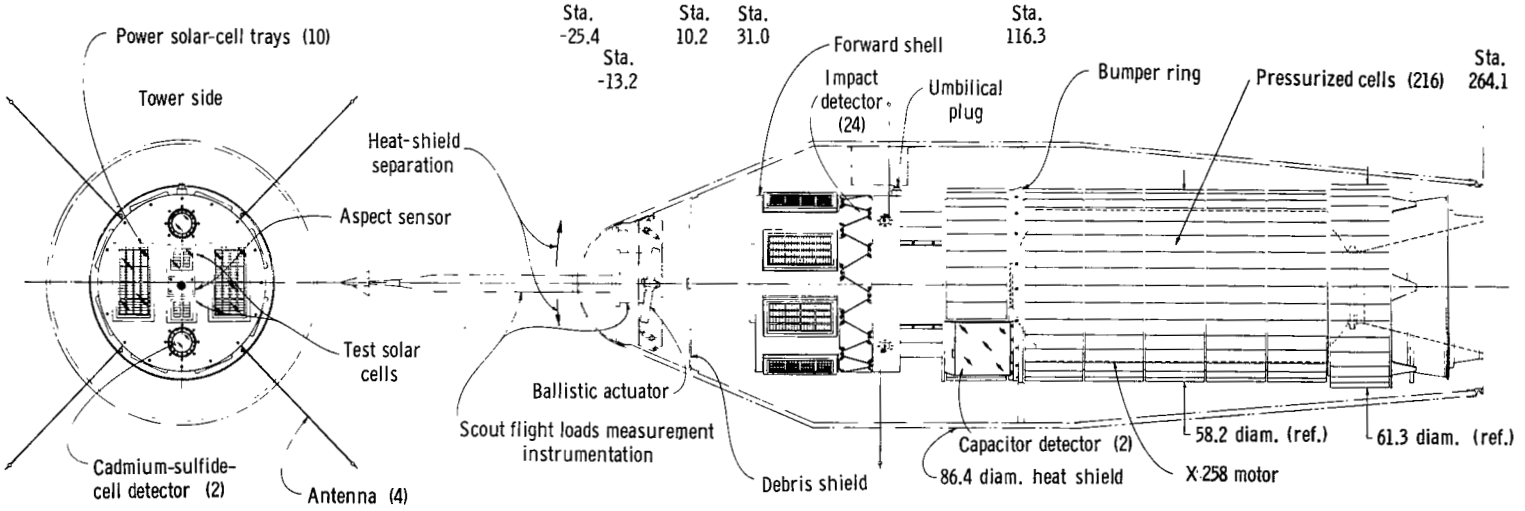

Figure I-2.- Payload assembly drawing. All dimensions are in centimeters.

II. PRESSURIZED-CELL EXPERIMENT

By Charles A. Gurtler and Gary W. Grew
Langley Research Center

DESCRIPTION

The frequency at which two different thicknesses of stainless steel were punctured in space was obtained by the pressurized-cell experiment. The pressurized cells were constructed by utilizing the test material as that part of the pressure-carrying structure of the cell exposed to the space environment. Thus, the frequency at which cells lost pressure was a direct measure of the frequency at which the test material was being punctured by meteoroids.

A drawing of a pressurized cell with the test material noted is shown in figure II-1. The test material was half-hard type 302 stainless steel. Test material thicknesses were 25.4 ± 2.5 microns and 50.8 ± 2.5 microns; these thicknesses are referred to in this paper as 25 and 50 microns, respectively. Of the 210 active cells, 70 had 25-micron-thick test material and 140 had 50-micron-thick test material.

Each cell was pressurized with helium to an absolute pressure of 1300 mm Hg. When the cell is punctured, the gas leaks out and the pressure loss actuates a switch, the opening of which indicates the puncture. Thus, after one puncture, the cell cannot indicate additional punctures; however, the open switch does provide permanent storage of the information that the cell is punctured. A thermal-balance coating was applied to the outer surface of each pressurized cell. It consisted of successive layers of chromium, silicon monoxide, aluminum, and an outer layer of silicon monoxide. The combined thickness of this coating was about 1.4 microns. Dr. George Hass and Alan P. Bradford of U.S. Army Engineer Research and Development Laboratories, Ft. Belvoir, Virginia, directed the coating operation.

A total of 216 pressure cells were mounted in seven rows around the periphery of the spacecraft. Each row contained 32 cells except the forward row which contained 24 cells. The telemeter system could not accommodate 6 of the cells; as a result, these 6 cells were inactive and could not record penetrations. A cross-sectional view of some of the pressure cells mounted around the spacecraft is shown in figure II-2. This placement of the cells was typical of the six most forward rows with the exception of the first row where 4 cells were omitted from each side to provide space for mounting the two capacitor detectors. In each of the six forward rows of cells, there was an 0.20-cm gap between adjacent cells, except for four 1.12-cm gaps equally spaced around the periphery

of the spacecraft. In the aft row of cells, where the spacecraft diameter was increased by 3.1 cm, these gaps were 0.36 cm and 1.32 cm.

The area exposed to the influx of meteoroids in space is considered to be π times the diameter of the circumscribed circle (58.2 cm for the six forward rows and 61.3 cm for the aft row) multiplied by the detector-sensing length. A correction has been made for the open area between the sensors and for the inactive cells. This definition of area gives a total value of 2.07 m^2 for the prelaunch condition. The area associated with each sensor is 9.87×10^{-3} m^2. This area is used in all analyses connected with the pressurized-cell experiment. The areas corresponding to the various thicknesses are given in table II-1:

TABLE II-1.- TOTAL AREA OF CELLS

Material thickness, microns	Number of active cells	Area, m^2
25	70	0.69
50	140	1.38

RESULTS AND DISCUSSION

Seventy-four of the 140 pressurized-cell detectors with 50-micron stainless-steel test material were punctured during the first 365 days of orbital lifetime. This puncture rate corresponds to an average puncture rate of 2.4×10^{-6} punctures m^{-2}-sec^{-1}. During this same period, 50 of the 70 pressurized-cell detectors with 25-micron stainless-steel test material were punctured, the puncture rate corresponding to an average puncture rate of 4.1×10^{-6} punctures m^{-2}-sec^{-1}.

Experimental data for the pressurized cells were taken from 1298 interrogations, the last of which was on the 5311th pass. Of these interrogations, 946 contained data from both telemeters and 352 interrogations contained data from only 1 of the telemeters. The pressurized-cell detectors were divided into two groups which were telemetered separately on the two telemeters. One telemeter transmitted data on seventy 50-micron detectors and forty 25-micron detectors. The other telemeter transmitted data on seventy 50-micron detectors and thirty 25-micron detectors. When only one of the telemetric transmissions from an interrogation was reducible, data were received, in effect, from only approximately one-half of the sensors. Data were not lost in such cases, since they could be recovered in subsequent interrogations; however, there would be less precision in identifying the time of a puncture.

Table II-2 shows the first interrogation in which each new puncture was recorded and the elapsed time since the last previous interrogation. The maximum uncertainty in the time of occurrence of a puncture was 44 hours and 32 minutes. Since the area of only one detector is involved during this time, the time area uncertainty is negligible when compared with the total time area for the experiment.

TABLE II-2.- TIME OF PUNCTURE

Pass	Greenwich date	Greenwich mean time at interrogation	Time since last interrogation, hr	min	Accumulated punctures for detector thickness of –	
					25 microns	50 microns
13	Nov. 7, 1964	9:24	3	19	0	1
46	Nov. 9, 1964	17:02	4	7	0	2
84	Nov. 12, 1964	6:50	5	1	0	3
170	Nov. 18, 1964	4:59	6	45	1	4
235	Nov. 22, 1964	17:16	7	14	1	5
308	Nov. 27, 1964	18:06	1	49	1	6
314	Nov. 28, 1964	2:55	3	20	2	7
344	Nov. 30, 1964	4:37	1	45	3	7
354	Nov. 30, 1964	20:56	3	46	4	7
372	Dec. 2, 1964	2:54	17	16	4	8
386	Dec. 3, 1964	2:01	8	25	5	8
409	Dec. 4, 1964	16:29	13	36	6	8
454	Dec. 7, 1964	18:21	26	35	6	9
466	Dec. 8, 1964	13:59	9	36	7	9
485	Dec. 9, 1964	21:27	21	22	8	9
531	Dec. 13, 1964	01:57	12	3	9	9
544	Dec. 13, 1964	23:12	10	11	9	10
558	Dec. 14, 1964	22:13	9	17	10	11
603	Dec. 18, 1964	01:02	26	45	11	11
618	Dec. 19, 1964	1:57	13	54	11	12
640	Dec. 20, 1964	13:34	16	13	12	12
660	Dec. 21, 1964	23:11	7	17	13	12
673	Dec. 22, 1964	20:19	6	48	13	13
739	Dec. 27, 1964	9:15	21	33	14	13
789	Dec. 30, 1964	20:07	6	56	14	14
799	Dec. 31, 1964	12:19	23	8	14	15

TABLE II-2.- TIME OF PUNCTURE – Continued

Pass	Greenwich date	Greenwich mean time at interrogation	Time since last interrogation, hr	min	Accumulated punctures for detector thickness of –	
					25 microns	50 microns
812	Jan. 1, 1965	9:43	12	21	15	15
857	Jan. 4, 1965	12:23	5	2	15	16
869	Jan. 5, 1965	7:53	19	30	15	17
880	Jan. 6, 1965	3:23	19	30	15	18
967	Jan. 12, 1965	3:19	8	24	15	19
986	Jan. 13, 1965	9:27	8	22	15	20
1039	Jan. 17, 1965	01:01	23	32	15	21
1118	Jan. 22, 1965	12:07	8	47	16	21
1147	Jan. 24, 1965	12:06	10	31	16	22
1155	Jan. 25, 1965	00:51	12	45	17	22
1190	Jan. 27, 1965	11:11	10	40	18	22
1247	Jan. 31, 1965	9:02	4	6	19	22
1346	Feb. 7, 1965	4:42	10	35	20	23
1358	Feb. 8, 1965	00:53	9	28	21	23
1381	Feb. 9, 1965	15:24	19	29	21	24
1412	Feb. 11, 1965	17:33	14	41	21	25
1426	Feb. 12, 1965	16:40	14	47	22	25
1446	Feb. 14, 1965	1:52	3	20	23	25
1455	Feb. 14, 1965	16:37	18	5	24	25
1630	Feb. 26, 1965	18:24	5	48	24	26
1646	Feb. 27, 1965	20:26	26	2	25	26
1671	Mar. 1, 1965	13:30	18	40	25	27
1816	Mar. 11, 1965	13:11	5	58	25	28
1820	Mar. 11, 1965	20:25	7	14	25	29
1839	Mar. 13, 1965	04:16	21	17	25	30
1864	Mar. 14, 1965	21:38	9	15	25	31
1928	Mar. 19, 1965	06:03	13	26	25	32
1945	Mar. 20, 1965	10:31	22	12	25	33
1949	Mar. 20, 1965	17:38	13	52	25	34
2006	Mar. 24, 1965	15:27	6	45	25	35
2031	Mar. 26, 1965	08:39	25	5	26	35

TABLE II-2.- TIME OF PUNCTURE – Continued

Pass	Greenwich date	Greenwich mean time at interrogation	Time since last interrogation, hr	min	Accumulated punctures for detector thickness of – 25 microns	50 microns
2090	Mar. 30, 1965	10:14	10	10	26	36
2102	Mar. 31, 1965	05:56	5	27	27	36
2120	Apr. 1, 1965	12:03	7	15	27	37
2149	Apr. 3, 1965	11:46	22	46	28	38
2199	Apr. 6, 1965	22:08	12	53	28	39
2202	Apr. 7, 1965	03:01	4	53	28	40
2217	Apr. 8, 1965	04:00	18	05	28	41
2236	Apr. 9, 1965	12:21	9	03	28	42
2330	Apr. 15, 1965	22:37	12	08	29	42
2383	Apr. 19, 1965	15:16	21	55	30	42
2507	Apr. 28, 1965	3:25	22	45	30	43
2521	Apr. 29, 1965	02:47	13	8	30	44
2543	Apr. 30, 1965	14:38	24	49	30	45
2675	May 9, 1965	17:22	7	16	31	45
2723	May 13, 1965	01:13	12	48	32	45
2734	May 13, 1965	18:21	6	39	32	46
2737	May 14, 1965	00:19	23	6	33	47
2761	May 15, 1965	15:29	7	16	34	47
2823	May 19, 1965	22:27	35	52	35	48
2847	May 21, 1965	13:08	8	58	36	48
2863	May 22, 1965	15:18	20	56	37	48
2937	May 27, 1965	18:24	6	12	38	48
2965	May 29, 1965	16:13	10	4	38	49
3006	June 1, 1965	11:50	19	17	39	49
3115	June 8, 1965	23:01	14	33	40	49
3122	June 9, 1965	11:51	12	50	40	50
3149	June 11, 1965	08:09	6	37	41	50
3276	June 20, 1965	02:01	6	5	41	51
3316	June 22, 1965	20:04	10	58	41	52
3379	June 27, 1965	04:24	12	22	41	53
3394	June 28, 1965	05:20	8	41	42	53

TABLE II-2.- TIME OF PUNCTURE – Concluded

Pass	Greenwich date	Greenwich mean time at interrogation	Time since last interrogation, hr	min	Accumulated punctures for detector thickness of –	
					25 microns	50 microns
3415	June 29, 1965	16:13	13	36	43	53
3422	June 30, 1965	03:28	11	15	43	54
3514	July 6, 1965	12:18	9	16	43	55
3639	July 15, 1965	02:52	8	45	44	55
3644	July 15, 1965	11:17	8	25	45	55
3709	July 19, 1965	21:54	14	15	45	56
3786	July 25, 1965	05:47	9	5	45	57
3817	July 27, 1965	07:33	21	12	46	57
3822	July 27, 1965	16:23	8	50	46	58
3854	July 29, 1965	22:11	9	14	46	59
3892	Aug. 1, 1965	12:00	44	32	46	60
3924	Aug. 3, 1965	17:00	4	8	46	61
3953	Aug. 5, 1965	17:17	3	49	47	61
4010	Aug. 9, 1965	15:07	3	23	47	62
4078	Aug. 14, 1965	07:20	17	49	47	63
4203	Aug. 22, 1965	21:44	21	33	47	64
4210	Aug. 23, 1965	9:48	5	17	48	64
4249	Aug. 26, 1965	01:35	17	42	48	65
4287	Aug. 28, 1965	17:40	12	34	48	66
4319	Aug. 30, 1965	21:22	16	19	48	67
4391	Sept. 4, 1965	20:22	19	38	48	68
4407	Sept. 5, 1965	22:48	5	54	48	69
4473	Sept. 10, 1965	13:00	10	45	48	70
4505	Sept. 12, 1965	16:34	12	22	48	71
4736	Sept. 28, 1965	14:26	16	13	49	71
4826	Oct. 4, 1965	19:26	6	53	49	72
5060	Oct. 20, 1965	22:56	12	32	49	73
5132	Oct. 25, 1965	21:58	1	48	49	74
5311	Nov. 7, 1965	04:50	28	30	50	74

The average puncture rates of the 25-micron and 50-micron detectors were calculated by dividing the total number of punctures by the total time-area products; that is,

$$\psi = \frac{n}{T} \tag{1}$$

where

ψ punctures m^{-2}-sec^{-1}

n total number of punctures

T total exposed time-area product, m^2-sec

The exposed time-area calculations considered the loss in area as a result of punctured detectors. Each time one of the sensors was punctured, the exposed area of the experiment was reduced. The reduced area was then used until the next punctured detector occurred. The total exposed time-area products and the puncture rates for the two material thicknesses are shown in table II-3.

TABLE II-3.- TIME-AREA PRODUCTS AND PUNCTURE RATES

Material thickness, microns	Number of punctures	Time-area products for 365 days, m^2-sec	Average puncture rate, punctures m^{-2}-sec^{-1}
25	50	1.209×10^7	4.1×10^{-6}
50	74	3.058	2.4

The total time-area product for the 25-micron sensors was 1.209×10^7 m^2-sec with an average puncture rate of 4.1×10^{-6} punctures m^{-2}-sec^{-1}. This average rate is only slightly higher than the puncture rate of 3.9×10^{-6} punctures m^{-2}-sec^{-1} which was obtained in the 25-micron beryllium-copper material on the Explorer XVI. (See ref. II-1.) The total time-area product for the 50-micron sensors was 3.058×10^7 m^2-sec with an average puncture rate of 2.4×10^{-6} punctures m^{-2}-sec^{-1}. This average rate is also only slightly higher than the puncture rate of 2.0×10^{-6} punctures m^{-2}-sec^{-1} which was obtained in the 50-micron beryllium-copper material on the Explorer XVI.

Figures II-3 and II-4 show the history of the 50 punctures in the 25-micron sensors and the 74 punctures in the 50-micron sensors that occurred during the 365 days of the mission. Curves showing punctures as a function of time based on the average puncture

rates have been plotted. Equation (1) was used to calculate the time between punctures by using the average puncture rates. The dashed curves have been plotted to show one-standard-deviation $\left(\sqrt{\text{Number of punctures}}\right)$ boundaries for the average curves. Most data points fall within one standard deviation. However, there is some indication that over short periods of time, the puncture rates vary by a factor of two or three. Figure II-5 shows a plot of punctures in the 25-micron test material as a function of time-area product. Lines have been drawn through groups of data points that appear to define a reasonably straight line. The slopes of these lines are somewhat steeper than the average slope obtained for the 1-year period. Some bunching of the penetrations with respect to time would be expected in a random process; however, it would appear that there is a cyclic trend to the bunching in this plot. Similar results can be observed in the Explorer XVI and Pegasus data. (See refs. II-1 and II-2.) The cyclic trend is not evident in the 50-micron puncture history. The data obtained from both the 25-micron and 50-micron material thicknesses were tested from randomness by applying the chi-square tests as described in reference II-3.

If the data are random, the experimental time-area products between punctures should be distributed according to the probability density function

$$f(T) = \psi e^{-\psi T} \tag{2}$$

where the symbols are as indicated previously. To test the data the values of χ^2 are determined; that is

$$\chi^2 = \sum_{i=1}^{n} \frac{\left[(\text{Observed value})_i - (\text{Expected value})_i\right]^2}{(\text{Expected value})_i} \tag{3}$$

For the 50-micron detectors, the data were divided into eleven classifications of equal time-area intervals, 13×10^4 m^2-sec, except for the eleventh classification, which included all time-area products between punctures greater than 13×10^5 m^2-sec. The "expected values" for each classification were found by the equations

$$(\text{Expected value})_i = n \int_{T_{i-1}}^{T_i} f(T)\, dT \qquad (i = 1, 2, \ldots, 10) \tag{4}$$

and

$$(\text{Expected value})_i = n \int_{T_{i-1}}^{T_\infty} f(T)\, dT \qquad (i = 11) \tag{5}$$

where n is the total number of punctures and i denotes the particular classification.

Figure II-6 compares the experimental values with the theoretical values of number of punctures having time-area products between punctures that fall within the time-area classification shown. For example, experimentally, 13 punctures in which the time-area products between punctures were found to lie within 26 to 39 $\times 10^4$ m^2-sec as compared with the theoretical prediction of 10.8 punctures were found. Theory and experiment appear to be in fair agreement. The value of χ^2 for this case was found to be 5.05. According to the chi-square test, if χ^2 lies between 4.17 and 14.7, there is some justification for the conclusion that the puncture data are random. Figure II-7 shows the results of performing the same test on the 25-micron data. For this case to be random, χ^2 should lie between 1.06 and 7.78; the actual value was 4.24.

Figure II-8 shows the puncture rates obtained from Explorer XXIII and Explorer XVI presented as a function of thickness for stainless-steel sheet. Pegasus puncture rates in aluminum (ref. II-4), tentatively interpreted in terms of stainless steel, are shown for comparison. Three curves of predicted puncture rate as a function of thickness for stainless-steel sheet are also shown. The three curves labeled "optimistic," "best estimate," and "pessimistic" have been obtained by using the approach taken by Whipple. (See ref. II-5.) In this reference, Whipple derived a "best estimate" formula for the near-earth flux of meteoroids that can penetrate an aluminum sheet as a function of thickness:

$$\log N = -4.02 \log P - 13.33 \tag{6}$$

where N is the meteoroid flux rate in meteoroids m^{-2}-sec^{-1} and P is the thickness in cm of type 2024 aluminum sheet.

For making the comparison with the experimentally obtained data, two changes were made to Whipple's formula. The formula was adjusted for earth shielding and was also modified to give the penetration rate in half-hard 302 stainless steel instead of in aluminum.

Whipple assumed that because of earth shielding, the meteoroid flux at a point near the earth would be one-half that existing in free space. Equation (6) corresponds to such a reduced flux. For the mean altitude of Explorer XVI and Explorer XXIII, the earth is estimated to shield only about one-fourth of the 4π steradian influx of meteoroids. Therefore, at such an altitude, the flux is 3/2 as much as that indicated by equation (6). The flux rate in Whipple's formula (6) has accordingly been multiplied by 3/2 to provide a direct comparison with experimental data.

In the derivation of his formula, Whipple utilized, from Herrmann and Jones (ref. II-6), the following equation for the penetration of a semi-infinite target by spherical particles:

$$\frac{p}{m^{1/3}} = 0.6\left(\frac{6\rho}{\pi\rho_t^2}\right)^{1/3} \log_e\left(1 + \frac{K_0^{2/3}B}{4}\right) \tag{7}$$

where

m projectile mass

p depth of penetration

ρ projectile density

ρ_t target density

$K_0 = \frac{\rho}{\rho_t}$

$B = \frac{\rho_t v^2}{H}$

H Brinell hardness

v velocity of projectile

In addition, Whipple adopted the relation

$$\frac{P}{p} = 1.5 \tag{8}$$

for the conversion from semi-infinite targets to thin sheets (where P is the thickness of the sheet and p is the depth of penetration). For meteoroids, he adopted the values of $\rho = 0.44$ gram-cm^{-3} and $v = 22$ km-sec^{-1}. For the type 302 stainless-steel test material used on Explorer XXIII, the density $\rho_t = 7.86$ grams-cm^{-3} and the Brinell hardness $H = 2.85 \times 10^{10}$ dynes-cm^{-2} have been used. Thus, the equation for the rate of penetration of type 302 stainless-steel material by meteoroids at an altitude where the earth shields one-fourth of the total flux is given by

$$\log N = -4.02 \log P - 14.61 \tag{9}$$

By the same procedure Whipple's "pessimistic" and "optimistic" formulas, respectively, become

$$\log N = -4.02 \log P - 13.40 \quad (10)$$

$$\log N = -3 \log P - 13.85 \quad (11)$$

Equations (9), (10), and (11) are represented in figure II-8.

Experimental results obtained in the hypervelocity impact laboratory at the Langley Research Center indicate that the penetration depths in beryllium-copper targets and in steel targets are about the same when obtained under similar impact conditions. (See refs. II-7 and II-8.) This equivalence is also confirmed by using equation (7) of reference II-6 to compute the penetration in beryllium-copper material with a density of 8.26 grams-cm^{-3} and a Brinell hardness H of 1.0×10^{10} dynes-cm^{-2}. The Explorer XVI data for the 25-micron and the 50-micron beryllium-copper materials have also been plotted in figure II-8. Pegasus data in aluminum were interpreted in terms of stainless-steel sheet by using equation (7) which is taken from reference II-6.

Confidence limits (confidence coefficient, 0.95) for the Explorer XXIII data points have been indicated in figure II-8. It can be assumed at least for long periods of time that the puncture data are random and confidence limits can be applied, based on the facts that (a) Explorers XVI and XXIII data resulted in the same puncture rates, (b) chi-square tests were successfully performed on the 25-micron and 50-micron detector puncture data, and (c) most points plotted in figures II-3 and II-4 lie within plus or minus one standard deviation of the average curve through these data points. These limits were computed by using the chi-square distribution in the manner described in reference II-1. The limits on the Explorer XXIII data indicate that one can expect with 95-percent confidence that the puncture rate in punctures m^{-2}-sec^{-1} will be between 3.0×10^{-6} and 5.4×10^{-6} for 25-micron stainless steel and between 1.9×10^{-6} and 3.0×10^{-6} for 50-micron stainless steel.

In figure II-8 the puncture rates obtained from stainless steel on Explorer XXIII are close to the puncture rates obtained from beryllium-copper material on Explorer XVI. The confidence limits include the data points obtained from Explorer XVI. These data fall between the "best estimate" and "optimistic estimate" curves in figure II-8. Explorer XXIII and the Explorer XVI data indicate a more gradual decrease of puncture rate with increasing skin thickness than is shown by the estimated curves.

The comparison in figure II-8 of Explorer and Pegasus measurements of puncture frequency show Explorer measurements to be somewhat higher than Pegasus measurements. Although some uncertainty exists in converting Pegasus data in aluminum to equivalent data in stainless steel, such uncertainties would not explain the difference between the two sets of data. This difference is believed to be due to the different principle of operation of the Explorer pressurized-cell type of detector and the Pegasus

capacitor type of detector. The pressurized cell would be expected to be more sensitive since a complete penetration would not be required to produce a sensor material fracture and leak whereas a complete penetration of the capacitor type of sensor is required to produce the ionization necessary for a sensor discharge. The result would be for the capacitor to react as a thicker pressure cell of the same test material would. The presence of the dielectric and capacitor plate glued to the rear of the test material and also the foam backing on the Pegasus detectors (ref. II-2) would contribute to this characteristic. The contribution of this effect, however, would probably decrease with increasing test material thickness. A complex and extensive ground test program is required to provide a calibration between the two types of detectors. The George C. Marshall Space Flight Center has undertaken a calibration program, but a final calibration is not yet available. Limitations in the ability to obtain meteoroid velocities and masses makes the testing and analysis in such a program difficult and time consuming.

CONCLUSIONS

The primary objective of the Explorer XXIII spacecraft, the measurement of the puncture rate in two thicknesses of stainless steel, was successfully accomplished. The pressurized-cell-experiment data indicate:

1. The puncture rate in 25-micron stainless steel, derived on the basis of 50 punctures is 4.1×10^{-6} m^{-2}-sec^{-1}. With 95-percent confidence, the average puncture rate in 25-micron stainless steel lies between 3.0×10^{-6} and 5.4×10^{-6} punctures m^{-2}-sec^{-1}.

2. The puncture rate in 50-micron stainless steel, derived on the basis of 74 punctures, is 2.4×10^{-6} m^{-2}-sec^{-1}. With 95-percent confidence, the average puncture rate in 50-micron stainless steel lies between 1.9×10^{-6} and 3.0×10^{-6} punctures m^{-2}-sec^{-1}.

3. The puncture rates obtained for stainless steel on Explorer XXIII are close to the puncture rates obtained for beryllium-copper material on Explorer XVI. The confidence limits include the data points obtained from Explorer XVI.

REFERENCES

II-1. Hastings, Earl C., Jr., compiler: The Explorer XVI Micrometeoroid Satellite – Supplement III, Preliminary Results for the Period May 27, 1963, Through July 22, 1963. NASA TM X-949, 1964.

II-2. Anon.: The Meteoroid Satellite Project Pegasus First Summary Report. NASA TN D-3505, 1966.

II-3. Evans, Robley D.: The Atomic Nucleus. McGraw-Hill Book Co., Inc., c.1955.

II-4. Naumann, Robert J.: The Near-Earth Meteoroid Environment. NASA TN D-3717, 1966.

II-5. Whipple, Fred L.: On Meteoroids and Penetration. J. Geophys. Res., vol. 68, no. 17, Sept. 1963, pp. 4929-4939.

II-6. Herrmann, Walter; and Jones, Arfon H.: Correlation of Hypervelocity Impact Data. Proceedings of the Fifth Symposium on Hypervelocity Impact, vol. 1, pt. 2, Apr. 1962, pp. 389-438. (Sponsored by U.S. Army, U.S. Air Force, and U.S. Navy.)

II-7. Collins, Rufus D., Jr.; and Kinard, William H.: The Dependency of Penetration on the Momentum Per Unit Area of the Impacting Projectile and the Resistance of Materials to Penetration. NASA TN D-238, 1960.

II-8. Hastings, Earl C., Jr., compiler: The Explorer XVI Micrometeoroid Satellite – Description and Preliminary Results for the Period December 16, 1962, Through January 13, 1963. NASA TM X-810, 1963.

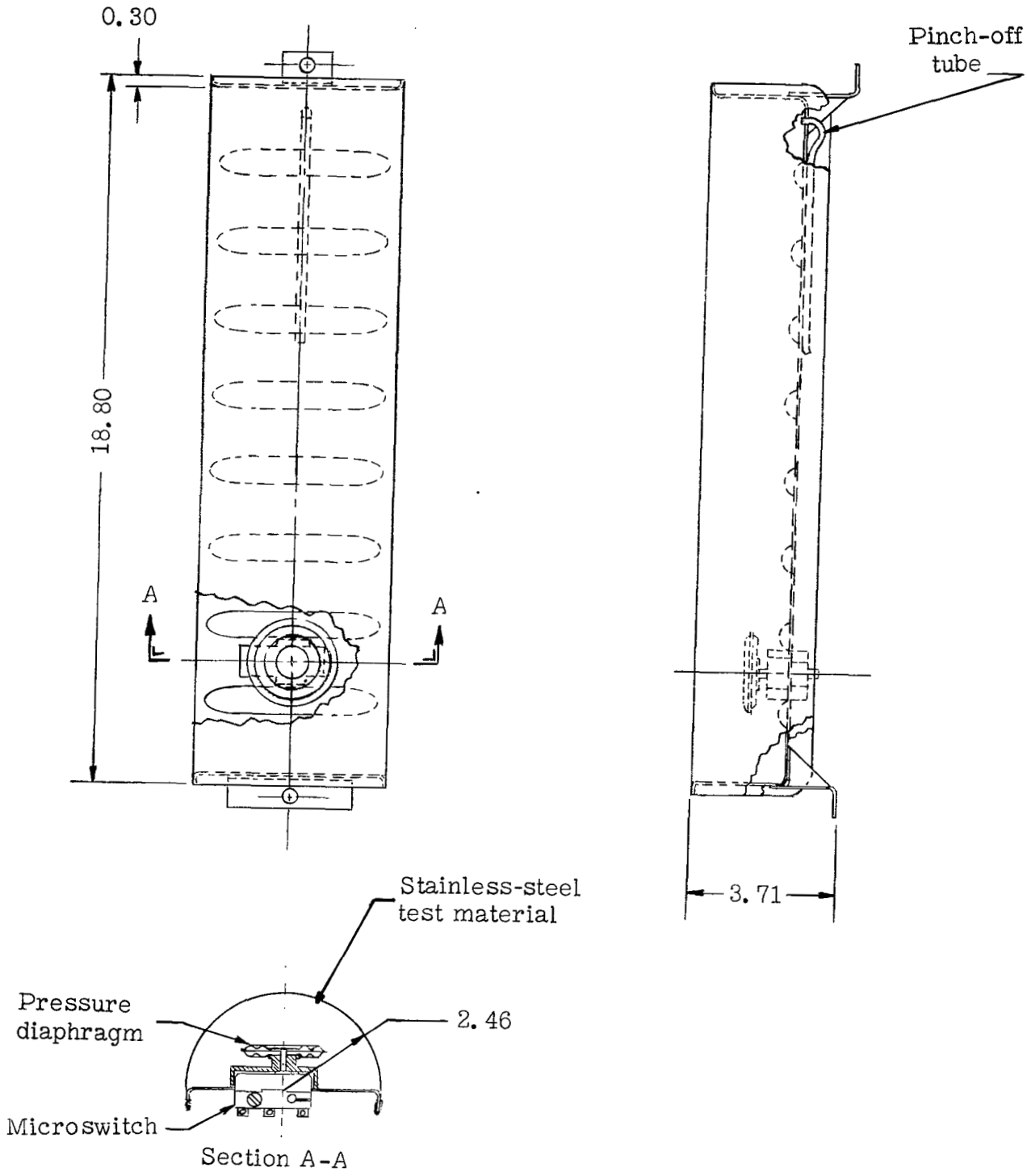

Figure II-1.- Pressurized-cell detector. All dimensions are in centimeters.

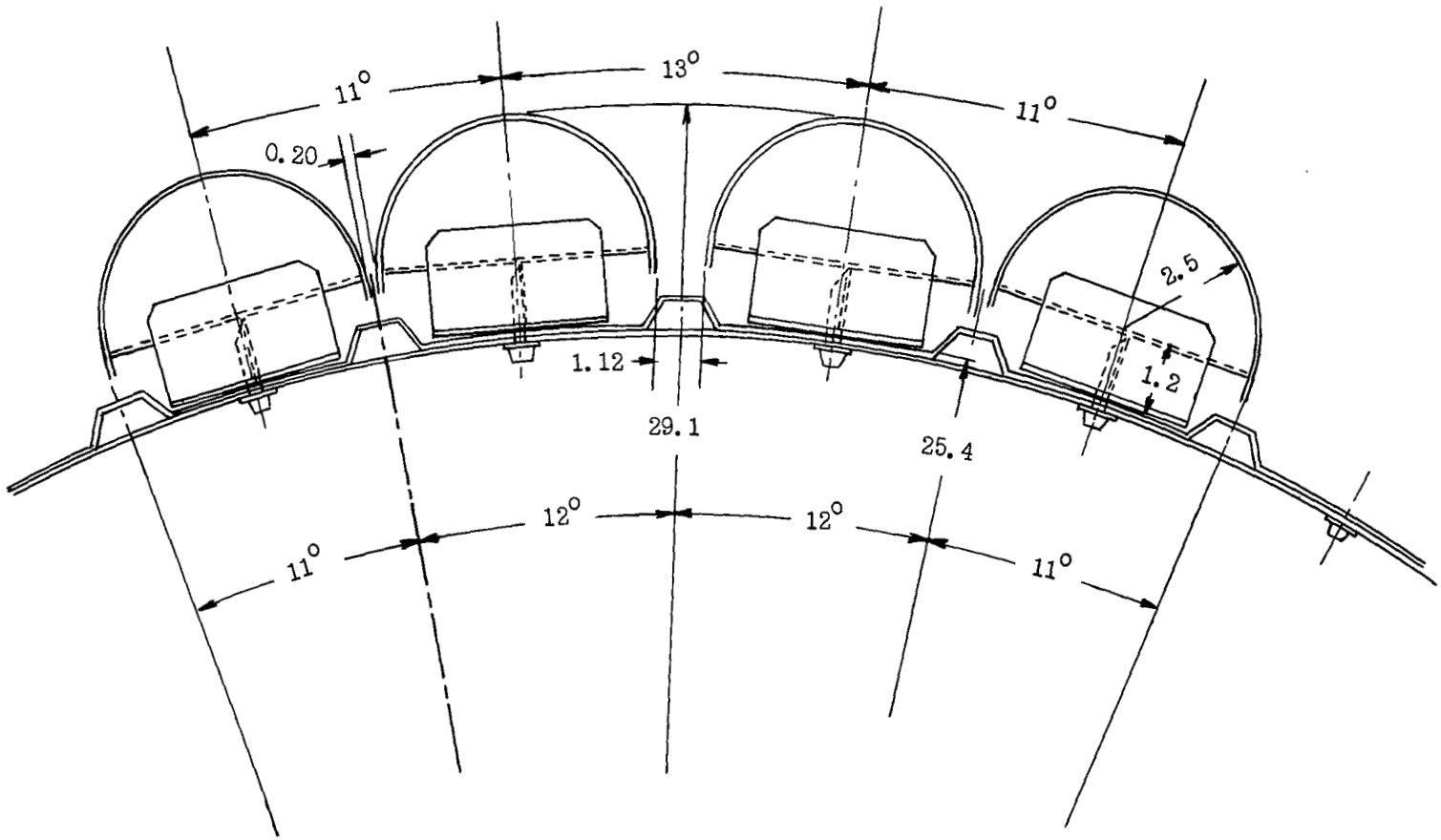

Figure II-2.- Mounting arrangement of pressurized cells. All dimensions are in centimeters unless otherwise noted.

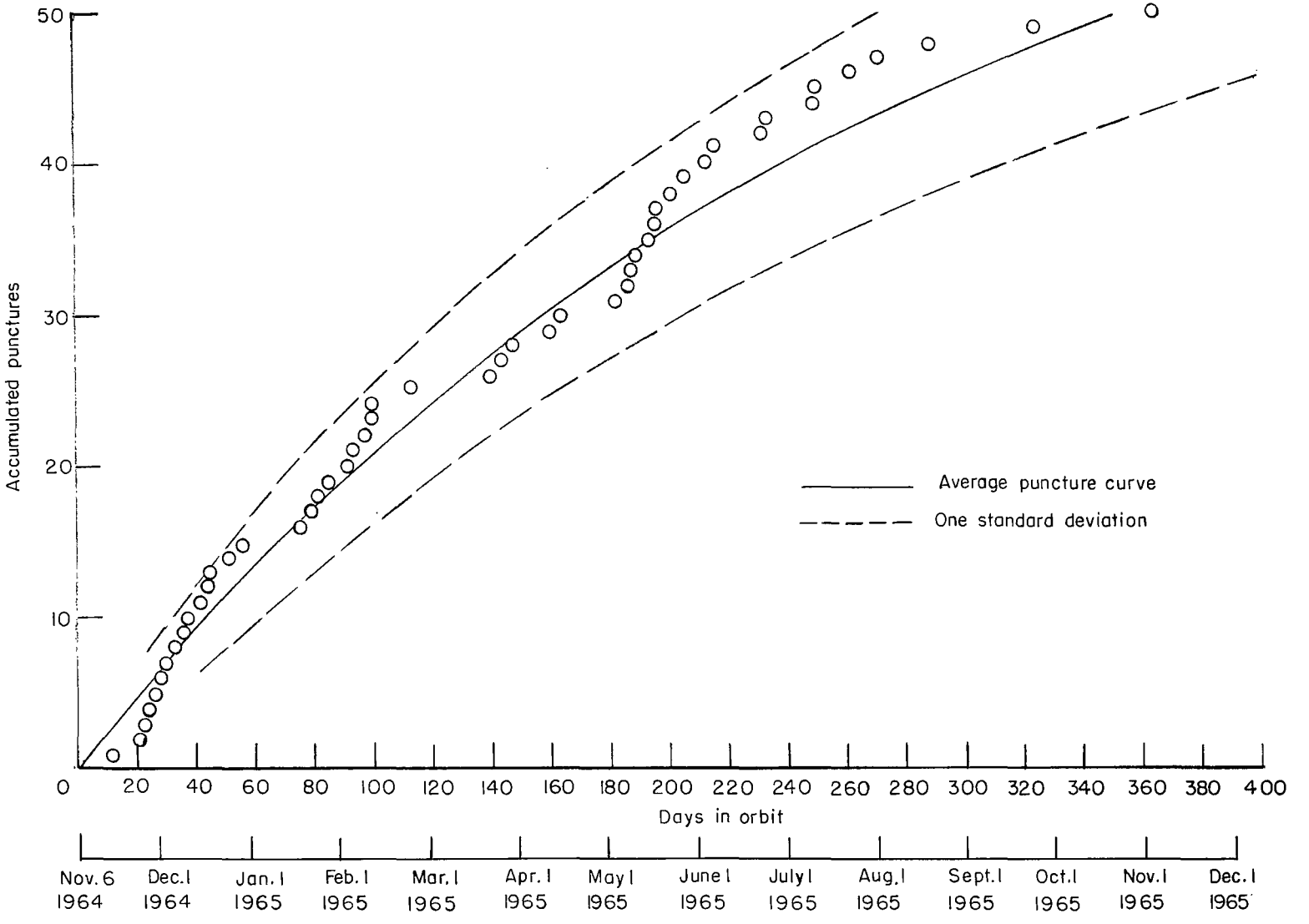

Figure 11-3.- Comparison of puncture history with average puncture curve for 25-micron stainless steel with one-standard-deviation boundaries noted.

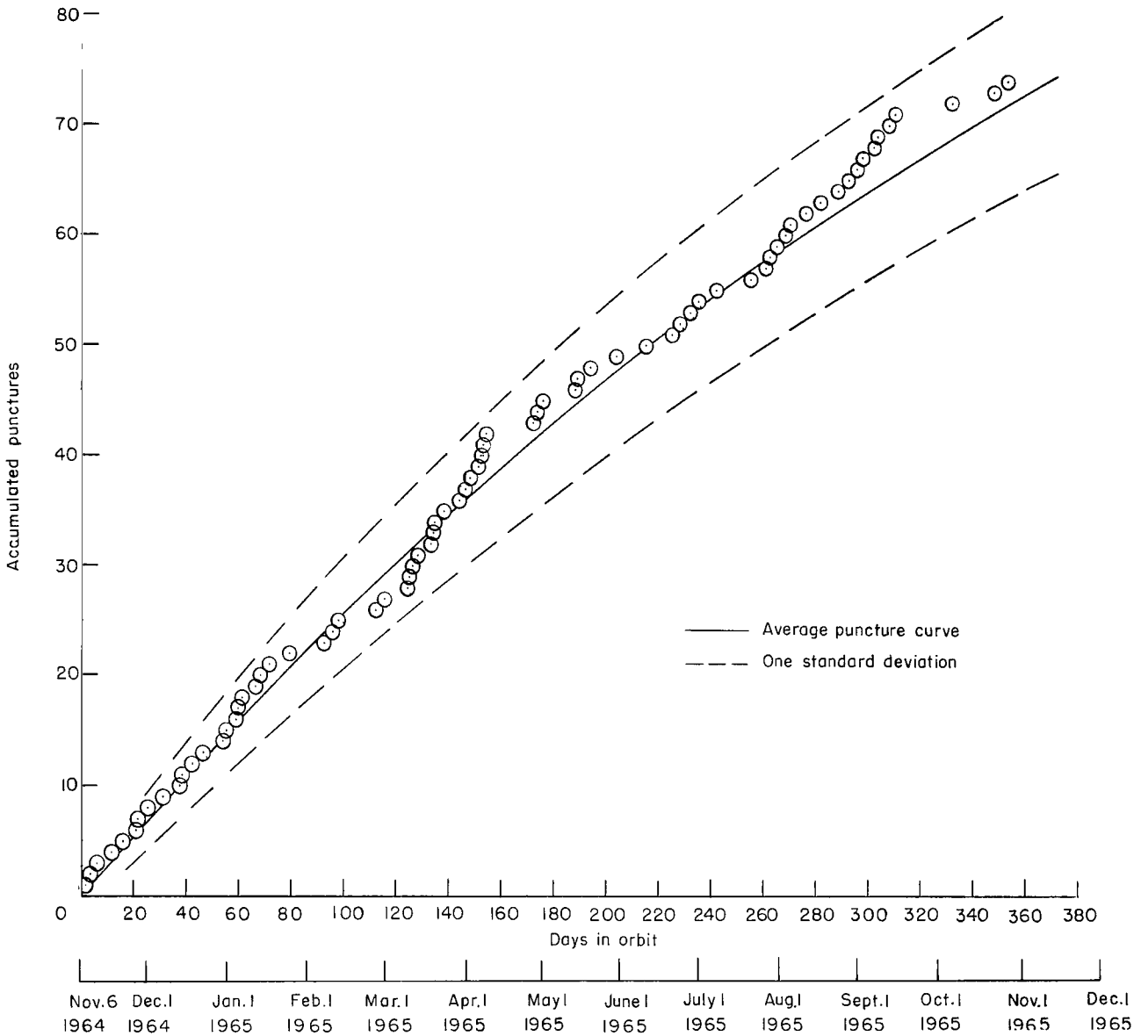

Figure II-4.- Comparison of puncture history with average puncture curve for 50-micron stainless steel with one-standard-deviation boundaries noted.

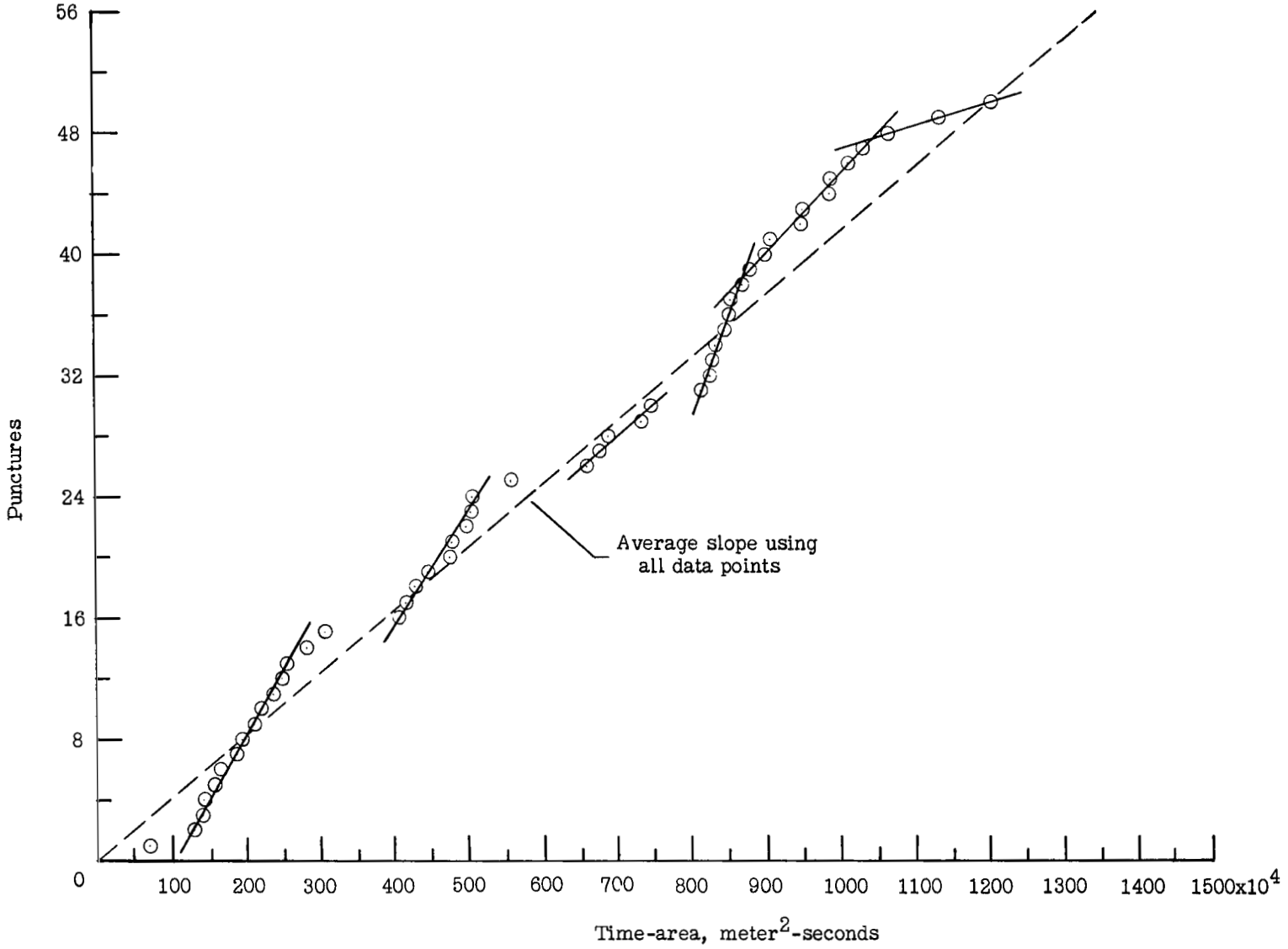

Figure II-5.- History of punctures for 25-micron stainless steel as a function of time-area in which slopes are drawn through groups of data points indicating possible changes in meteoroid flux rates.

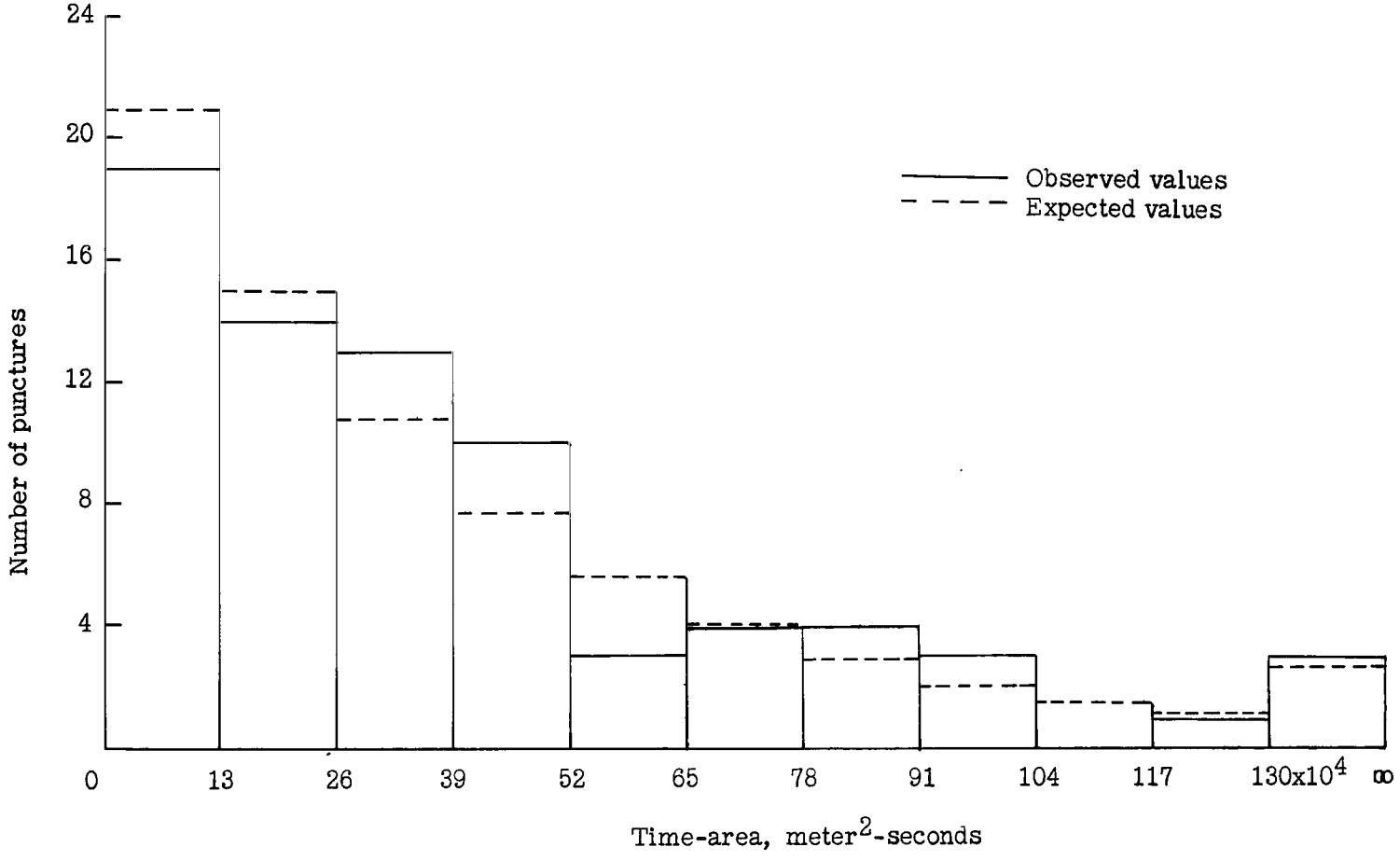

Figure II-6.- Comparison of observed values and expected values of number of punctures for 50-micron stainless steel whose time-area products between punctures fall within the time-area classifications shown.

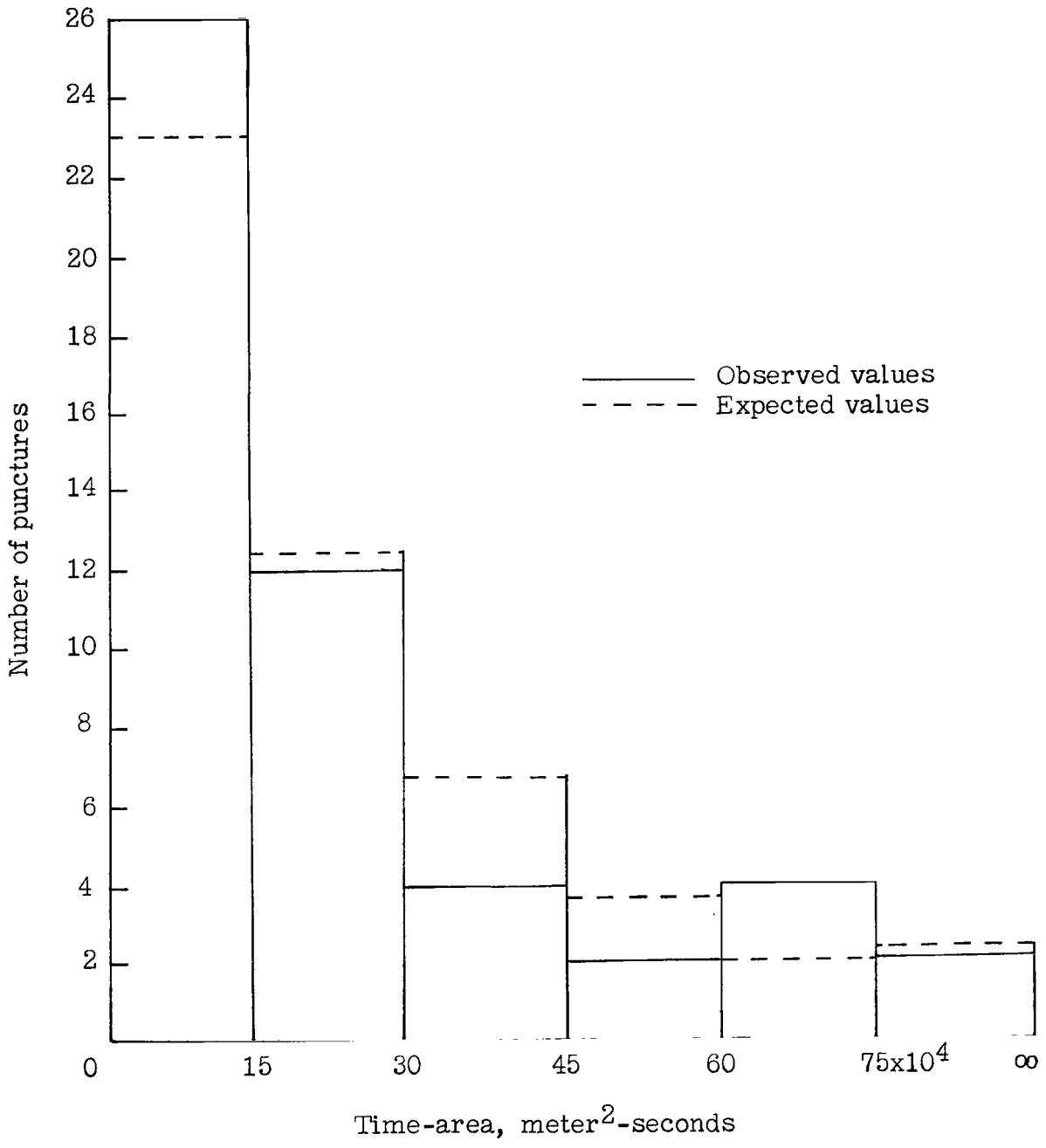

Figure II-7.- Comparison of observed values and expected values of number of punctures for 25-micron stainless steel whose time-area products between punctures fall within the time-area classifications shown.

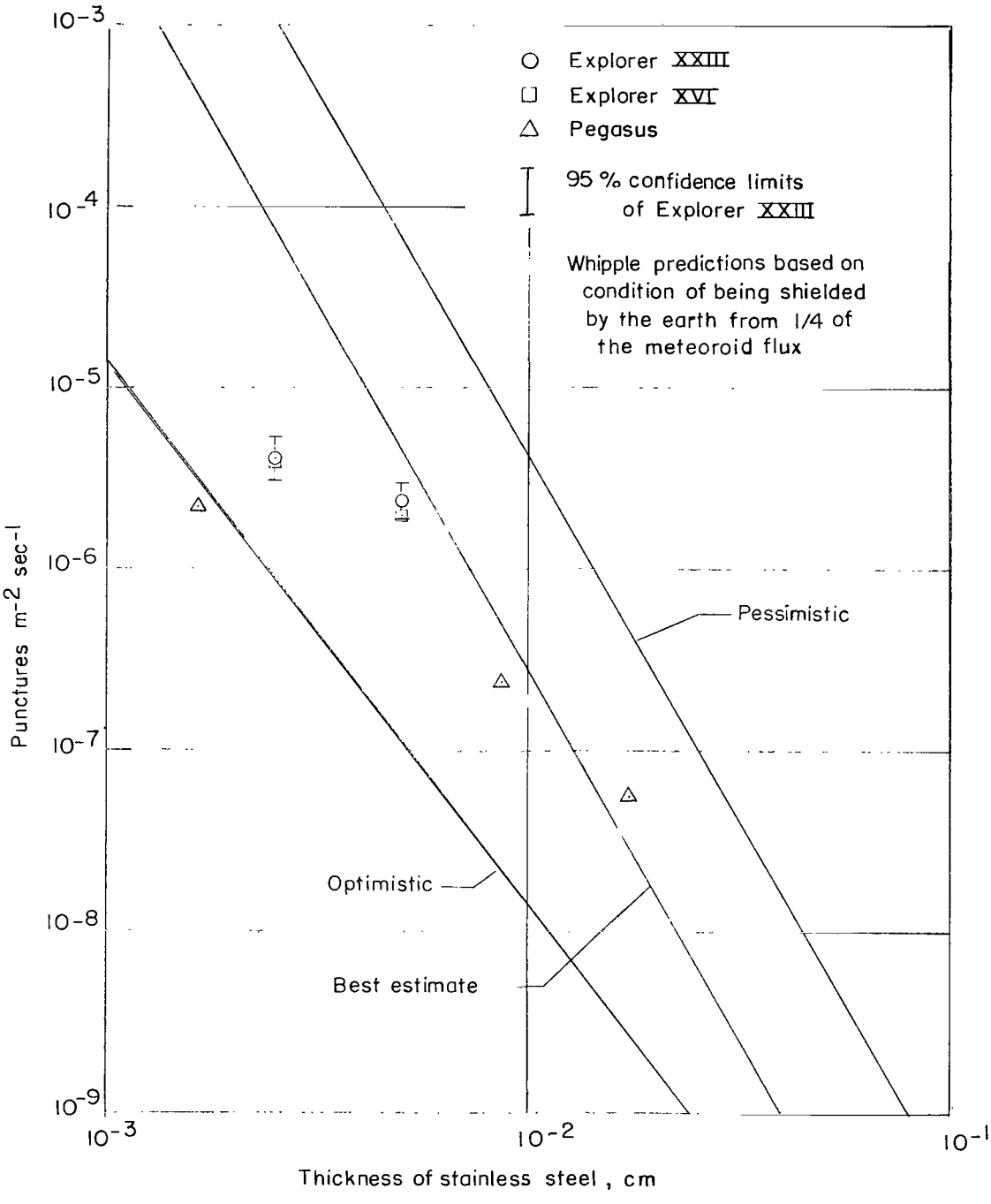

Figure II-8.- Comparison of Explorer XVI and Explorer XXIII pressurized-cell puncture rate as a function of stainless-steel-sheet thickness with three curves of predicted puncture rate and the Pegasus capacitor-detector data. Data points shown represent data from stainless steel on Explorer XXIII, beryllium copper on Explorer XVI, and aluminum on Pegasus; all data points are converted to stainless steel.

III. CAPACITOR-DETECTOR EXPERIMENT

By James H. Siviter, Jr.
Langley Research Center

DESCRIPTION

The capacitor type of meteoroid-penetration detector flown on the Explorer XXIII is essentially a capacitor made up of a thin-film polymer dielectric with a stainless-steel-foil target plate serving as one electrode and a vacuum-deposited copper film serving as the opposite electrode. When a hypervelocity particle penetrates the charged capacitor, a significant amount of material is vaporized in the area of the penetration and produces a conduction path. As a result, the capacitor is momentarily shorted and discharges. The momentary change of the voltage across the sensor during this discharge is detected and stored. The conduction path dissipates in less than 1 μsec and allows the capacitor to recharge. The detector should thus be capable of sensing any number of punctures unlike the pressurized cells which can sense only the first puncture.

The purpose of the capacitor-detector experiment on the Explorer XXIII was to determine whether the space radiation environment had any adverse effects on the operation of the capacitor as a meteoroid-penetration detector. The possibility of such effects occurred when radiation tests, conducted in an electron-radiation facility, indicated frequent sporadic pulsing of the detector, apparently because of electron storage in the dielectric with subsequent discharge to one of the detector electrodes. These tests indicated that possibly hundreds of pulses might occur in flight, with the wave form from some of the pulses similar to that resulting from a particle penetration discharge. These observations indicated the desirability of flying the capacitor detector to determine whether the energetic electrons in space might similarly collect in the dielectric and produce spurious counts when they discharged. The exposed area of the detectors was kept small (726 cm^2) to reduce the probability of meteoroid penetrations and thus better define the origin of any large number of discharges as being induced by radiation. From Explorer XVI penetration data, fewer than 10 meteoroid penetrations of the sensor were expected during 1 year.

From later carefully controlled radiation tests of a flight-configuration sensor in which the total electron dose in each test was of the order of that expected in flight, it was found that although some pulsing did occur, the number of pulses was much less than that observed in earlier tests. The maximum number of pulses observed in any test was six and the minimum number observed was zero. One of the two sensors flown on the

spacecraft was irradiated under the same conditions and displayed similar pulsing characteristics. It was determined that methods used in mounting the sensors and the associated electrical leads in the radiation-facility test chamber and malfunctions in the sensor signal conditioning equipment caused the number of pulses observed in the initial tests to be abnormally high.

The results of the more refined ground tests indicated that the number of radiation-induced pulses in flight would be about the same as or less than the number resulting from penetrations, and thus, it was difficult if not impossible to distinguish between the two. This difficulty made the value of the experiment, in fulfilling the original objective, questionable. It was, however, of interest to establish whether the detector would remain operational for the length of the mission even though the source of any signals produced might not be identifiable.

The capacitor-type penetration detector is shown in figures III-1 and III-2. A photograph of the detector as flown on the spacecraft is shown in figure III-3.

The penetration material consisted of 25.4-micron type 302 stainless steel in the half-hard condition. This same material was used in the 25.4-micron pressure cells. The stainless-steel penetration material also served as one electrode of the capacitor. The dielectric materials consisted of a bilaminate of two sheets of 3.8-micron poly[ethylene terephthalate] film (PET) laminated to each other and to the stainless steel with 0.76-micron adhesive. The total thickness of the bilaminate dielectric was approximately 7.1 microns instead of the design goal of 9.1 microns because of stretching of the PET film during lamination. Approximately 0.65 micron of copper was vacuum deposited to the outer layer of the dielectric to serve as the second electrode.

The bilaminate dielectric system was found to be more satisfactory than a single layer of 6.5 microns of PET film because pinholes in a single sheet may fill with copper and cause an electrical short when the copper electrode is deposited, whereas the probability that such imperfections would be superimposed in a bilaminate is negligible. The use of two layers of 3.8-micron film greatly reduced the number of electrical shorts occurring during fabrication.

A silicon monoxide thermal-balance coating was applied to the outer surface of the stainless-steel foil. The coating was the same as that used on the pressurized cells.

An electrical connection to the vacuum-deposited copper surface was made by soldering a 25-micron copper ribbon directly to the surface. The soldering was accomplished by using a 63-37 solder, a standard flux, and a controlled-temperature (205° C) soldering iron.

The capacitor was mounted on a 0.63-cm-thick layer of polyurethane foam support by a 2.5-micron adhesive. The foam acted as both a low-density support structure and

an absorber for the spray resulting from a meteoroid penetration. A laminated fiber-glass tray was used as the mounting fixture. A printed circuit was laminated to the rear surface of the fiber-glass tray to bring the capacitor leads to terminal pins.

A thermistor temperature-sensing element was located on the rear face of a 1.9-cm by 0.63-cm sample cross section of the detector. Figure III-1 shows the location of the thermistor on the detector panel.

The copper electrodes of the two detectors on the Explorer XXIII spacecraft were charged to a nominal potential of -13 V dc through the signal conditioning circuits. This voltage could vary slightly because it was dependent on the power-supply battery voltage. The stainless-steel electrodes were at ground potential. Each of the two capacitor-detector units was wired into a separate signal conditioner unit and to a separate telemeter. The electrical discharge of the capacitor would be accepted by the signal conditioner unit and stored in a counter to be telemetered to a ground station upon interrogation.

The signal conditioner circuit was designed to bias the capacitor detector with a -13 V dc potential and produce a uniform output signal to the counter when triggered by a fast-rise-time discharge of the capacitor. A block diagram of the capacitor-detector circuitry is shown in figure III-4. Each signal conditioner unit was calibrated to determine its triggering characteristics as shown in figure III-5. The calibration curves show the combinations of pulse amplitude and discharge time that were required to trigger the signal conditioning unit. Any combination of pulse amplitude and discharge time falling above the curve would trigger the unit, whereas any combination of pulse amplitude and discharge time falling below the curve would not trigger the unit. These curves were obtained by capacitive coupling of the square wave pulses of various combinations of amplitude and discharge time into the signal conditioning unit and recording the output. A calibration was performed at 20° C and at 0° C.

Each capacitor detector was supplied with a monitoring circuit as shown in figure III-4 to determine the condition of the detector at each interrogation of the satellite. The monitor unit consisted of a voltage divider circuit wired to the biased side of the detector. This voltage was fed to a subcarrier oscillator in the telemeter. If the detector became electrically "open" or "shorted," the monitor unit voltage would drop to zero.

Additional details concerning the development of the capacitor detector flown on the Explorer XXIII are given in the appendix.

RESULTS AND DISCUSSION

Two discharges were recorded for one of the capacitor detectors during the 365 days from launch through November 5, 1965. No discharges were recorded for the other

detector during this period. The capacitor-detector monitoring circuits indicated that both detectors maintained bias voltage throughout the mission.

It is estimated that Explorer XXIII was exposed to an omnidirectional flux of 10^{10} to 10^{11} electrons/cm^2-day in the energy range 0.5 MeV to 8.0 MeV. This rate would indicate that the electron dose in this energy range for the 365-day period would be of the order of 10^{12} to 10^{13} electrons/cm^2. Little information is available concerning the flux rate in space for the energy spectrum from about 50 keV to 0.5 MeV. This range is generally considered to represent 95 percent of the total flux rate from 50 keV to 8.0 MeV. The corresponding omnidirectional electron dose rate for energies from about 50 keV to 8.0 MeV would then be about 10^{11} to 10^{12} electrons/cm^2-day, and the total dose would be about 10^{13} to 10^{14} electrons/cm^2 for the 365 days in orbit.

For comparison of Explorer XXIII flight results with the results of ground tests, these doses are reduced by about an order of magnitude in order to take into account the facts that (1) the sensor face was shielded from half the omnidirectional flux and (2) the electrons in space are incident at all angles, whereas in the laboratory studies the electron irradiation was normal to the surface. The effective dose is thus considered to be about 10^{12} to 10^{13} electrons/cm^2 after 1 year in orbit.

The equivalent flux to each sensor, as previously defined, was from 10^{11} to 10^{12} electrons/cm^2-day. In the radiation ground tests, one of the flight sensors (designated sensor A) was irradiated to a total dose of 10^{13} electrons/cm^2. The two flight sensors on Explorer XXIII were exposed to the radiation environment long enough to receive a dose equivalent to that in the ground test. The two counts occurred in sensor A on February 5, 1965 (day 35 GMT) and on April 19, 1965 (day 108 GMT). No counts were recorded on sensor B, which was not irradiated in ground tests.

The pressurized-cell data indicated that no more than about 10 penetrations would be expected in the capacitor detectors. If the same number of radiation-induced pulses occurs in flight as occurred in the ground tests, their frequency of occurrence, like that of the penetrations, would be low. It is of interest that the two counts occurred relatively early in the flight whereas ground tests indicated that the first radiation-induced count would have been expected near the end of the 1-year flight time if the assumed space radiation flux is accurate. The range of uncertainty in flux, however, precludes any attempt to predict accurately when and to what extent radiation-induced pulsing might be expected. Although it is inconclusive as to whether the two discharges observed in flight were caused by penetrations or by radiation effects, the experiment does indicate that any radiation-induced pulses in excess of 2 V are at a minimum and would not likely affect meteoroid flux data to any great extent in this type of sensor when the penetration rates are relatively high.

The two counts recorded for the capacitor detector are somewhat less than the expected number of meteoroid penetrations. For an equivalent exposed area, the pressurized cells experienced about 10 punctures. This difference in counts could be due to (1) the difference in sensitivity between the two sensors and (2) the available level of the capacitor bias voltage. As discussed previously, pressurized cells appear to be more sensitive than capacitors in recording penetrations. A comparison of such data in figure II-8 indicates that a 25-micron capacitor detector would probably indicate about half as many penetrations as a 25-micron pressurized-cell detector. Hypervelocity impact tests of sample capacitor detectors in which various levels of detector bias voltage were used have shown that a capacitor bias voltage of about 60 V to 120 V dc was more desirable for recording penetrations than the -13 V dc potential used for the flight sensors. Tests conducted on flight-type detectors showed that in about 96 percent of the penetrations of a capacitor charged to -13 V dc, the discharge voltage fell below the threshold of the Explorer XXIII capacitor-detector signal conditioning units.

The maximum temperature variation of the sensors as measured by a thermistor temperature-sensing element was -40° C to 100° C. This temperature range is well within the ground-test temperature range and does not exceed the operating limits of the sensors.

CONCLUSIONS

Two counts were recorded by the capacitor-detector experiment during the 1-year reporting period. It is inconclusive as to whether the two discharges observed in flight were caused by penetrations or by radiation effects. The capacitor-detector monitoring circuit indicated that both detectors maintained bias voltage during the 1-year period.

APPENDIX

CAPACITOR-TYPE PENETRATION-DETECTOR DEVELOPMENT

The development of a capacitor-type penetration detector at the Langley Research Center has included an extensive environmental test program. These tests have included electron irradiation, temperature cycling in vacuum, vibration, and hypervelocity-projectile impact. Ten detector units were fabricated for use in environmental tests and in the flight program. The 10 detector units were fabricated from the same material batches in order to keep the units as nearly identical as possible. Six of the 10 detectors were designated as test units and were used for the environmental tests. Additional test samples were fabricated for impact tests. Two of the 10 detectors were designated as flight units and two were used as flight backup units.

Environmental Testing

Electron irradiation tests.- A sensor configuration of the type flown on Explorer XXIII was irradiated in the materials radiation laboratory at the Langley Research Center to determine its performance in the radiation environment. The tests were conducted at room temperature (approximately 25° C) with a flux of 10^{10} electrons/cm^2-sec. Ten runs were made on the sensor, each at a different electron energy level, to cover, in increments of 100 keV, the energy range from 100 keV to 1000 keV. In each run the sensor received a total dose of 10^{13} electrons/cm^2. The minimum number of pulses observed in any run was zero and the maximum number observed in any one run was six. Twenty pulses were observed for the 10 runs.

Thermal vacuum tests.- Each of the 10 detectors was vacuum soaked for a minimum of 96 hours at a pressure of 1×10^{-5} mm Hg. During the vacuum soak the detectors were heated and cooled by quartz-tube radiators and liquid nitrogen coils, respectively. Each detector was cycled a minimum of four times. During the testing each detector was charged to a -13 V dc potential through a flight-type signal conditioning circuit. The output of the signal conditioning circuit was monitored with a recording oscilloscope. In addition, some detectors were monitored during each test with a high-frequency-response oscilloscope.

Each of the detectors was tested from -80° C to 120° C with continuous electrical measurements made during each thermal cycle. After approximately 48 hours of vacuum soak and 1 to 2 thermal cycles, the leakage current through the capacitor became constant. The capacitance of the 10 detectors ranged from 0.111 μF to 0.122 μF measured at 1000 Hz. The capacitance value for the detector changed approximately 10 percent

for the full temperature cycle. No discharging or shorting was observed during the thermal vacuum testing.

Vibration tests.- Some detector units were given vibration tests through the entire vibration spectrum used in payload vibration tests. These tests were designed to determine the structural integrity of the printed wiring, the pin connections, the laminate of PET film and stainless steel, and the assembled unit. In addition, prototype and flight units were vibration tested on their respective payloads. No electrical or mechanical difficulties were observed during these tests.

The vibration spectrum and levels for these tests are shown in the following table:

Frequency, Hz	Amplitude, g	Sweep rate, octaves/min
20 to 2000	1	2
75 to 500	6	2
500 to 2000	12	2
50 to 70	6	2
40 to 70	3 for 24 sec	
Random, 20 to 2000	11.3 root mean square for 240 sec	

Hypervelocity-projectile impact tests.- Projectile impact tests were run on many capacitor-detector test samples. Borosilicate spheres, approximately 50 microns in diameter, were accelerated by means of an electrical-discharge type of small-particle accelerator to velocities ranging from 3 km/sec to 20 km/sec.

A number of sample capacitor sensors measuring approximately 9 by 9 cm were tested in the electric-discharge small-particle accelerator. Each sensor sample was biased with a -15 V dc potential and monitored on an oscilloscope to determine the discharge amplitude and wave form when the sensor was penetrated. The average signal amplitude of the discharges resulting from penetrations varied from approximately 5 mV to 12 V with 98 percent of the amplitudes below 1.2 V. The wave form consisted of a 90-percent discharge in less than 1 μsec.

In addition to the test samples previously discussed, four full-sized flight-type detectors with a signal conditioner unit were tested in the electric-discharge small-particle accelerator. The full-size detectors in these tests were also biased with -15 V dc. Twenty-three tests were made with from one to eight particles impacting the detector in each test and with at least one particle exceeding 8 km/sec in each test.

APPENDIX

In most capacitor-detector impact tests a photomultiplier is placed behind the sensor, as in the series of tests on sample sensors, to detect the flash resulting from a complete penetration. Since the four flight-type detectors were mounted on foam and an opaque backing (see figs. III-1 and III-3), the photomultiplier could not be used to obtain positive identification of complete penetrations. To identify complete penetrations the surface of each detector was scanned with a ×30 microscope. This method is not as reliable as the penetration-flash photomultiplier technique. A photomultiplier was used to detect the impact flash on the front face of the detector. A total of 25 complete penetrations were found by the microscope method in 23 tests. Fourteen discharges were recorded with discharge amplitudes varying from about 0.1 V to 2.0 V. The one 2.0-V discharge triggered the signal conditioner unit and registered a count. The remaining discharges did not have sufficient amplitude to trigger the signal conditioner unit, since in both the ground test and the flight electronics at least 2.0 V were required to activate the circuit.

A typical capacitor discharge from a hypervelocity-projectile penetration is shown in figure III-6. Impact tests were conducted on sample capacitors with a number of different impressed voltages. This figure illustrates the wave form which was typical of all tests. The two oscilloscope traces shown are for the same discharge but were obtained at different sweep speeds. In the upper beam the trace was swept at 100 μsec/division and the lower beam was swept at 1 μsec/division. The ringing in the early part of the sweep in the lower beam was found to be characteristic of the oscilloscope used.

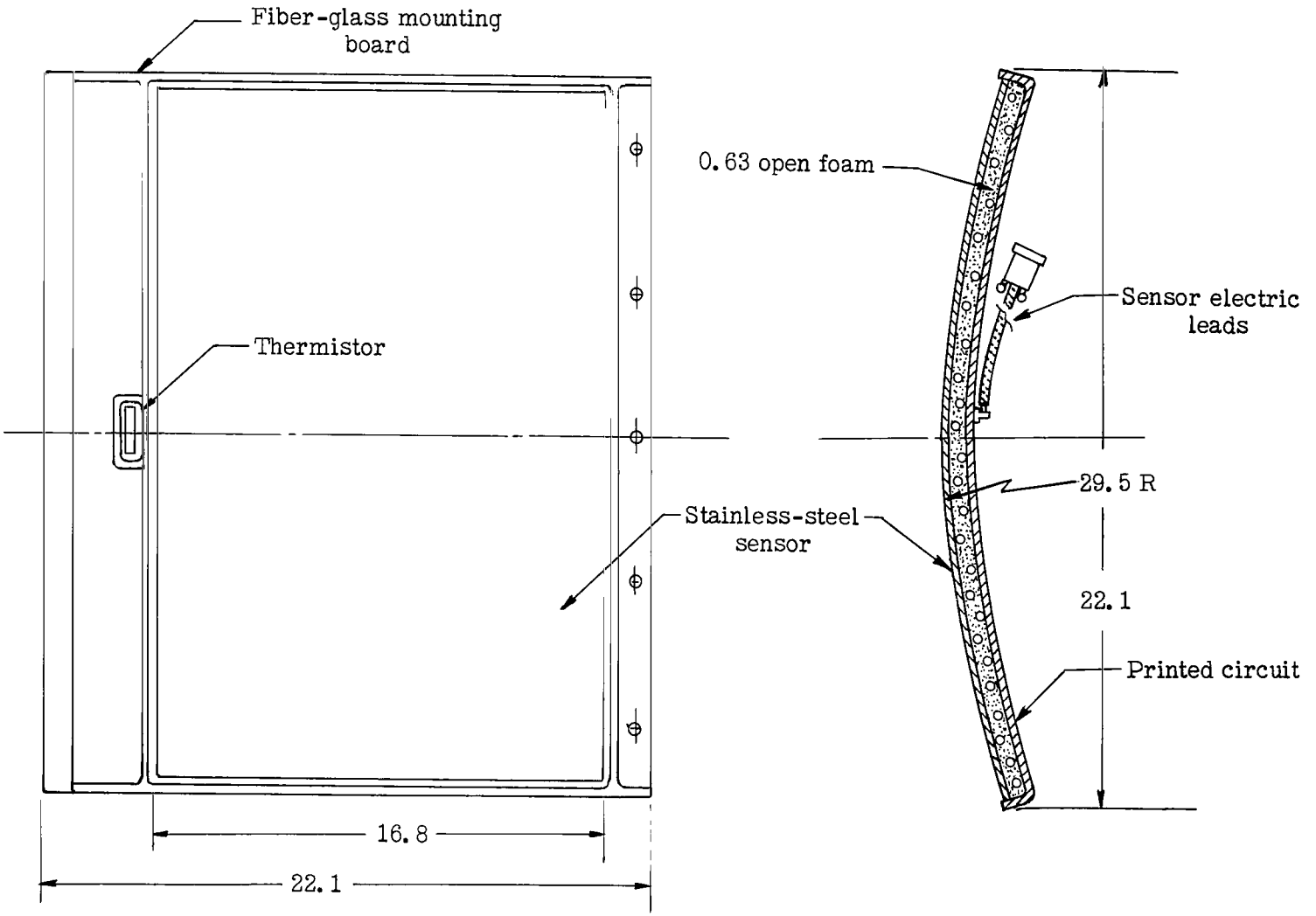

Figure III-1.- Capacitor-type penetration detector. All dimensions are in centimeters.

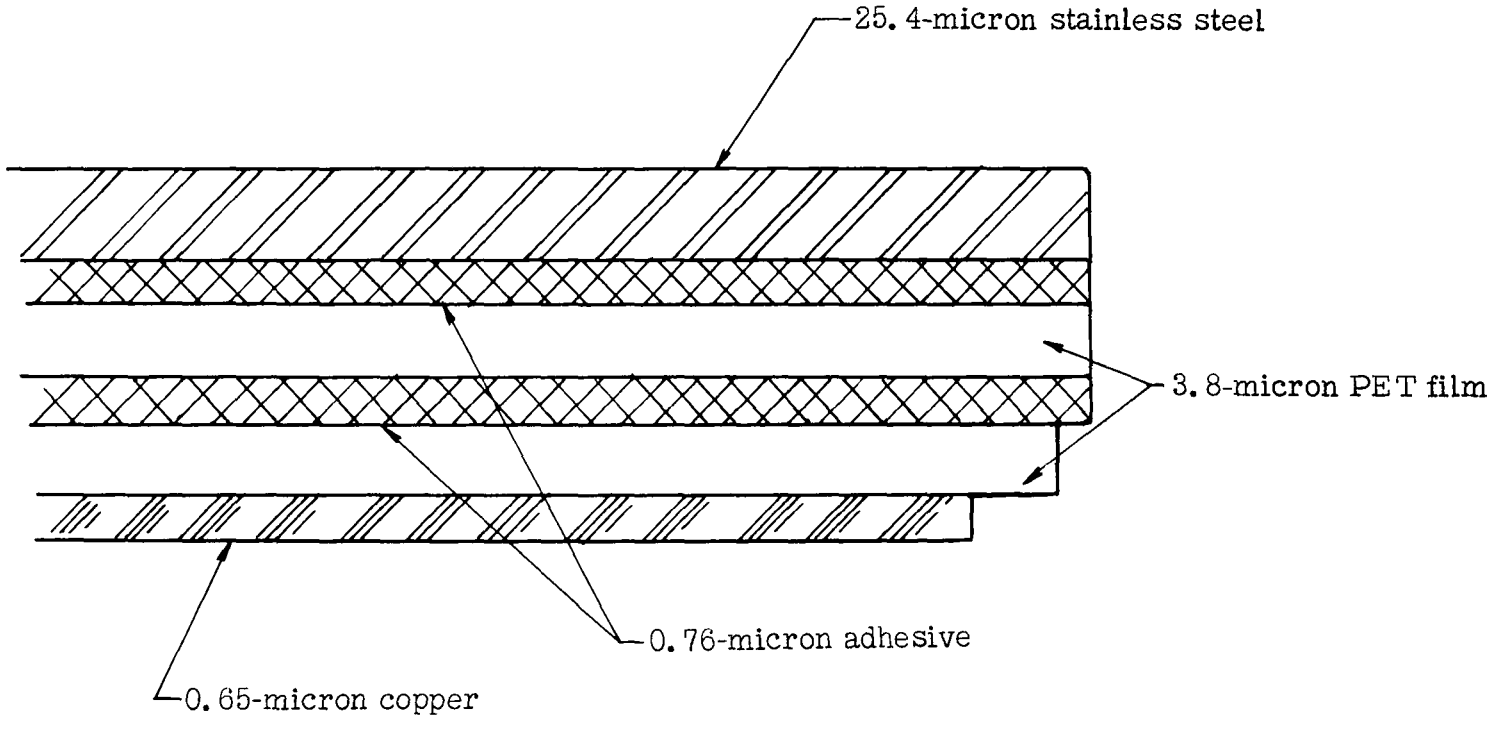

Figure III-2.- Typical cross section of capacitor-type penetration detector.

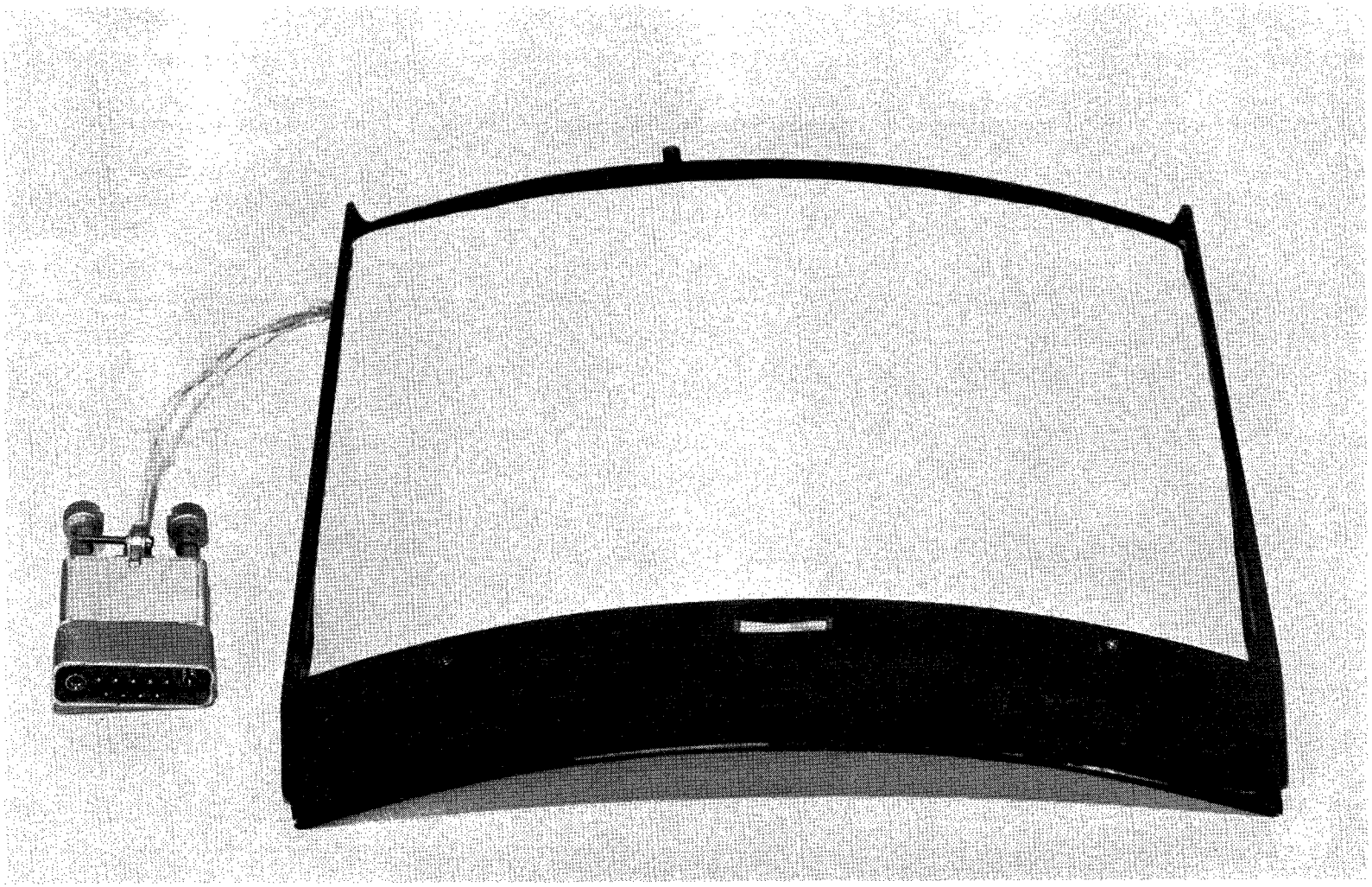

Figure III-3.- Photograph of capacitor-type penetration detector.

L-64-8916.1

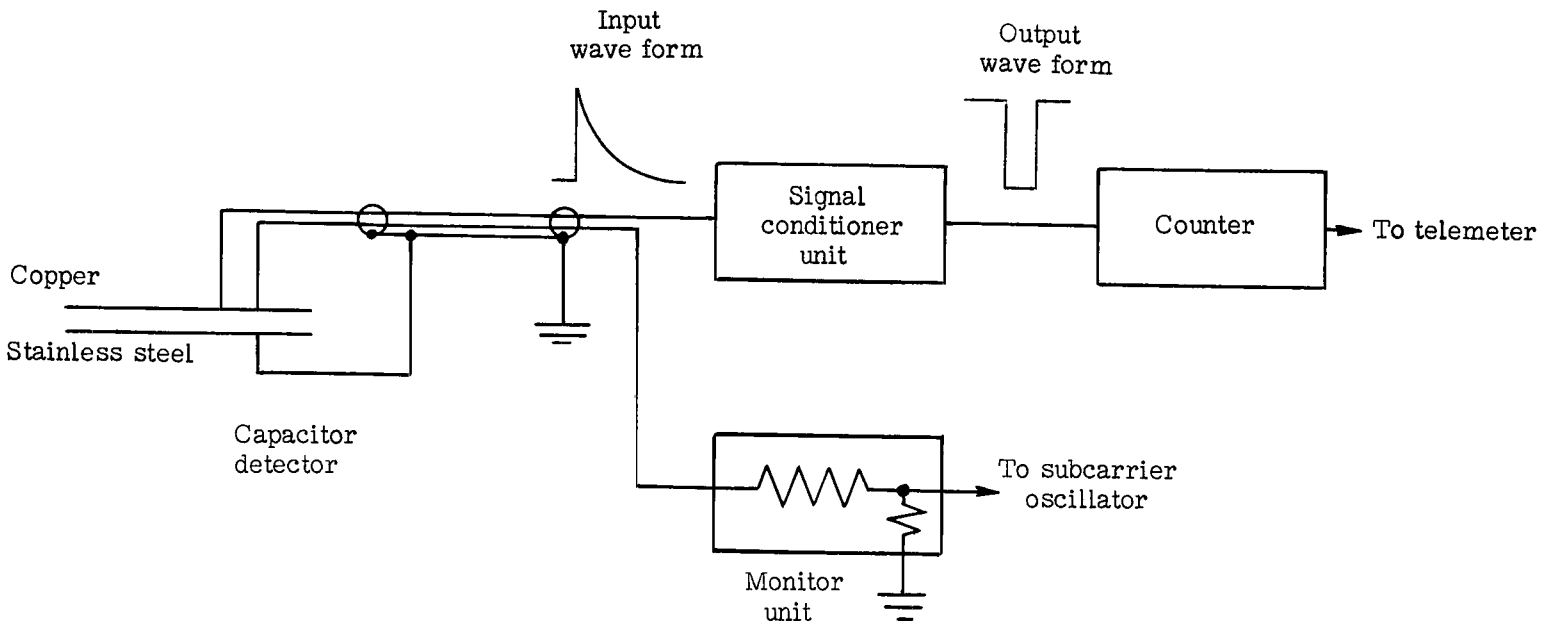

Figure III-4.- Block diagram of capacitor-detector circuitry.

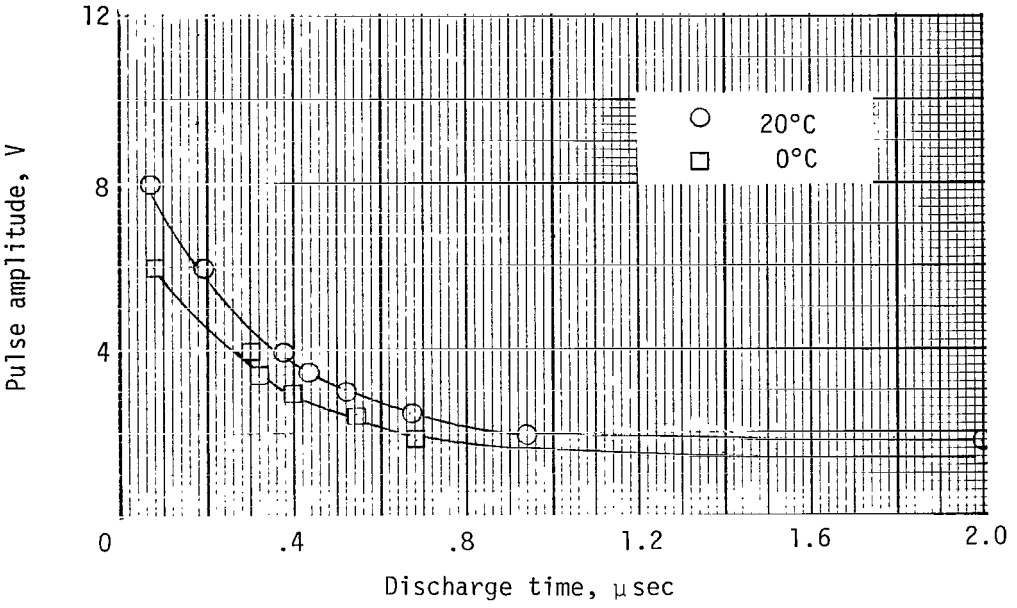

(a) Calibration of signal conditioning unit for sensor A.

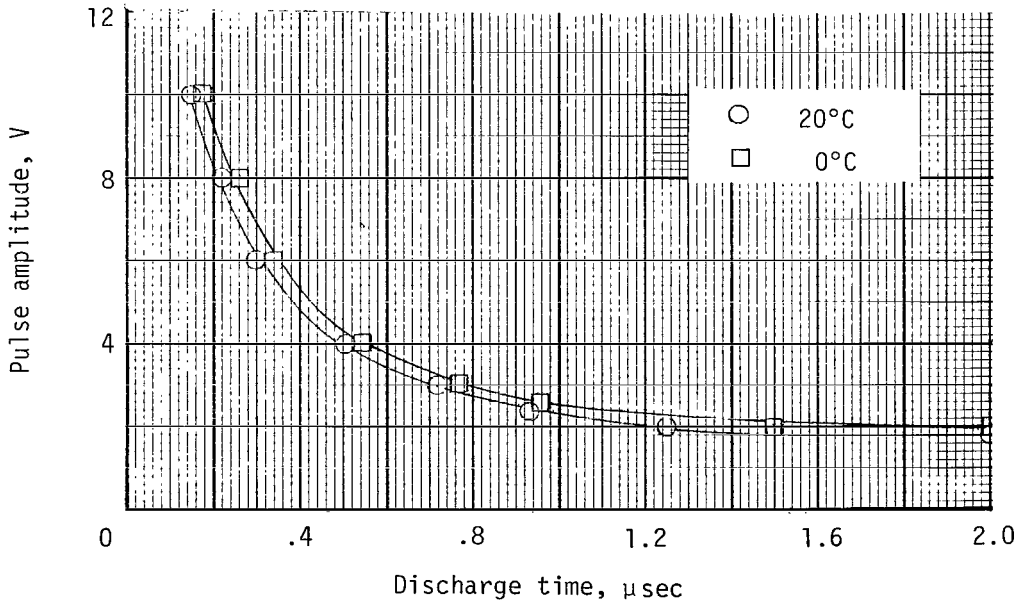

(b) Calibration of signal conditioning unit for sensor B.

Figure III-5.- Calibration curves of capacitor-detector signal conditioning units.

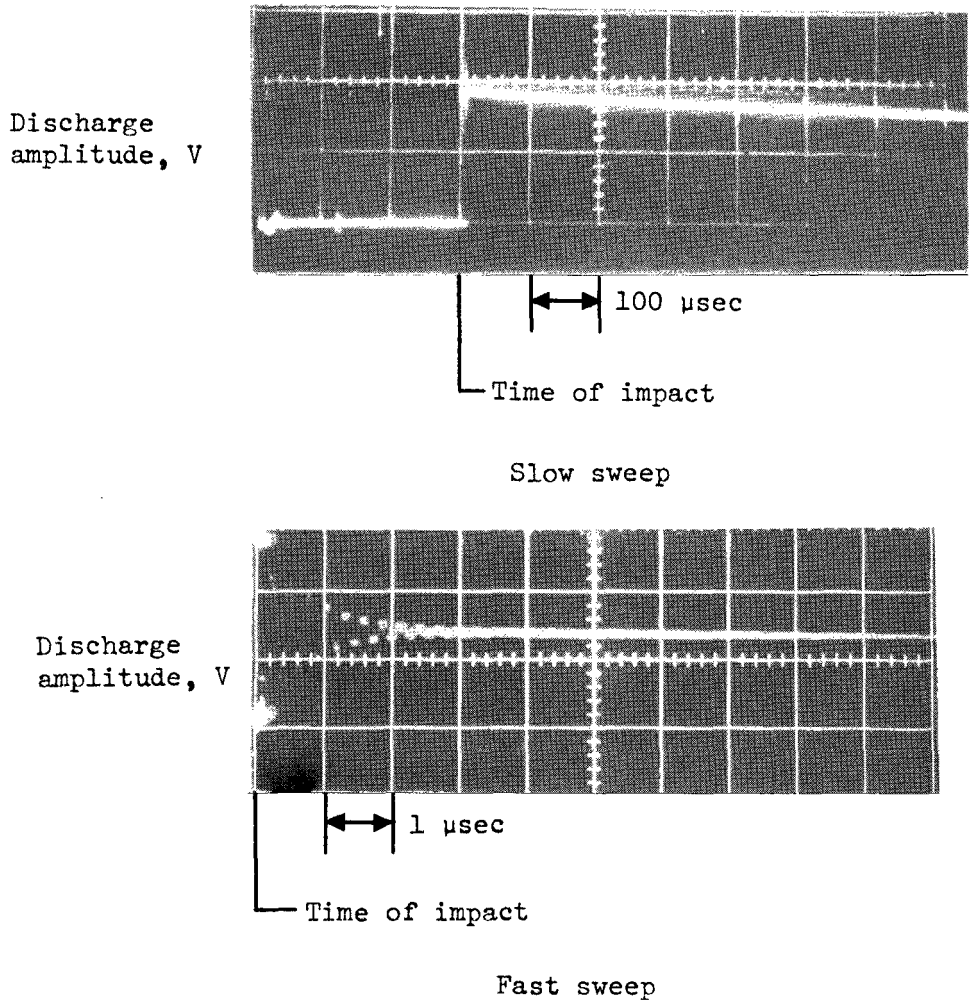

Figure III-6.- Typical oscilloscope photograph of capacitor-detector discharge from a hypervelocity-projectile penetration.

IV. IMPACT-DETECTION EXPERIMENT

By Dale G. Holden and Alfred G. Beswick
Langley Research Center

DESCRIPTION

The meteoroid-impact-detection system was designed to measure a mass distribution of meteoroids in space. The impact-detection system had three levels of sensitivity which were assumed to correspond to three levels of momentum. By assigning a velocity to the particles impacting in space, the system output was directly related to threshold levels of particle mass.

The meteoroid-impact-detection system consisted of 24 triangular sounding boards with attached piezoelectric transducers. A meteoroid impacting on a sounding board caused an electrical signal to be produced from the transducer. The electrical signal was amplified, threshold detected, counted, and stored until readout by interrogation of the satellite telemeter. An overall block diagram of the system is shown in figure IV-1. As seen in this figure, there were four groups of sounding boards with each group consisting of six boards electrically paralleled. Each group of boards had an electronic amplifier, and all four amplifiers were electrically identical. Each of the amplifiers has three stages of amplification corresponding to the low, medium, and high sensitivity ranges. The outputs from the one, two, or three stages of amplification in each of the four amplifiers were threshold detected and fed to their respective signal conditioners. There was one signal conditioner and counter storage unit for each of the three threshold sensitivity levels. The capacity for each of the high and medium sensitivity storage counters before recycling was 1024 counts, and the capacity for the low sensitivity counter was 64 counts. The system sensitivity was adjusted during final calibrations so that all 24 sounding boards acted as a single detector for all three sensitivity levels.

Each of the triangular sounding boards had an effective area of 6.0×10^{-3} meter^2; thus, the total exposed area for the 24 boards was 1.44×10^{-1} meter^2. Figure IV-2 shows a sketch of a typical sounding board. The board was made of 0.13-centimeter-thick 6061 aluminum alloy, slightly curved to fit around the periphery of the spacecraft, and coated for thermal control. A lead-zirconate-titanate piezoelectric transducer element was mounted on the underside and in the center of the sounding board. This mounting is shown in figure IV-3. Figure IV-4 shows an exploded view of the transducer mounting assembly. The transducer element produces an electrical signal when disturbed by a mechanical force along its poled axis which is perpendicular to the surface of the sounding board. The electrical output produced by the transducer element is

picked off by the metal tabs on either end of the element and fed by triaxial cable to the amplifier for processing.

The electronics used in the system are basically the same as those used for the impact detectors mounted on some of the pressurized cells of Explorer XIII (ref. IV-1) and Explorer XVI (ref. IV-2). The only differences are the replacement of the solid-state devices used in the earlier system with improved types and the addition of temperature-compensating circuitry to improve gain stability of each amplifier throughout the operating temperature range.

The impact detectors were calibrated with the assumptions that the system response is proportional to the meteoroid momentum and that the response to hypervelocity impacts could be simulated by dropping large, low-velocity projectiles on the sounding board. The calibration of the system was basically the same as that for Explorers XIII and XVI and was conducted as follows: Synthetic ruby spheres ranging from 1.3×10^{-8} to 1.2×10^{-4} gram in mass are dropped from known heights ranging from 2×10^{-2} to 1×10^{-1} meter under normal atmospheric conditions onto different areas of the sounding board and the electrical output from the piezoelectric transducers is recorded. From the relation $M = m\sqrt{2gh}(1 + e)$, the momentum M of the sphere is calculated, where m is the particle mass, h is the drop height, g is the particle acceleration due to gravity, and e is the coefficient of restitution as determined from the rebound height measurements of the impacting spheres.

Holding the spherical mass and the drop height constant, 10 or more ball drops on predetermined areas of each sounding board were made and the electrical outputs recorded. By utilizing this information, sounding boards exhibiting similar electrical outputs were selected to make up four groups of 6 boards each for a total of 24 sounding boards. These four groups of sounding boards were then mated to their associated electronic amplifiers, and system calibration was accomplished by adjustment of the electronic amplifier gains and detector threshold characteristics for each of the three desired sensitivities by utilizing the synthetic-ruby-sphere drop technique previously described. Final system calibration was made after the sounding boards were mounted to the spacecraft structure. The ball drop technique allowed a low-velocity, large-mass momentum figure to be calculated for each of the three threshold levels. It is assumed that the figure calculated is valid for the relatively high-velocity, small-mass particles expected in the meteoroid environment. The thresholds calculated for the high, medium, and low ranges, respectively, are 3.0×10^{-7}, 8.0×10^{-6}, and 1.2×10^{-4} newton-second.

RESULTS AND DISCUSSION

The high sensitivity system of the meteoroid-impact-detection system recorded 14 169 counts, the medium sensitivity system recorded 218 counts, and the low

sensitivity system recorded 2 counts for the 365-day reporting period. The number of counts recorded for the high and medium sensitivity systems in each 24-hour interval of the reporting period is shown in figures IV-5 and IV-6. The two low-sensitivity-range counts were recorded on the 42d and 206th day of 1965. The data as recorded were necessarily subject to interpolation because of the distribution of interrogations for each day. A straight-line interpolation between the last interrogation of one 24-hour interval and the first interrogation of the next interval was used to resolve the number of counts between the two interrogations.

The high-sensitivity-range data presented in figure IV-5 show counting activity occurring in groups with an order-of-magnitude increase during the last half of 1965. With the exception of a very few counts, the medium-sensitivity-system data in figure IV-6 show counts occurring at the same time as very active periods are noted in the high sensitivity system. Of the 218 total counts for this system, 176 occurred within a 2-week period beginning at about the 200th day of 1965. The groupings of meteoroid activity with orders of magnitude variation between active and quiet periods were not found in the penetration measurements. As discussed in chapter II, only small variations from the average penetration rate were observed in the pressurized-cell data. It is of interest that the microphone system on Explorer VIII (ref. IV-3) recorded large variations of at least plus or minus an order of magnitude from the mean within intervals of a few hours for particle masses of about 10^{-9} gram.

Figure IV-7 shows the high, medium, and low sensitivity ranges of data on a particle-impact-rate basis as a function of particle mass. The effective particle mass sensitivity of each system in grams was obtained by assuming that each of the three system sensitivities is directly related to the momentum of the impinging particle and also assuming an average particle velocity of 22 kilometers/second and then calculating the three mass sensitivities by using the previously determined momentum figures. The impact rate shown for each of the three ranges was obtained by taking the total counts recorded for each range and dividing by the total number of seconds of exposure (365-day period) and the total exposed area of 1.44×10^{-1} meter^2.

Particle impact rates measured by Explorer VIII and Explorer XVI are also shown in figure IV-7. The pressurized-cell penetration rates and the Whipple 1963 estimate of the penetration rate have been converted to a particle-mass basis and included for comparison. The Herrmann and Jones penetration equation (eq. (7) of chapter II) and the factor for converting from semi-infinite targets to thin sheets (eq. (8) of chapter II) were used to relate material thickness penetrated to particle mass.

A comparison of the impact-rate data as measured by the impact detectors shows Explorer XXIII rates to be about an order of magnitude above Explorer VIII rates and significantly less than Explorer XVI rates. Although the decrease in impact rate with

increasing particle mass for Explorer XXIII and Explorer VIII agree well with the Whipple estimate, the decrease is much greater than indicated by Explorer XXIII penetration measurements. Uncertainties exist in the application of laboratory-developed penetration equations and assumed meteoroid properties to relate meteoroid-penetration data to penetrating meteoroid mass. Uncertainties also exist in the assumption that momentum response at hypervelocity meteoroid encounter is the same as or even comparable with the observed momentum response of such systems at the low velocities employed for calibration. It is believed that such uncertainties could affect the magnitude; however, they would not explain the difference in the variation of impact rate with particle mass measured by the two systems.

The lack of agreement between the impact data and the penetration data and the peculiar grouping of the impact-system counting activity causes the impact data in the higher sensitivity ranges to be questioned. In an analysis of the Explorer XVI impact data in reference IV-2 there appeared to be a greater correlation between the temperature environment of portions of the satellite skin structure and impact activity than could be ascribed to chance or coincidence. An investigation has been made to determine whether such a condition existed in the Explorer XXIII impact data.

A comparison of the satellite percent time in sunlight with impact counts is shown in figure IV-8. There appears to be a good correlation of the data activity with the satellite percent time in sunlight. For example, whenever there is 90 percent or more time spent in sunlight, there is a corresponding reduction in recorded counts; and also the data activity increases after each period of 90 percent or more time in sunlight with a rate that appears related to the rate of change of the percent time in sunlight.

It is known that the temperatures throughout the satellite are directly related to the percent time in sunlight. With this fact in mind, the various effects which temperature variations would have on the sensors and electronic signal-conditioning systems of the prototype spacecraft were investigated in the laboratory. The initial results of these investigations indicated that there were no temperature effects in the electronics which could cause the anomalous behavior indicated in the data. However, further tests showed that the sounding boards themselves exhibited a tendency to generate signals resembling impacts under certain conditions of temperature change, and these signals were detectable only by the high sensitivity system. Generally, the spurious signals of significant detectable amplitude were produced when the sounding-board temperature was rapidly decreased from the highest to the lowest temperatures predicted for the satellite in any one orbit. The rate of temperature change used in the test was on the order of that predicted for the satellite during each orbit of the earth in a 60-percent sunlight period. The laboratory tests indicated that, in the high range, from zero to three counts could accumulate per orbit.

The telemetered temperature measurements on the back side of two sounding boards mounted 180° away from each other on the periphery of the satellite were studied in light of the laboratory tests. This study showed that the same correlation existed between the counting activity and the band of measured sounding-board temperatures as that previously discussed for the percent-time-in-sunlight curve and the high-range-data plot of figure IV-8. However, the interrogation rate was such that it precluded any possibility of defining the rate of temperature change encountered by any one sounding board, but it is possible that at least one sounding board in one orbit of a 24-hour period was subjected to a rate of temperature change similar to the predicted rate used in the laboratory tests.

CONCLUSIONS

From the study of the impact data and the laboratory investigations of the impact-detection system, it is concluded that the high-sensitivity-range data probably contain false impact counts caused by sensor temperature effects. It is not possible to determine how many counts were caused by temperature effects because of the improbability of achieving identical system performance in the laboratory under simulated environmental conditions and also because of differences which may exist between the impact-detection system for the flight and prototype spacecraft. The laboratory tests did not show the medium-sensitivity system to be affected by temperature; however, the same test limitation prevents a positive conclusion concerning validity of this range of flight data. In general, data for the higher sensitivity ranges are questionable because of the apparent temperature sensitivity and lack of agreement with penetration data. Although the converted data from the low sensitivity system are near the level of pressurized-cell data, little confidence can be placed in the relatively poor statistical sampling of impacts.

REFERENCES

IV-1. D'Aiutolo, Charles T., coordinator: The Micrometeoroid Satellite Explorer XIII (1961 Chi) – Collected Papers on Design and Performance. NASA TN D-2468, 1964.

IV-2. Hastings, Earl C., Jr., compiler: The Explorer XVI Micrometeoroid Satellite – Supplement III, Preliminary Results for the Period May 27, 1963, Through July 22, 1963. NASA TM X-949, 1964.

IV-3. Alexander, W. M.; McCracken, C. W.; Secretan, L.; and Berg, O. E.: Review of Direct Measurements of Interplanetary Dust From Satellites and Probes. Goddard Space Flight Center Contributions to the COSPAR Meeting May 1962, NASA TN D-1669, 1963, pp. 39-60.

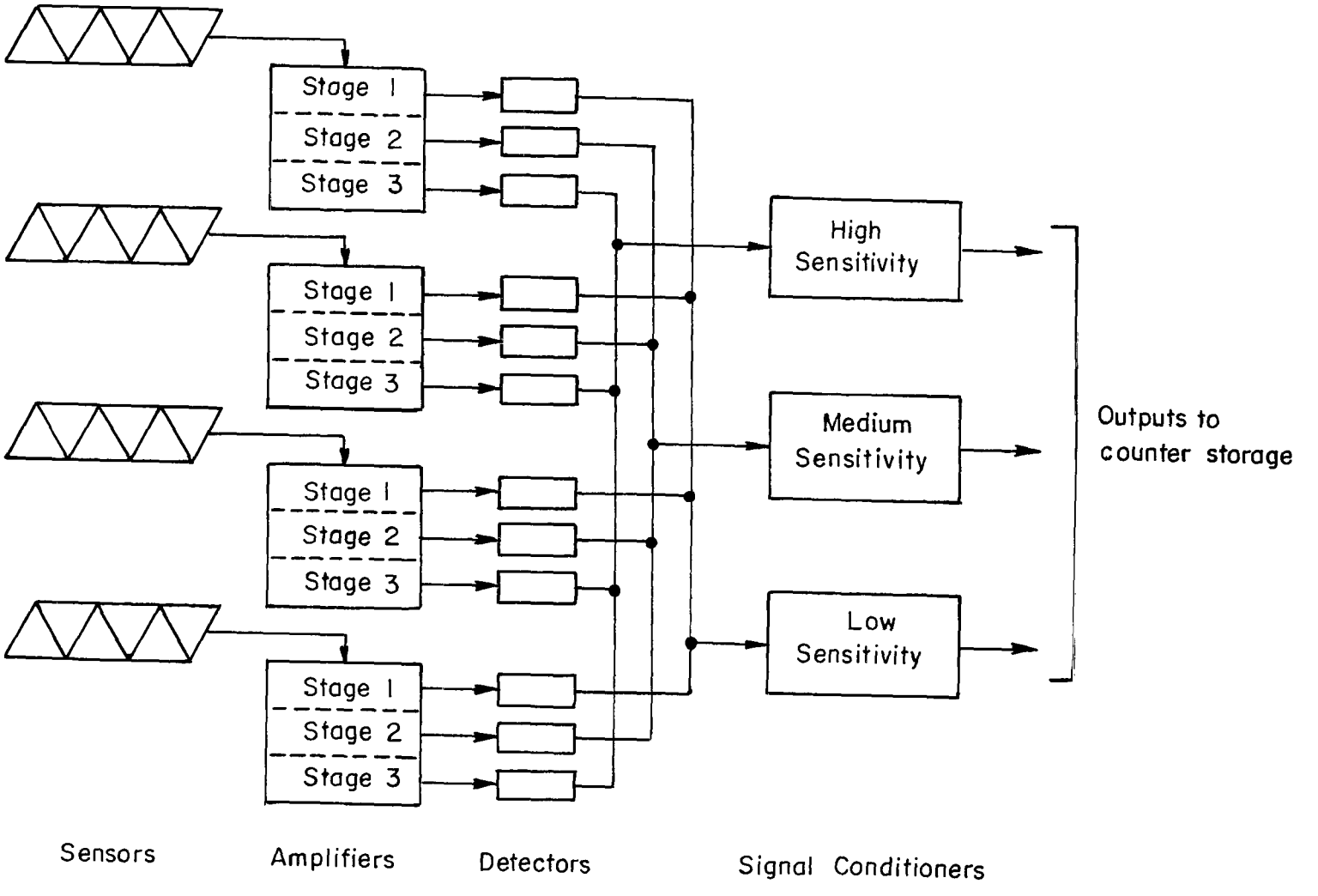

Figure IV-1.- Block diagram of micrometeoroid-impact-detection system.

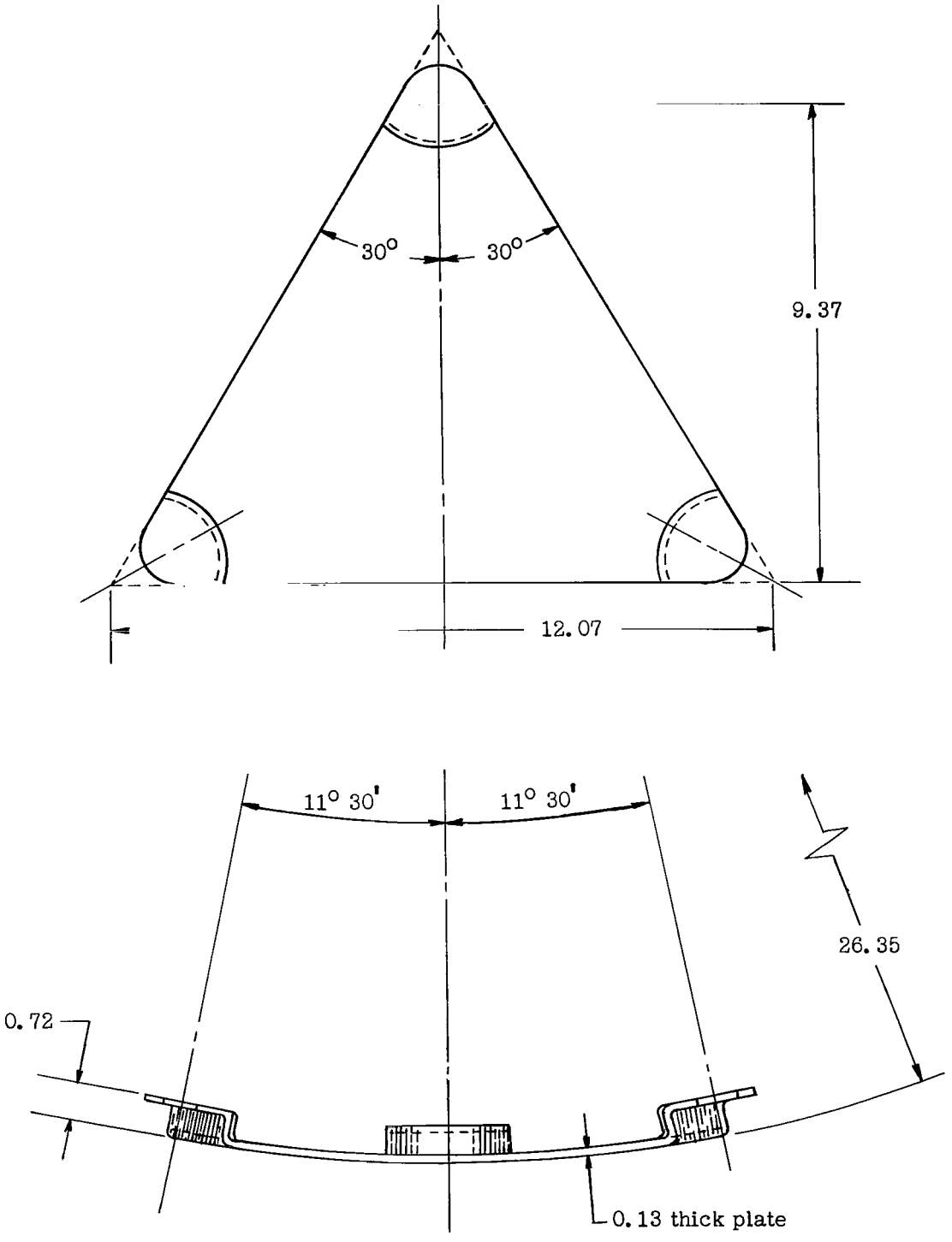

Figure IV-2.- Typical sounding board. All dimensions are in centimeters unless otherwise noted.

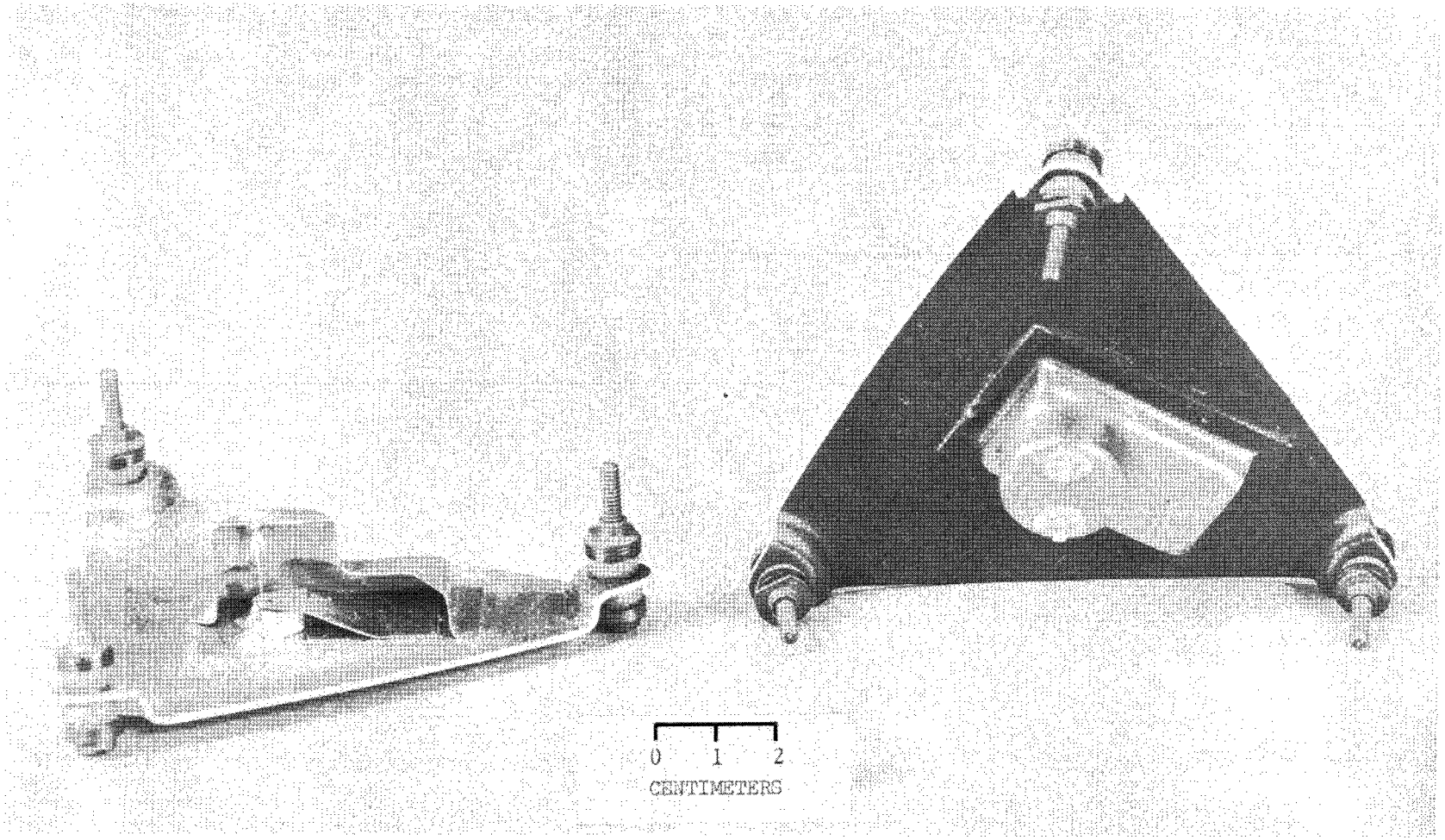

Figure IV-3.- View of back side of typical sounding board showing transducer mounting and shielding technique. L-64-56

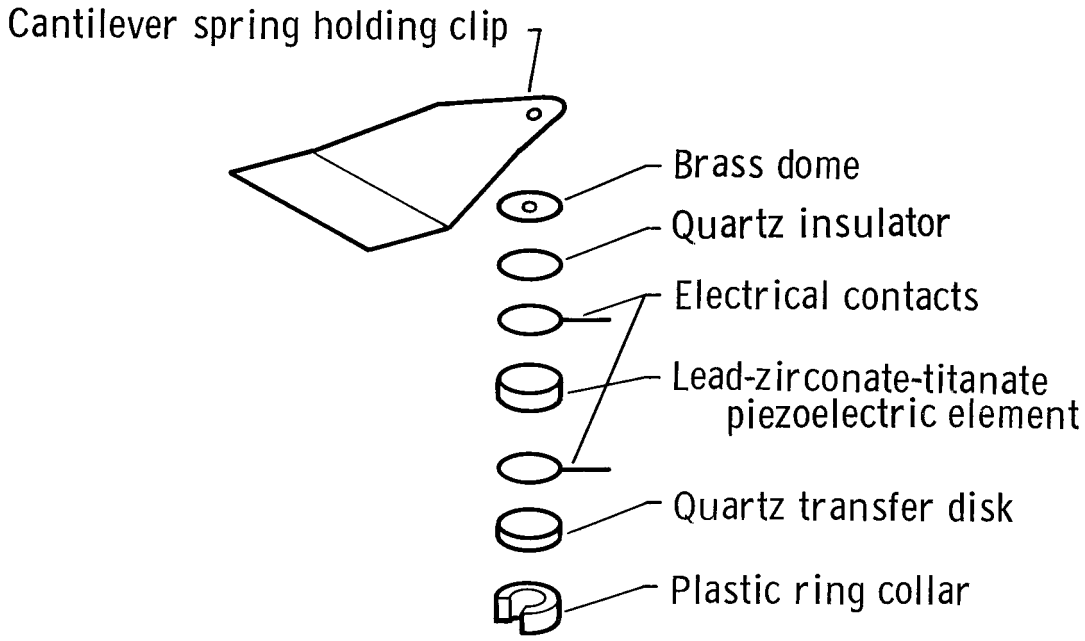

Figure IV-4.- Exploded view of piezoelectric impact-detector assembly.

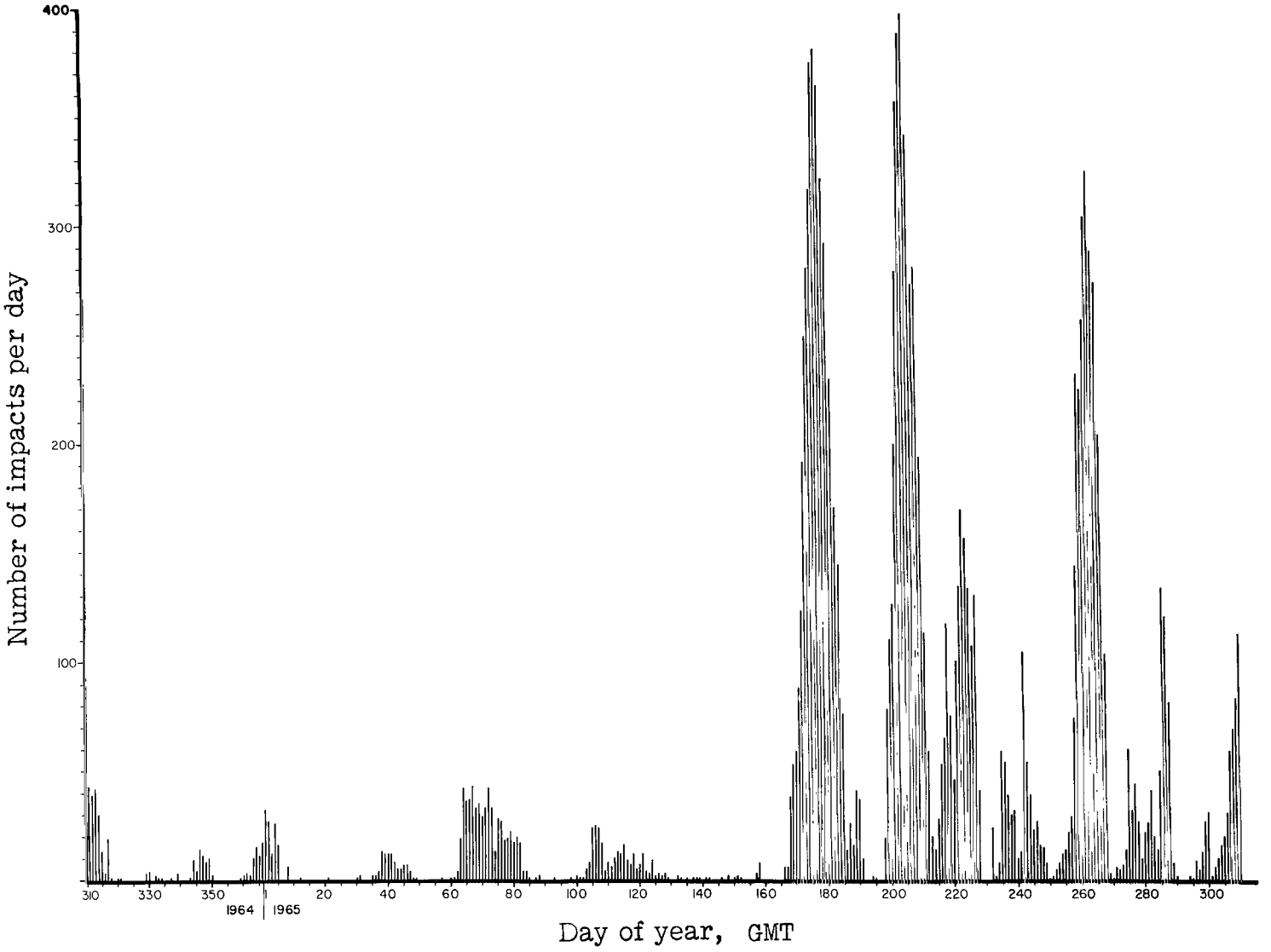

Figure IV-5.- Daily impact accumulation for the high sensitivity range of the micrometeoroid-impact-detection system.

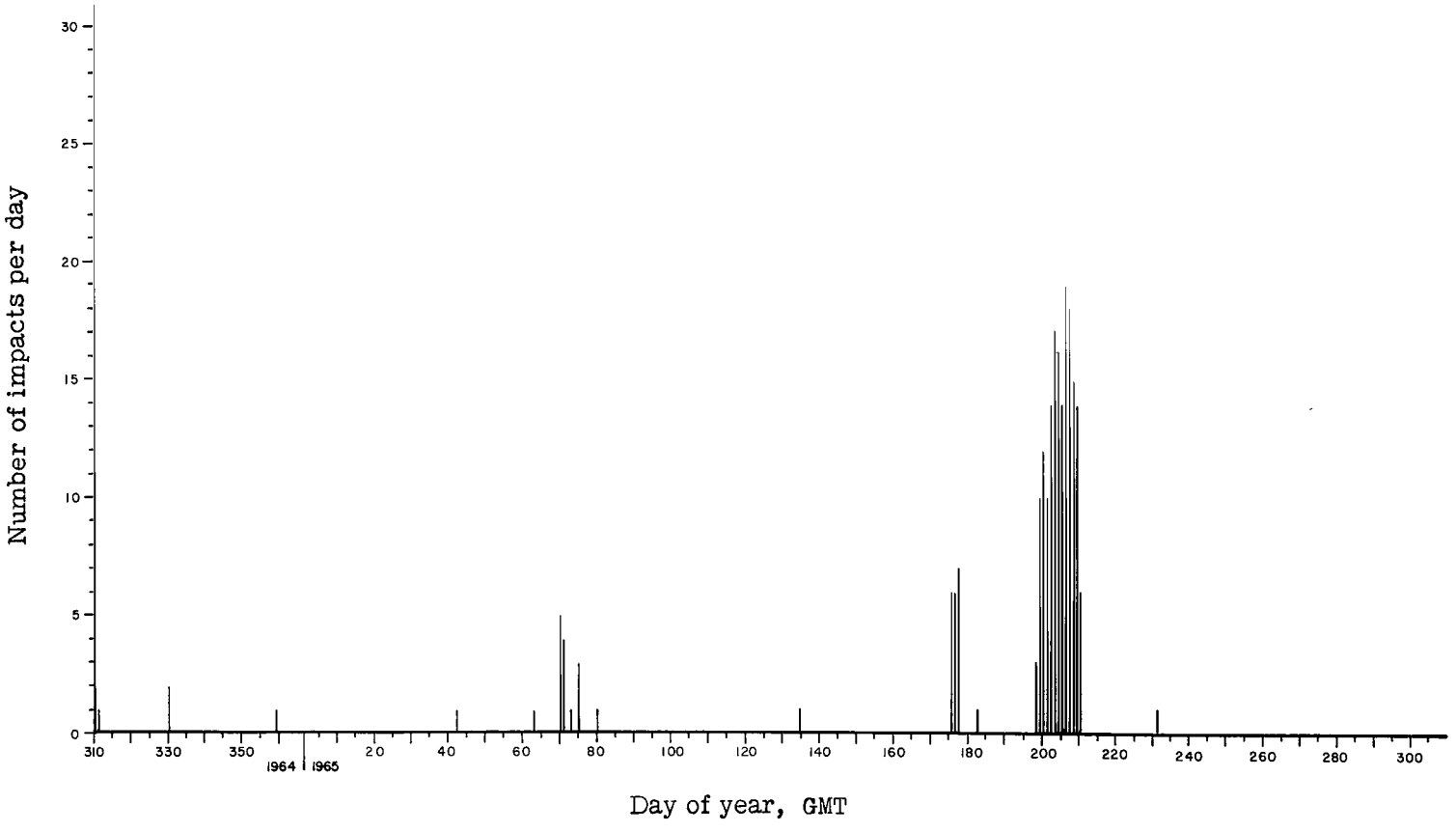

Figure IV-6.- Daily impact accumulation for the medium sensitivity range of the micrometeoroid-impact-detection system.

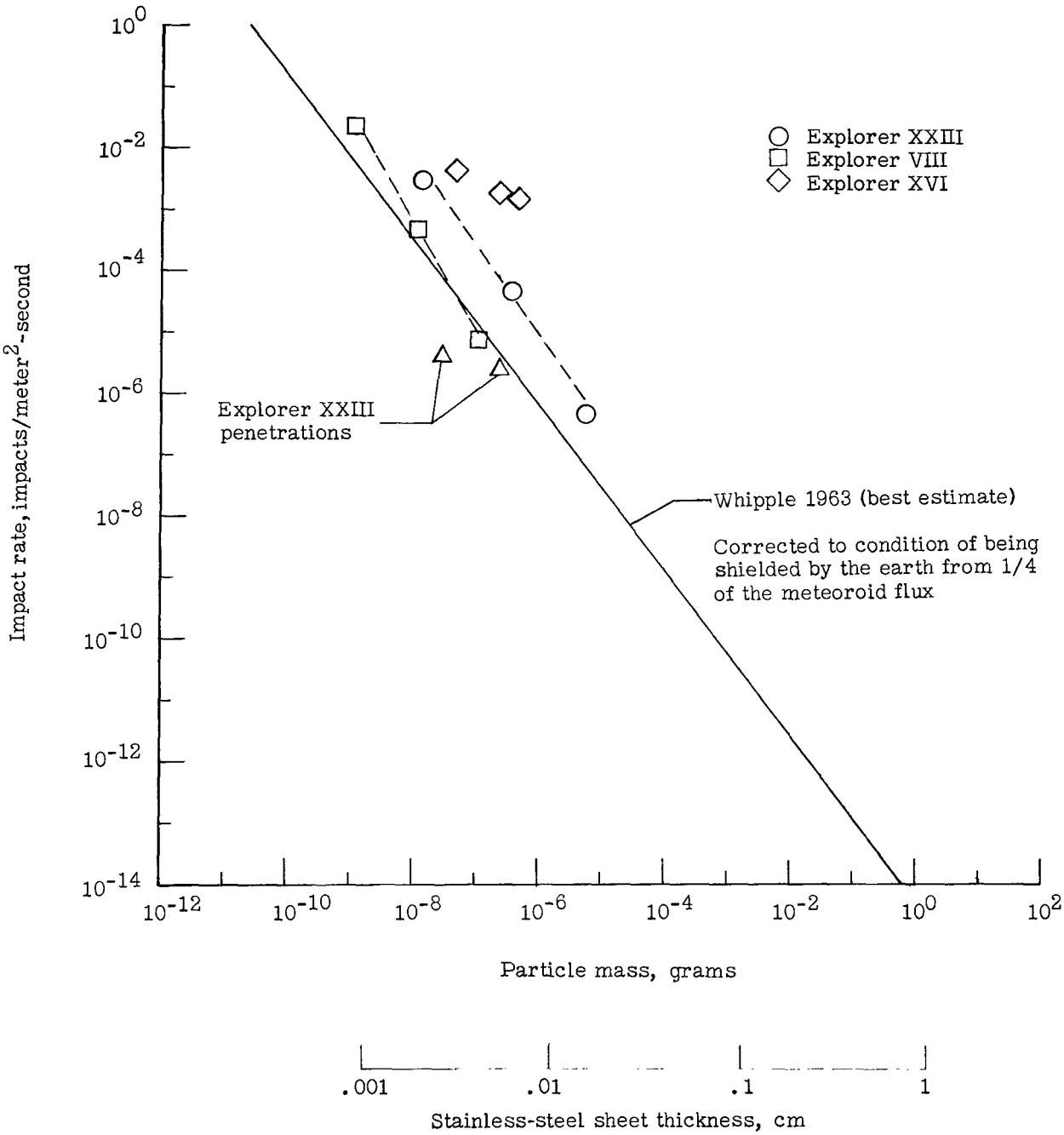

Figure IV-7.- Comparison of impact data from Explorer VIII, Explorer XVI, and Explorer XXIII. Estimated flux and measured penetration rates in terms of impact rates are noted. (Assumed impact velocity is 22 km/sec.)

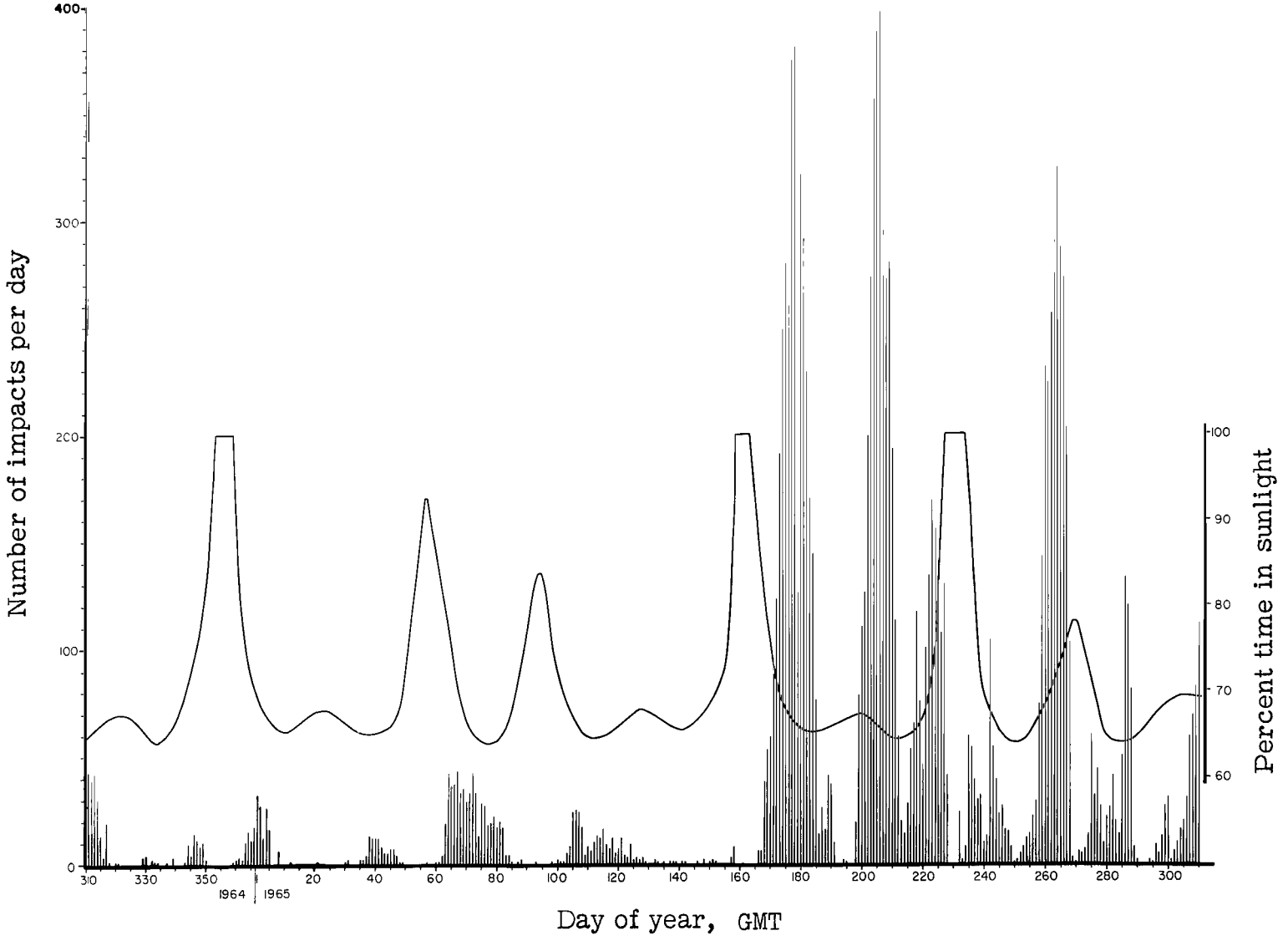

Figure IV-8.- Predicted percent time in sunlight for Explorer XXIII compared with high-sensitivity-range daily impact accumulation.

V. CADMIUM-SULFIDE-CELL-DETECTOR EXPERIMENT

By Luc Secretan
Goddard Space Flight Center

DESCRIPTION

The purpose of the cadmium-sulfide-cell-detector experiment was to measure the size of holes produced in two thicknesses of a plastic film by meteoroid penetrations. Such measurements would provide information regarding the size of the penetrating meteoroids.

The cadmium-sulfide-cell detector was developed by the Goddard Space Flight Center. A drawing of this detector is shown in figure V-1. The detector consisted of a light-sensitive cadmium-sulfide-cell element mounted beneath a sheet of PET film having evaporated aluminum on both sides. The useful surface area was about 3.44×10^{-3} m^2 per cell. Penetration of the aluminized PET sheet would allow sunlight (direct or reflected) to illuminate the cadmium-sulfide-cell element and reduce its resistance. This resistance change was monitored by the telemetry system. The detector system was calibrated to relate the resistance change to accumulative hole sizes in the PET film.

Two cadmium sulfide cells were mounted on the forward face of the spacecraft. One was mounted beneath a sheet of 6.35-micron PET film and one was mounted beneath a sheet of 3.18-micron PET film.

RESULTS

The cadmium-sulfide-cell detectors were the same type as those flown successfully on Explorer XVI. The detectors on Explorer XXIII were functioning properly during all interrogations made prior to lift-off, but on the first interrogation made shortly after fourth-stage burnout they were saturated with light. Apparently, the aluminized PET film covers were damaged during the launch and, thus, the detectors could not provide meteoroid-penetration data.

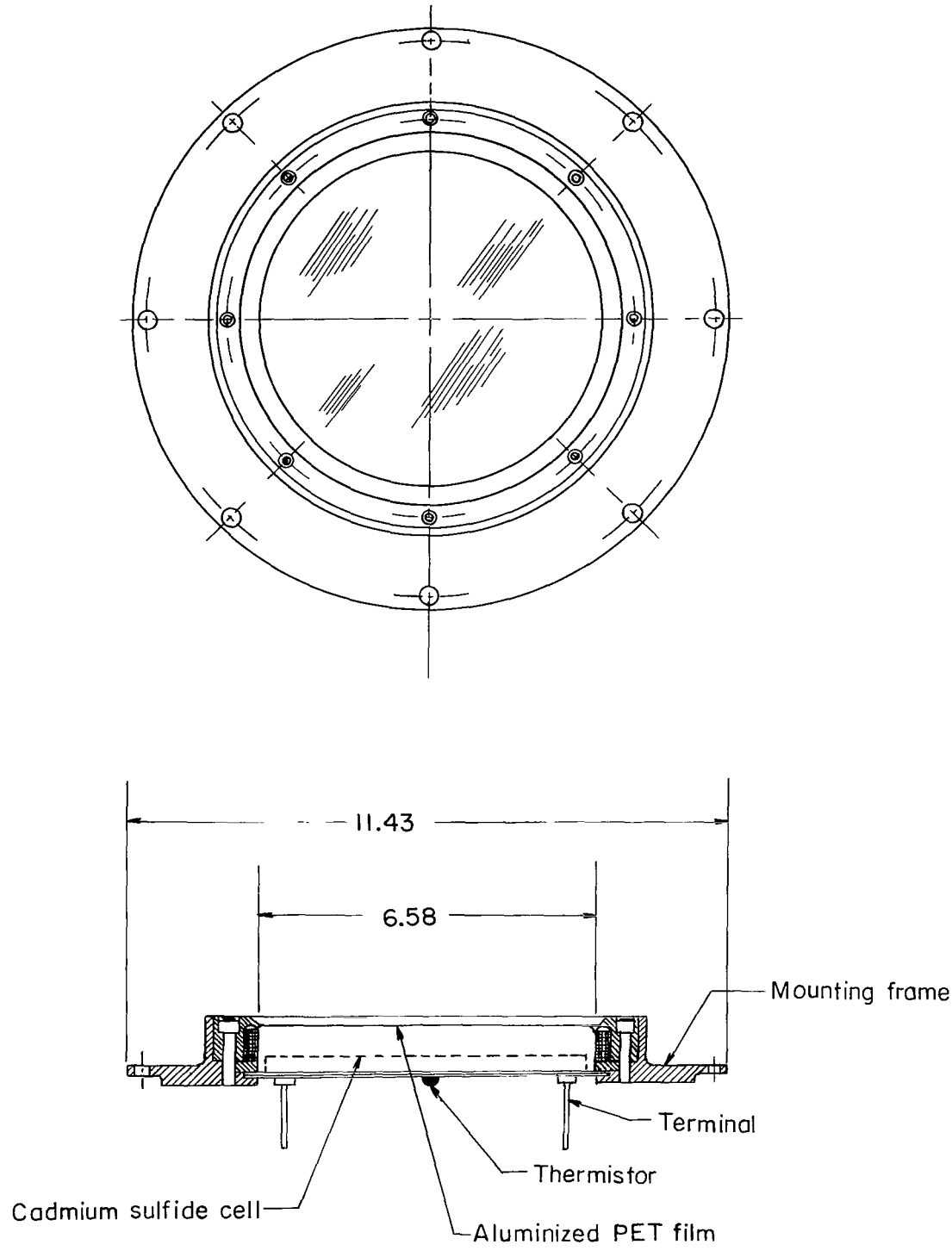

Figure V-1.- Sketch of cadmium-sulfide-cell detector. All dimensions are in centimeters.

VI. SOLAR-CELL IRRADIATION EXPERIMENT

By Walter E. Ellis and James Bene
Langley Research Center

DESCRIPTION

General

The purpose of the solar-cell irradiation experiment was to measure the degradation in performance of shielded and unshielded solar cells operating in the space environment. This was accomplished by monitoring the voltage output from solar-cell test groups during the mission and comparing the results with the original output. In order to isolate space environmental effects on performance, the solar-cell output voltages were corrected for solar angle of incidence, solar-flux variation, solar-cell temperatures, and earth-reflected solar radiation.

The solar-cell irradiation experiment consisted of a solar aspect sensor and four solar-cell test groups. These components were mounted in the same plane on the forward flat surface of the spacecraft as shown in figure I-2.

The solar aspect sensor shown in figure VI-1 provided the solar orientation data necessary to evaluate properly the data received from the solar-cell test groups. The sensor consisted of six triangular silicon solar-cell segments of the type used in the solar-cell test groups. These six segments were arranged in a hexagon and had a total effective area of 2.49 cm^2. The solar-cell segments were shielded with a synthetic fused silica cover, 0.636 cm thick, which provided a transparent window, 1.67 cm in diameter, centered over the solar-cell sensor.

Each triangular solar-cell segment was loaded with a 22-ohm, wire-wound, low-temperature-coefficient resistor. These six resistors were series connected to provide the necessary voltage output that was compatible with the telemetry system. This design provided a reasonably linear voltage output as a function of aspect angle and a minimum voltage output variation as a function of temperature over the range expected during the mission. A room-temperature-cure silicon adhesive was used to cement the solar cells to the sensor housing and to pot the resistors and electrical leads.

Each of the four test groups consisted of five, 1- by 2-cm, N/P, 1.0 ohm-cm, silicon solar cells of the type used in the primary power system. The cells in each group were series connected into a shingled configuration as shown in figure VI-2. Each group operated into a fixed load of 33 ohms. This was an optimum load, determined from

laboratory tests, to provide a reasonably high initial output voltage of approximately 1.9 volts at normal-incidence space sun illumination and to maximize linearity as a function of illumination intensity.

Test groups 1 and 2 were contained in the same module tray and were covered with a 0.476-cm-thick synthetic fused silica shield, identical to the shielding used over the solar cells in the spacecraft power system. Test groups 3 and 4 were contained in a similar tray but had no protective shield. The four test groups were oriented in the trays and mounted on the spacecraft so that the shingle angle was in the same direction for all groups.

The temperature of the solar aspect sensor was determined in flight by means of a thermistor mounted in the faceplate of the satellite, directly beneath the aspect sensor. The temperatures of the solar-cell test groups were determined by means of thermistors embedded in the base of each module tray.

The solar aspect sensor and solar-cell test groups 1, 2, and 3 were assigned adjacent channels in telemeter A. Solar-cell test group 4 was assigned to a channel in telemeter B.

Calibration

Figure VI-3 shows the normalized angular response of the solar aspect sensor as determined from ground calibrations. This curve represents the response as measured with incident illumination at angles from 0^{o} to $\pm 90^{o}$. The maximum deviation from this curve of measurements made at roll angles from 0^{o} to 180^{o} was less than ± 2 percent.

Figures VI-4 and VI-5 show the normalized angular response of the shielded and unshielded solar-cell test groups, respectively. These curves represent the averaged angular response of the two shingles in each tray as measured with incident illumination at angles from 0^{o} to $\pm 90^{o}$ and at tray roll angles of 0^{o}, 45^{o}, and 90^{o}. The maximum variation in angular response at any measured roll angle was less than 3 percent at angles of incidence less than 60^{o}. At larger angles of incidence, groups 1 and 2 exhibited greater variation in angular response because of the shadows caused by the shield retaining cover.

RESULTS AND DISCUSSION

General

The outputs of the solar aspect sensor and the four solar-cell test groups were determined by measuring the respective voltages developed while operating into fixed resistive loads under solar illumination. Interrogations of 1-minute duration were made during each orbit for the first month; after which three interrogations per day were

made until the end of the mission. These interrogations occurred during both sunlight and darkness periods. Inasmuch as solar cells are photovoltaic devices, only data from those interrogations made during sunlight periods were usable for this experiment.

A listing of representative physical quantities measured during one interrogation is given in table VI-1. Raw data are shown as received from the data processing system without any additional corrections having been applied. It can be observed that only 40 frames, representing approximately 12 seconds of the 1-minute interrogation, were necessary to determine the performance of the test groups during this particular orbit. However, as the tumble rate decreased, the time interval between maximum voltage peaks increased. Therefore, after the satellite had been in orbit for several months, it was necessary to make longer printouts of the data in order to determine the maximum voltage output during one tumble revolution. Also, with the printout of two or more maximum voltage peaks, it was possible to average the maximum voltage measurements and thus insure a more accurate determination.

Several factors influenced the magnitude of output voltages from the solar aspect sensor and the four solar-cell test groups, the most influential being the solar angle of incidence at the time of interrogation. Other factors that affected the output voltages were the variation in solar flux during the year, solar-cell temperatures, and earth-reflected solar radiation.

Angle of Incidence

At injection, the satellite was spin stabilized at a rotational speed of approximately 2.4 rps as determined from signal-strength records. If a completely stabilized mode is assumed, the solar angle of incidence at injection, with respect to the test solar cells, would be equal to η_S (which is defined as the angle between the satellite momentum vector and the direction of the sun). Within a few days after injection, the longitudinal axis of the spacecraft would normally begin to cone as the spin rate decreased. The cone angle would normally enlarge with time and the satellite would normally develop into a full tumble mode several months later. For the day of launch, η_S was calculated to be 25.87°, and the calculated variation of η_S during the 1-year life of the mission is shown in figure VI-6.

During each cycle of coning or tumbling, the minimum solar angle of incidence ϕ, with respect to the test solar cells, was determined from the data received from the solar aspect sensor at the time of each interrogation of interest. These minimum angles of incidence were then applied to the maximum voltages received from the four test groups during the corresponding cycle of coning or tumbling. This procedure resulted in output voltages comparable to voltages from normal-incidence illumination.

TABLE VI-1.- TYPICAL PRINTOUT OF DATA FROM EXPLORER XXIII SOLAR-CELL IRRADIATION EXPERIMENT

[Pass 3080, 1965 GMT 157:14:41:15]

Telemeter A								Telemeter B			
Frame	Time, sec	Channel[a]						Frame	Time, sec	Channel[b]	
		D-15, °C	F-8, volts	F-9, volts	F-10, volts	F-11, volts	D-16, °C			F-11, volts	D-16, °C
1	0.177	10	0.14	0.21	0.21	0.20	11	1	0.193	0.18	11
2	.500	10	.23	.20	.20	.20	11	2	.524	.25	12
3	.823	11	.23	.22	.21	.21	12	3	.855	.25	11
4	1.145	10	.23	.21	.20	.21	12	4	1.185	.18	10
5	1.468	9	.15	.21	.20	.18	12	5	1.516	.18	10
6	1.791	10	.18	.20	.20	.20	12	6	1.846	.23	12
7	2.114	10	.15	.20	.19	.21	11	7	2.177	.17	11
8	2.436	10	.17	.18	.19	.18	12	8	2.508	.23	12
9	2.759	10	.18	.18	.27	.32	11	9	2.838	.22	11
10	3.082	10	.22	.25	.45	.50	11	10	3.169	.20	13
11	3.404	10	.27	.42	.59	.64	12	11	3.500	.37	11
12	3.727	10	.37	.63	.73	.75	12	12	3.831	.67	11
13	4.050	10	.49	.82	.89	.87	12	13	4.162	.87	11
14	4.373	10	.54	1.00	1.04	1.00	11	14	4.493	1.01	12
15	4.696	10	.60	1.13	1.15	1.11	12	15	4.824	1.11	12
16	5.019	10	.72	1.25	1.27	1.19	11	16	5.155	1.16	10
17	5.341	10	.80	1.36	1.38	1.30	11	17	5.485	1.24	12
18	5.664	9	.86	1.43	1.46	1.35	11	18	5.816	1.40	12
19	5.987	10	.95	1.50	1.54	1.43	11	19	6.147	1.42	12
20	6.309	10	1.03	1.55	1.59	1.49	11	20	6.478	1.48	12
21	6.632	10	1.09	1.59	1.64	1.53	11	21	6.809	1.52	10
22	6.955	10	1.11	1.64	1.67	1.55	11	22	7.140	1.56	11
23	7.277	11	1.20	1.67	1.69	1.58	11	23	7.470	1.62	11
24	7.600	10	1.18	1.68	1.70	1.59	12	24	7.801	1.58	11
25	7.923	9	1.22	1.68	1.71	1.57	11	25	8.132	1.56	13
26	8.245	10	1.18	1.68	1.69	1.57	12	26	8.462	1.60	12
27	8.568	10	1.17	1.65	1.65	1.54	11	27	8.793	1.54	12
28	8.890	10	1.11	1.61	1.61	1.50	12	28	9.124	1.48	12
29	9.213	10	1.05	1.56	1.56	1.43	12	29	9.455	1.48	12
30	9.536	10	.99	1.50	1.47	1.39	12	30	9.785	1.37	11
31	9.858	10	.90	1.41	1.40	1.30	12	31	10.116	1.32	12
32	10.181	10	.84	1.31	1.31	1.22	11	32	10.447	1.21	11
33	10.503	10	.74	1.25	1.18	1.11	12	33	10.777	1.22	11
34	10.826	10	.64	1.13	1.04	1.02	12	34	11.108	1.06	12
35	11.148	9	.52	.99	.87	.90	11	35	11.439	.95	12
36	11.471	10	.46	.85	.70	.76	12	36	11.770	.84	11
37	11.794	10	.35	.69	.49	.64	12	---	------	----	---
38	12.117	9	.27	.51	.31	.48	12	38	12.432	.48	11
39	12.439	10	.18	.32	.14	.32	12	39	12.762	.32	11
40	12.762	9	.16	.21	.06	.18	12	40	13.093	.20	12

[a]Channel notation:

D-15 Temperature, aspect sensor.
D-16 Temperature, groups 1 and 2.
F-8 Output, aspect sensor.
F-9 Output, group 1 shielded cells.
F-10 Output, group 2 shielded cells.
F-11 Output, group 3 unshielded cells.

[b]Channel notation:

D-16 Temperature, groups 3 and 4.
F-11 Output, group 4 unshielded cells.

Solar Flux

The percent of deviation of the solar flux from a mean value of 140 mW/cm^2 for a 1-year period after launch is shown in figure VI-7, obtained from reference VI-1. The maximum deviation is ±3.4 percent, with maximum-minimum intensities occurring at 6-month intervals.

Temperature

Temperature variations affect the output of silicon solar cells, the direction and degree of this effect being dependent upon the electrical parameters being measured and the method and degree of loading employed. Short-circuit current increases nonlinearly with increasing temperature, whereas maximum power and open-circuit voltage decrease approximately linearly with increasing temperature. Preflight calibrations made on the solar aspect sensor revealed that, over the temperature range from 0^o C to 60^o C, the variation in voltage output was less than 2 percent of its output at 30^o C. Preflight temperature calibrations made on the solar-cell test groups and from reference VI-2 indicate that the solar cells, as loaded in this experiment and over this temperature range, would experience voltage output variations of less than 3 percent of the voltage at 30^o C.

In addition to the temperature-dependent factors considered in the design of the spacecraft and the thermal controls employed, the flight temperatures of the solar aspect sensor and the four solar-cell test groups were also dependent upon two other principal factors, namely, the ratio of sunlight to darkness for each orbit and the time interval between the emergence of the satellite from the earth penumbra and the interrogation. The temperatures experienced by these test groups during the 1-year period in orbit ranged from a maximum of 40^o C to a minimum of -5^o C. The relatively small errors in voltage outputs induced by the variation in temperature were considered to be insignificant. Therefore, no temperature corrections have been applied to the data presented.

Earth-Reflected Solar Radiation

The earth-reflected solar radiation incident upon a satellite having orbital parameters similar to those of the Explorer XXIII can be as much as 30 percent of direct solar radiation (p. 232 of ref. VI-3), depending upon the reflected angle of incidence and the cloud and surface cover of the earth. No attempt was made to evaluate the earth-reflected radiation during this mission. However, in order to minimize the effect of reflected radiation on the results of this experiment, only data were used from those interrogations made while the nose of the satellite was oriented away from the earth, that is, near noon local satellite time and when ϕ was less than 40^o.

Flight Results

Figures VI-8 to VI-13 present the voltage outputs of the solar aspect sensor and the four solar-cell test groups for a 12-second interval of data received from several interrogations during the year. These curves represent plots from tabulated raw data, an example of which was shown in table VI-1. The initial frame rate of the telemetry systems, that is, the time required to scan sequentially all channels, was approximately 3.9 frames per second for system A and approximately 3.65 frames per second for system B. These rates decreased with time, and at the end of 1 year in orbit, the frame rate was approximately 2.9 frames per second for system A, and approximately 2.8 frames per second for system B. As mentioned previously, the aspect sensor and test groups 1, 2, and 3 were assigned to adjacent channels in system A. Therefore, any error induced in the data by the time interval necessary to scan the various channels was considered negligible. Although the two telemeters were commanded to operate simultaneously, the identically numbered channels in the two systems were not syncronized. Consequently, the voltage channel in system B was not syncronized with the aspect-sensor channel in system A. However, this source of error was avoided by utilizing only the minimum solar angle of incidence ϕ and the maximum voltages from the test groups during the cycle of coning or tumbling of interest.

Considerable scatter is observed in the data from pass 76, shown in figure VI-8. This is characteristic of most data received during the first few days after launch. Later, as shown for pass 336 (fig. VI-9) data scatter is reduced; more data points per spin cycle resulted in clearly defined cyclic curves and permitted a more accurate determination of maximum voltages.

From figures VI-8 to VI-13, several interesting observations can be made. As the satellite rotated in a spinning mode, and later, in tumble, the voltage outputs of the test groups passed through minimum and maximum values. These minima-maxima voltages were dependent upon η_S and the angle of cone at the time of interrogation. If η_S is known for a particular orbit, these minima-maxima voltages may be used to determine the cone angle for that orbit. Also, the time interval between adjacent maximum voltage peaks during an interrogation may be used to determine the spin or tumble rate for that particular orbit.

The minimum output voltages per revolution decreased as the cone angle increased and reached their lowest values at about day 346 GMT, 35 days after launch. After this date, the cone angle was of sufficient magnitude that the solar cells were not in direct sunlight continuously during a complete revolution. As shown in figures VI-10 and VI-11, the minimum voltages are relatively constant for an interval during each revolution. If direct solar radiation had been the only source of illumination, the outputs of the solar cells would have been zero during these minimum voltage periods. However, solar cells

are responsive to earth-reflected solar radiation, and their outputs during these minimum voltage periods were as much as 0.4 volt during some orbits. This value represents 20 percent or more of the solar-cell outputs from direct solar radiation at normal incidence.

After the satellite had developed into a full tumble mode, and disregarding all other influencing factors, ϕ would normally be expected to become 0^{o} at approximately 6-month intervals because of the rotational movement of the earth with respect to the sun. However, as will be shown, ϕ became 0^{o}, and hence maximum voltage outputs occurred, at irregular intervals during the year.

Figure VI-14 shows the voltages of the aspect sensor and the test groups from most of the interrogations during the year that resulted in usable data. Although the two telemetry systems were commanded simultaneously, there were some interrogations when only one system responded, with the result that data were received from only one system. These curves were plotted from data as received from the data processing system, without any corrections applied for angle of incidence and variation in solar flux. Each data point represents the maximum voltages obtained from the cyclic curves illustrated in figures VI-8 to VI-13. In fairing the curves through the data points, emphasis was given to those points least affected by earth-reflected sunlight. The blank periods in figure VI-14 are the result of a lack of usable data because of darkness interrogations, large solar aspect angles, and erratic telemetry data.

As shown in figure VI-14(a), the output voltages of all cells initially increased and reached maximum values corresponding to those expected for zero angle of incidence on day 334 GMT or 23 days after launch. On this date, a study of the cyclic curves indicated that both η_S and the half-angle of coning had become 26^{o} and, as a result, ϕ became 0^{o}. Insufficient information was available to define completely the spacecraft motions beyond this date. It will be noted that the output voltages of all cells peaked nine additional times during the year at irregular intervals. These 10 periods of maximum output were used to correct the aspect sensor for degradation.

Figure VI-15 shows the results obtained from the aspect sensor as determined from the maximum voltage output at each of the periods of zero angle of incidence, normalized to its initial voltage as determined from preflight calibrations and the first period of zero angle of incidence that occurred after launch. These data are corrected for solar-flux variation and plotted as a function of time in orbit.

In figure VI-16, the minimum solar aspect angle ϕ is shown for selected orbits as indicated by the aspect sensor. These angles were obtained from data received during interrogations that occurred near noon local satellite time, when the nose of the satellite was oriented away from earth and earth-reflected solar radiation was at a minimum during the period of maximum voltage output of the spin or tumble cycle.

Corrections were made for solar-flux variations and the apparent degradation observed in figure VI-15. The first data point shown is that from pass 6, on the day of launch. The angle ϕ is shown to be 22°. For the day of launch, η_s was calculated to be 25.87°. This means that approximately 11 hours after injection, the longitudinal axis of the satellite was coning at a total included angle of approximately 8°. This cone angle increased with time and ϕ decreased until ϕ became 0° for the first time about 23 days after launch.

The output voltages of the four solar-cell test groups are shown in figure VI-17. These data are from the same interrogations as the data shown for the aspect sensor in figure VI-16 and were corrected for solar-flux variation and solar angle of incidence as determined from the aspect sensor. Figure VI-18 shows these same voltages normalized to their respective initial values as determined from preflight calibrations and from flight data received at the time of the first period of zero incidence angle.

Discussion

It will be noted that the degradation of each group of cells shielded with 0.476-cm-thick synthetic fused silica was roughly 4 percent at the end of 1 year in space. Approximately the same degradation was observed for the aspect sensor cells that were shielded with 0.636 cm of the same type of synthetic fused silica. The corresponding degradation of each group of unprotected cells was approximately 16 percent. No degradation was observed until day 025 GMT. The rate of decay was relatively rapid for the next 70 to 80 days, then leveled off, after which another decay period was experienced. These periods of relatively rapid decay occurred when apogee was in the southern hemisphere and were probably caused by the heavier concentration of trapped electrons and protons at low altitudes over the South Atlantic Ocean. Similar irregularities in the degradation rates of solar cells on spacecraft in earth orbits were observed in results of experiments flown on Relay I and reported by Waddel in reference VI-4.

Table VI-2 presents the latitude position of apogee and the average electron flux rate for 4 nonconsecutive days during the year. These flux rates were determined by means of a computer program using space map electron distribution data for 1964.

TABLE VI-2.- ELECTRON FLUX RATE AT VARIOUS LATITUDES OF APOGEE

Date GMT	Latitude of apogee, deg	Integrated flux, electrons/cm^2-day
311 (1964)	-35	3.68×10^{10}
027 (1965)	-25	2.74×10^{10}
076 (1965)	0	2.21×10^{10}
208 (1965)	+35	5.63×10^{9}

With an initial perigee of 464 km and apogee of 980 km, the spacecraft passed through the lower fringe of the radiation belt only during a portion of each orbit. The average daily electron flux rate became more appreciable when apogee occurred at latitudes of the southern anomaly located above the Atlantic Ocean just off the coast of southern Brazil.

The number of electrons with energies above 0.5 MeV that impinged upon the unshielded cells was estimated to be about 7.6×10^{12} electrons/cm^2-year. Preflight electron irradiation tests made on the same type of unshielded cells at several energies from 0.5 MeV to 3.0 MeV indicated that 7.6×10^{12} electrons/cm^2 reduced their maximum power output by about 5 percent as measured under equivalent space sun illumination. These tests also indicated that approximately 5×10^{13} electrons/cm^2 were required to cause 16-percent degradation under similar illumination and loading conditions.

Apparently, a considerable percentage of the degradation experienced by the unshielded cells was caused by protons. From reference VI-5 it was estimated that the average proton flux rate for Explorer XXIII was approximately 1.4×10^8 protons/cm^2-day. The integrated proton flux for 1 year was estimated to be approximately 5.1×10^{10} protons/cm^2. Preflight proton irradiation tests on similar cells at 22 MeV, and published data on similar cells at 4.6 MeV (ref. VI-6) indicate that an integrated proton flux of 1×10^{11} and 5×10^{10} protons/cm^2, respectively, was required to cause 11-percent degradation of maximum power measured under equivalent space sun illumination. From these estimates, it appears that about one-third of the damage to the unshielded cells was caused by electrons and the remaining two-thirds resulted from protons.

The degradation experienced by the shielded cells was probably caused by both electrons and protons with energies sufficiently high to penetrate the shield. Based on range-energy relations for silicon dioxide, electrons with energies above 2.2 MeV, and protons with energies above 31 MeV should penetrate the 0.476-cm-thick shield. In the absence of a computer program giving proton energy distribution data for the orbit of Explorer XXIII, no attempt was made to estimate the protons that penetrated the shield. However, the degradation experienced by the shielded cells was relatively low, being about 4 percent. The limitation in data accuracy of the telemetry and data readout system prevents any detailed explanation concerning the degradation of the shielded cells. However, the amount of damage observed and the protection provided by the shield are substantiated by the performance of the primary power solar cells. Although the output of the power cells was not monitored, the power system voltages monitored during flight indicated no significant change at the end of 1 year in space. It is evident that the power solar cells, shielded in the same manner and degree as the shielded test groups, provided sufficient power for satisfactory operation of the electronic loads and to maintain the batteries at maximum capacity.

CONCLUSIONS

The solar aspect sensor and the four solar-cell test groups performed satisfactorily during the 1-year mission. The N/P, 1 ohm-cm, silicon solar cells covered with 0.476-cm-thick synthetic fused silica shields degraded approximately 4 percent while the unshielded N/P, 1 ohm-cm, silicon solar cells degraded approximately 16 percent during 1 year in orbit. The solar-cell degradation rate was not constant over this period. Damage plateaus were observed, with more rapid degradation occurring when apogee was in the southern hemisphere.

REFERENCES

VI-1. Moon, Parry: Proposed Standard Solar-Radiation Curves for Engineering Use. J. Franklin Institute, vol. 230, no. 5, Nov. 1940, pp. 583-617.

VI-2. Cunningham, Brian T.; Sharp, Robert L.; and Slifer, Luther W.: The Electrical Characteristics of Irradiated Silicon Solar Cells as a Function of Temperature. Proceedings of the Fourth Photovoltaic Specialist Conference. Volume I – Radiation Effects on Solar Cells and Photovoltaic Devices, PIC-SOL 209/5, Interagency Advan. Power Group, Aug. 1964, pp. A-7-1 – A-7-43.

VI-3. Cunningham, F. G.: Earth-Reflected Solar Radiation Incident Upon Spherical Satellites in General Elliptical Orbits. NASA TN D-1472, 1963.

VI-4. Waddel, Ramond C.: The Relay I Radiation Effects Experiment. NASA TN D-3665, 1966.

VI-5. Vette, James I.: Models of the Trapped Radiation Environment. Volume I: Inner Zone Protons and Electrons. NASA SP-3024, 1966.

VI-6. Cherry, William R.; and Slifer, Luther W.: Solar Cell Radiation Damage Studies With 1 MeV Electrons and 4.6 MeV Protons. NASA TN D-2098, 1964.

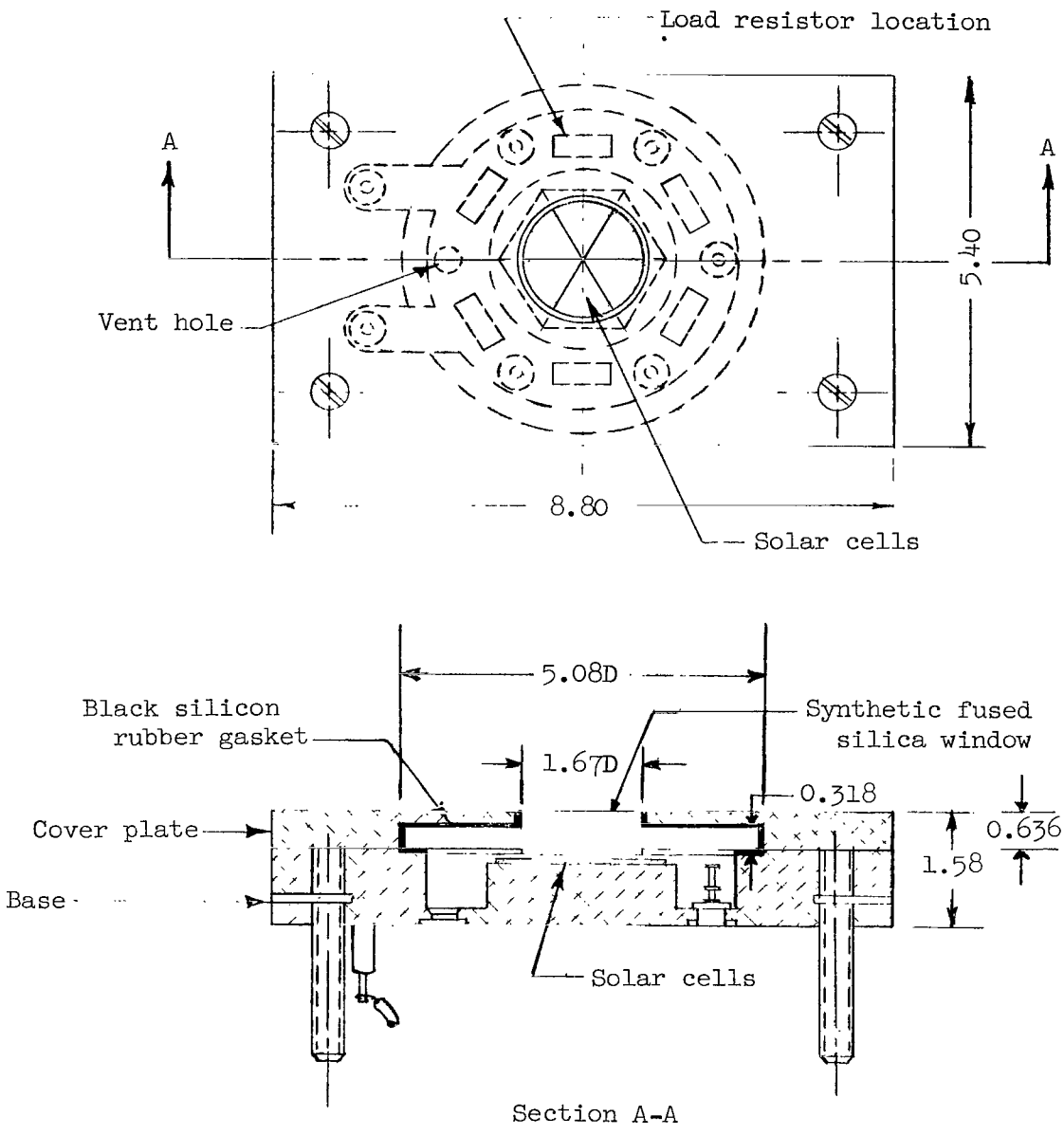

Figure VI-1.- Solar aspect sensor assembly. All dimensions are in centimeters.

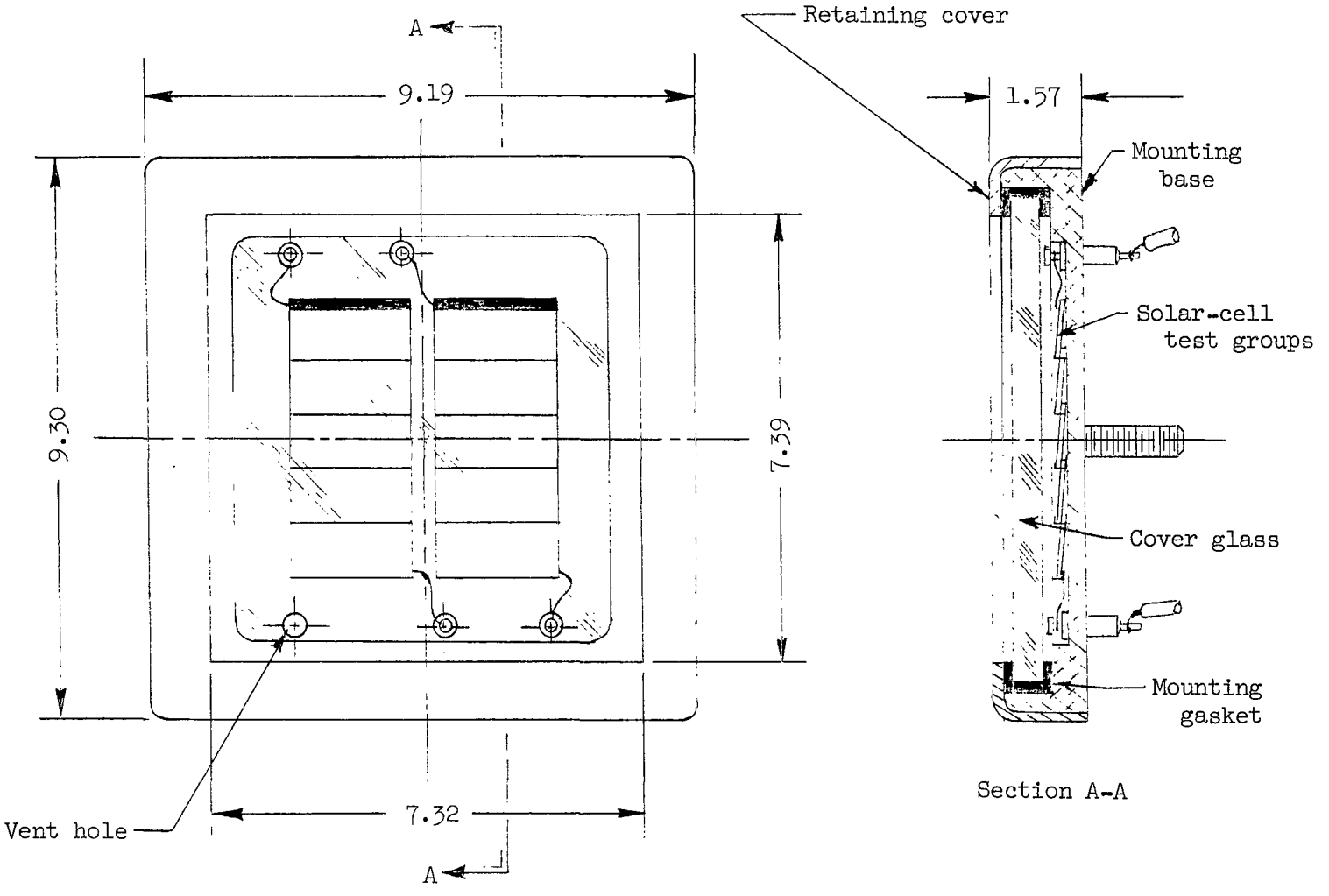

Figure VI-2.- Test solar-cell assembly. All dimensions are in centimeters.

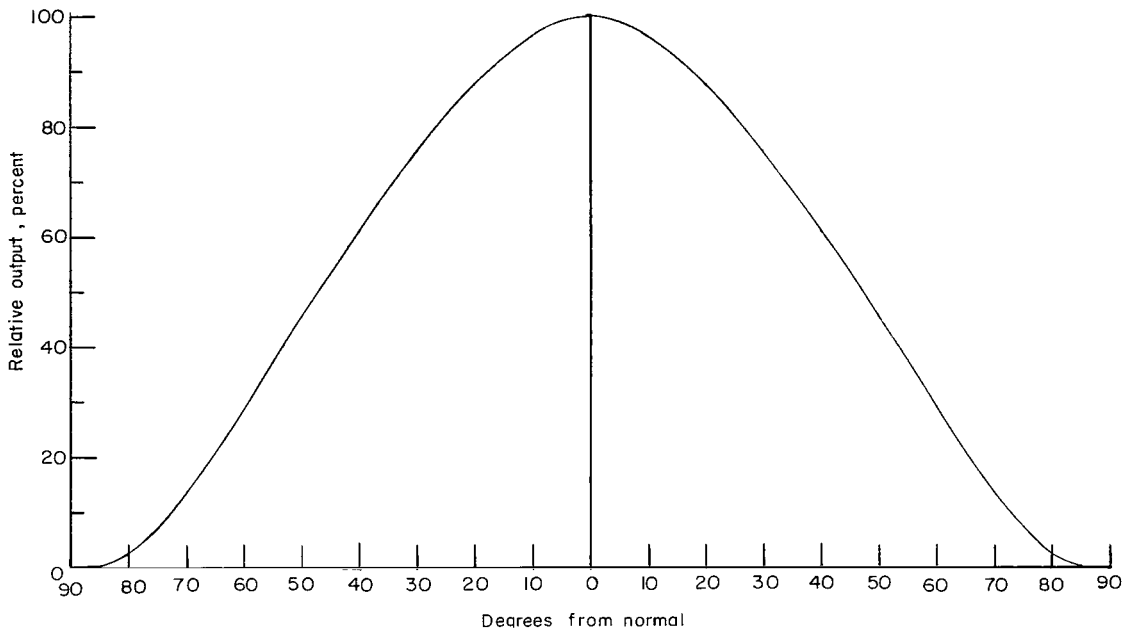

Figure VI-3.- Angular response of aspect sensor.

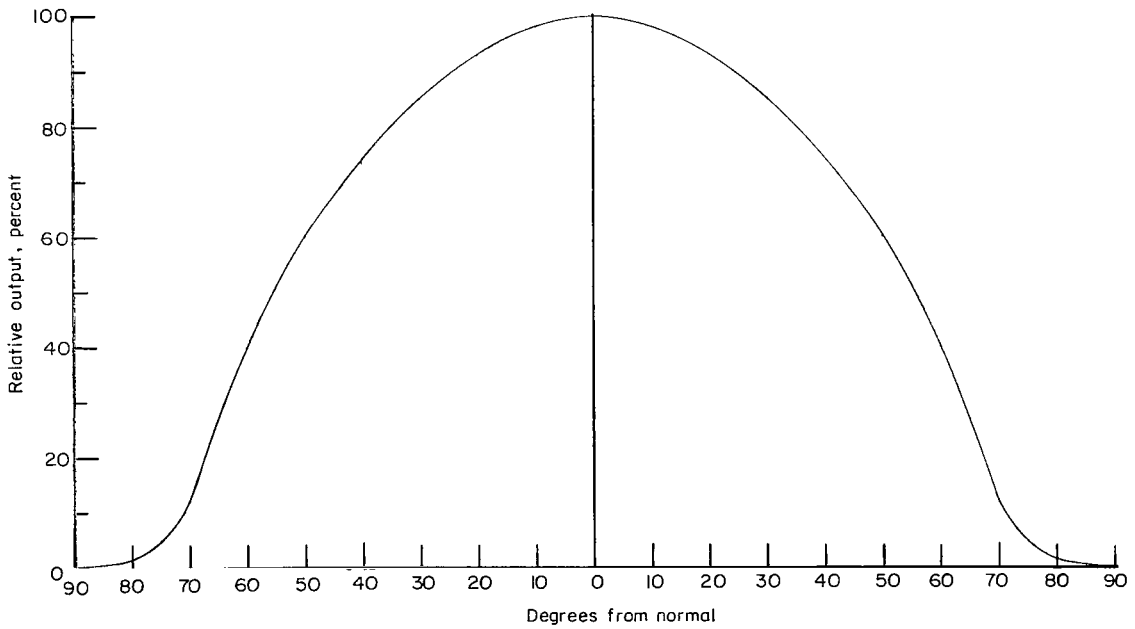

Figure VI-4.- Angular response of shielded solar-cell test groups 1 and 2.

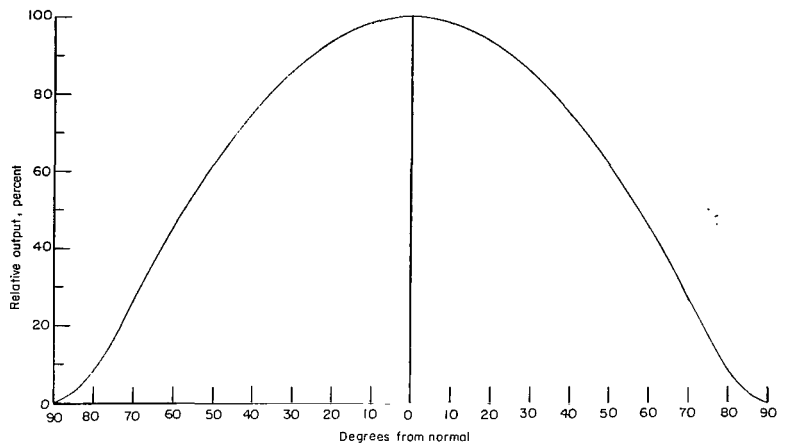

Figure VI-5.- Angular response of unshielded solar-cell test groups 3 and 4.

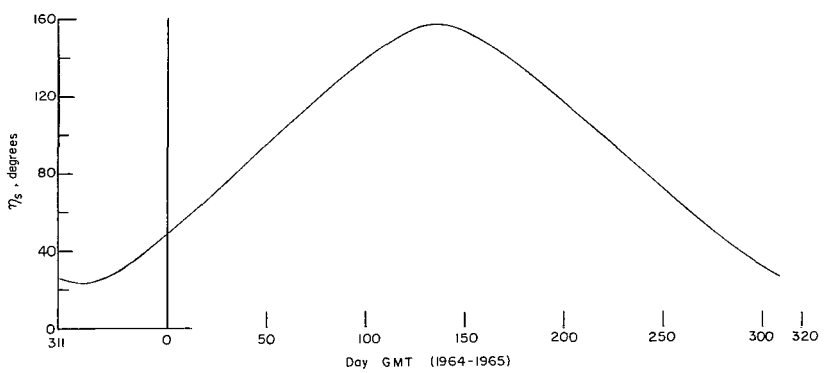

Figure VI-6.- Predicted orientation of Explorer XXIII momentum vector relative to the sun from day of launch, November 6, 1964.

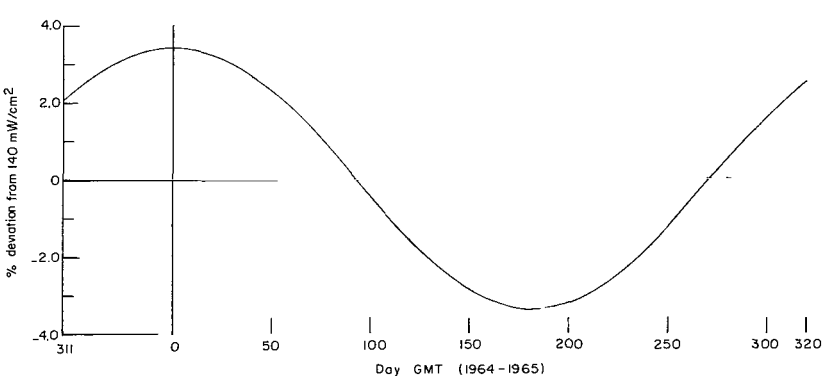

Figure VI-7.- Solar-flux variation.

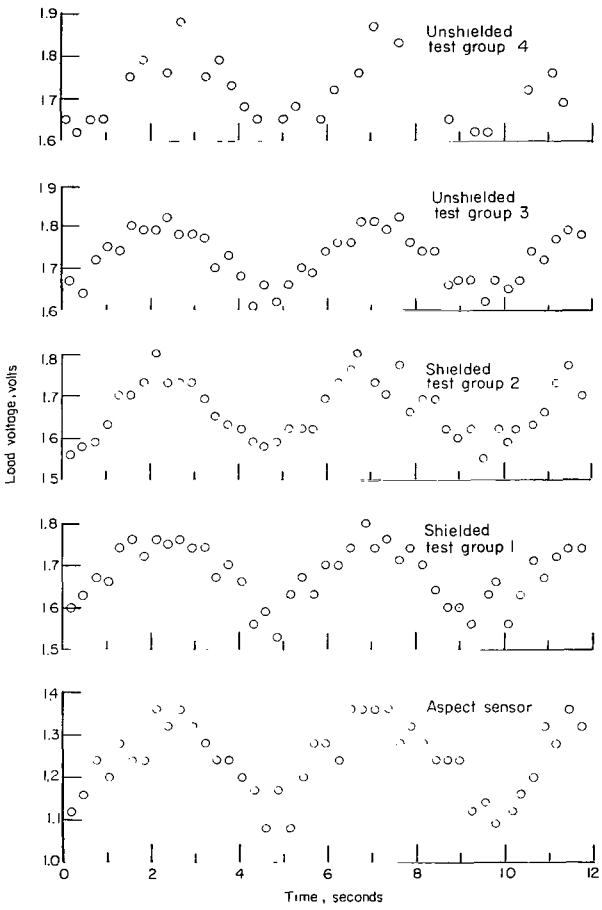

Figure VI-8.- Voltage output of test solar cells received at GMT 316:18:20:14, pass 76, from Santiago station.

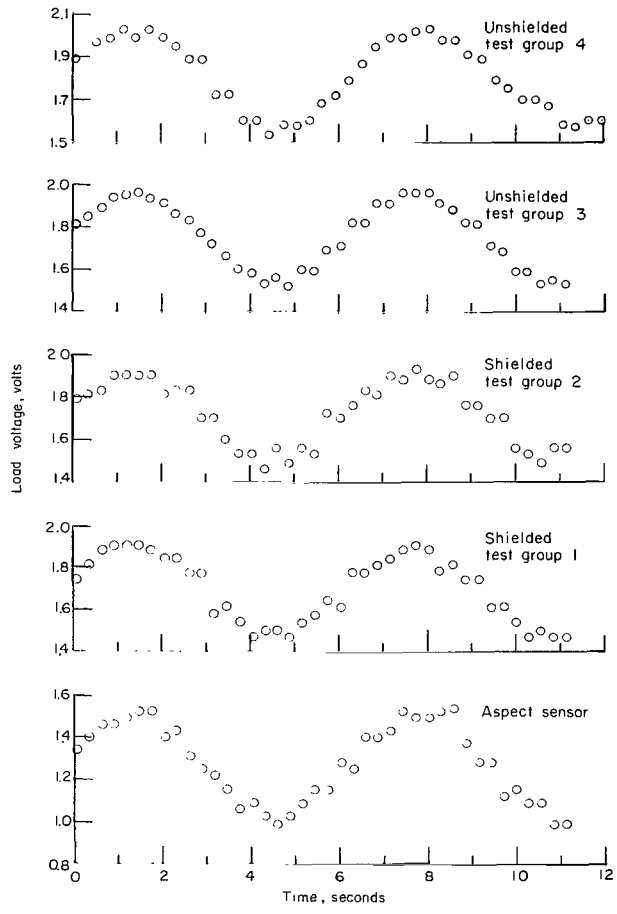

Figure VI-9.- Voltage output of test solar cells received at GMT 334:16:16:34, pass 336, from Santiago station.

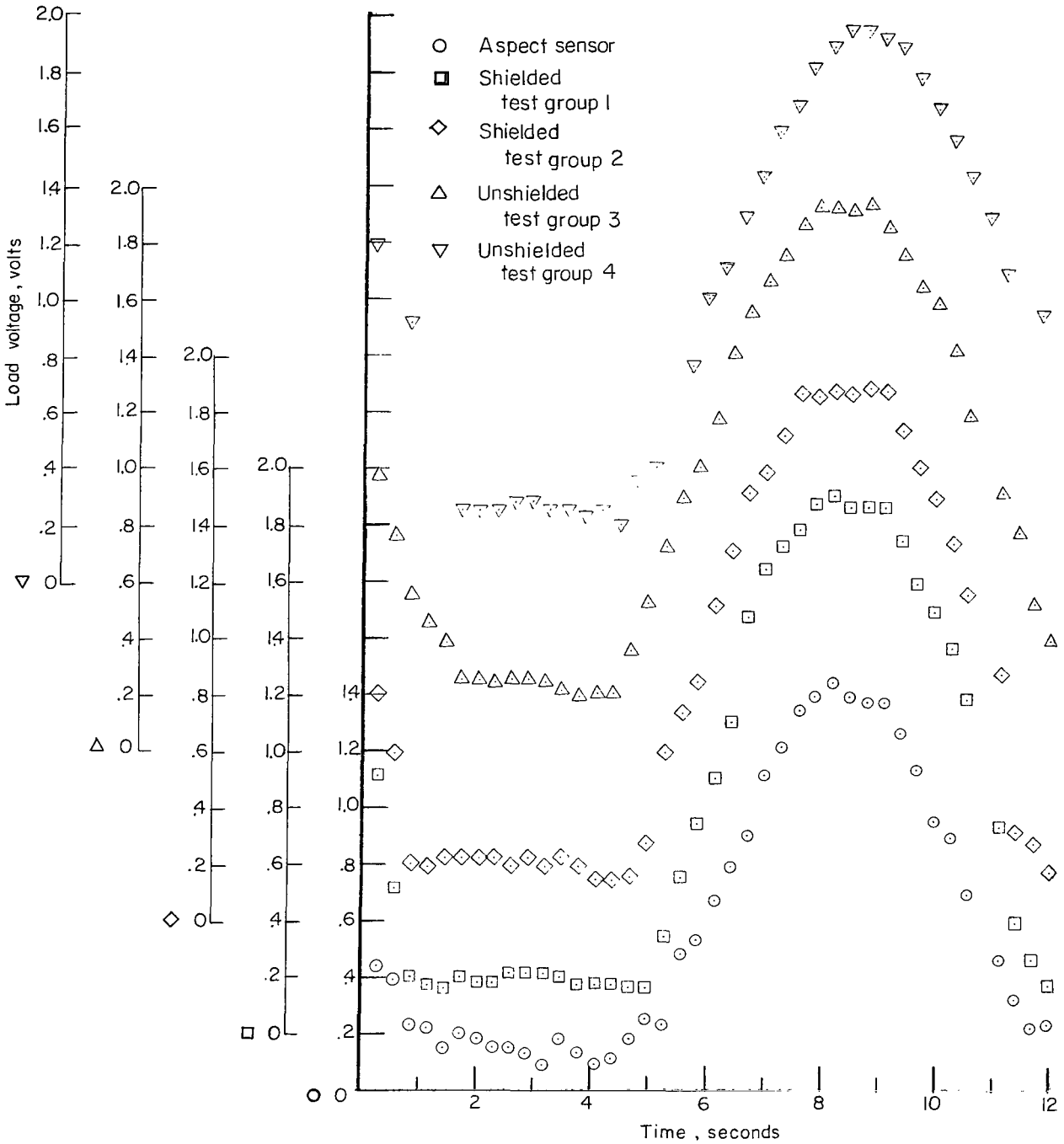

Figure VI-10.- Voltage output of test solar cells received at GMT 002:19:11:43, pass 832, from Mojave station.

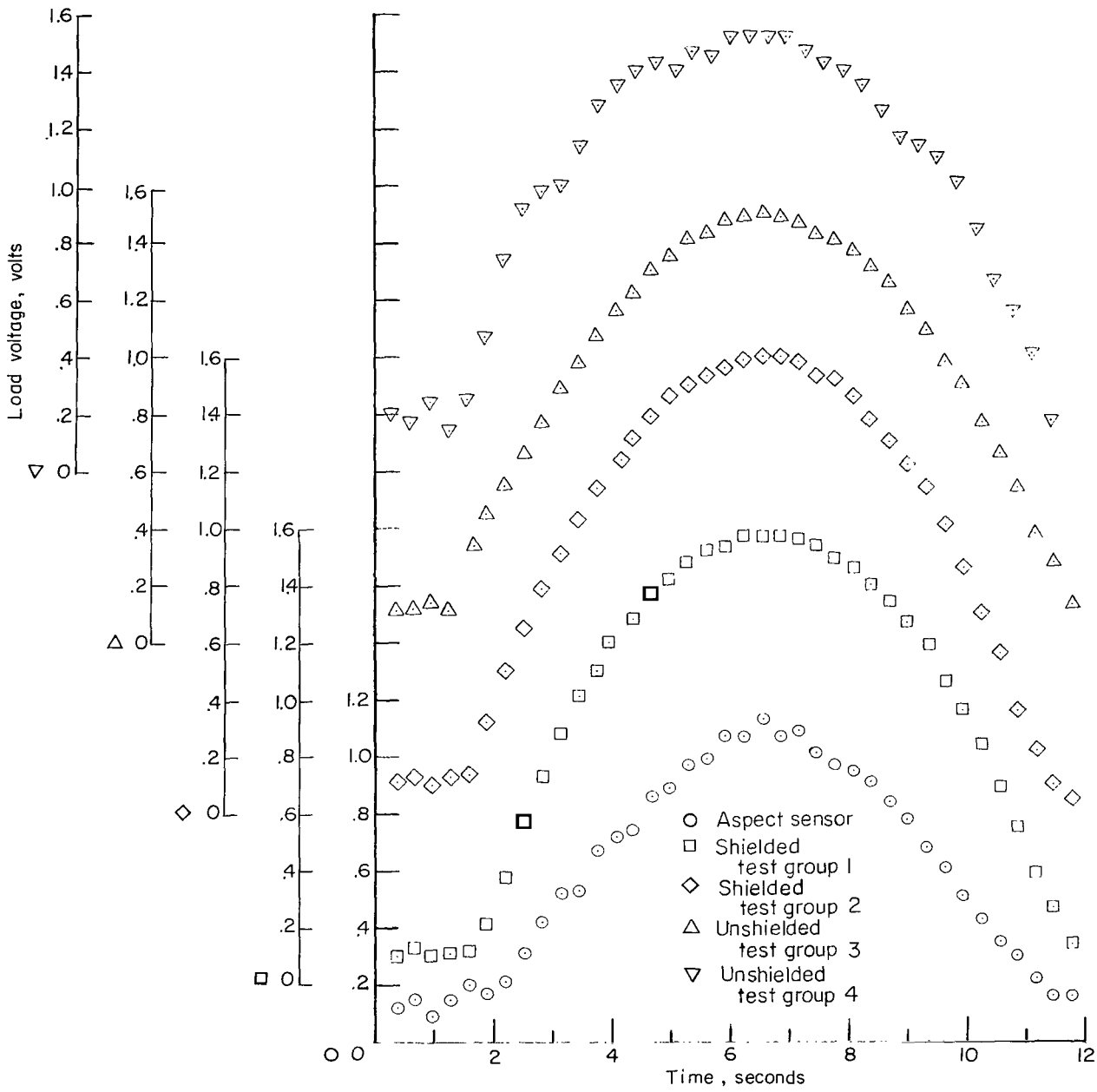

Figure VI-11.- Voltage output of test solar cells received at GMT 165:19:47:17, pass 3199, from Santiago station.

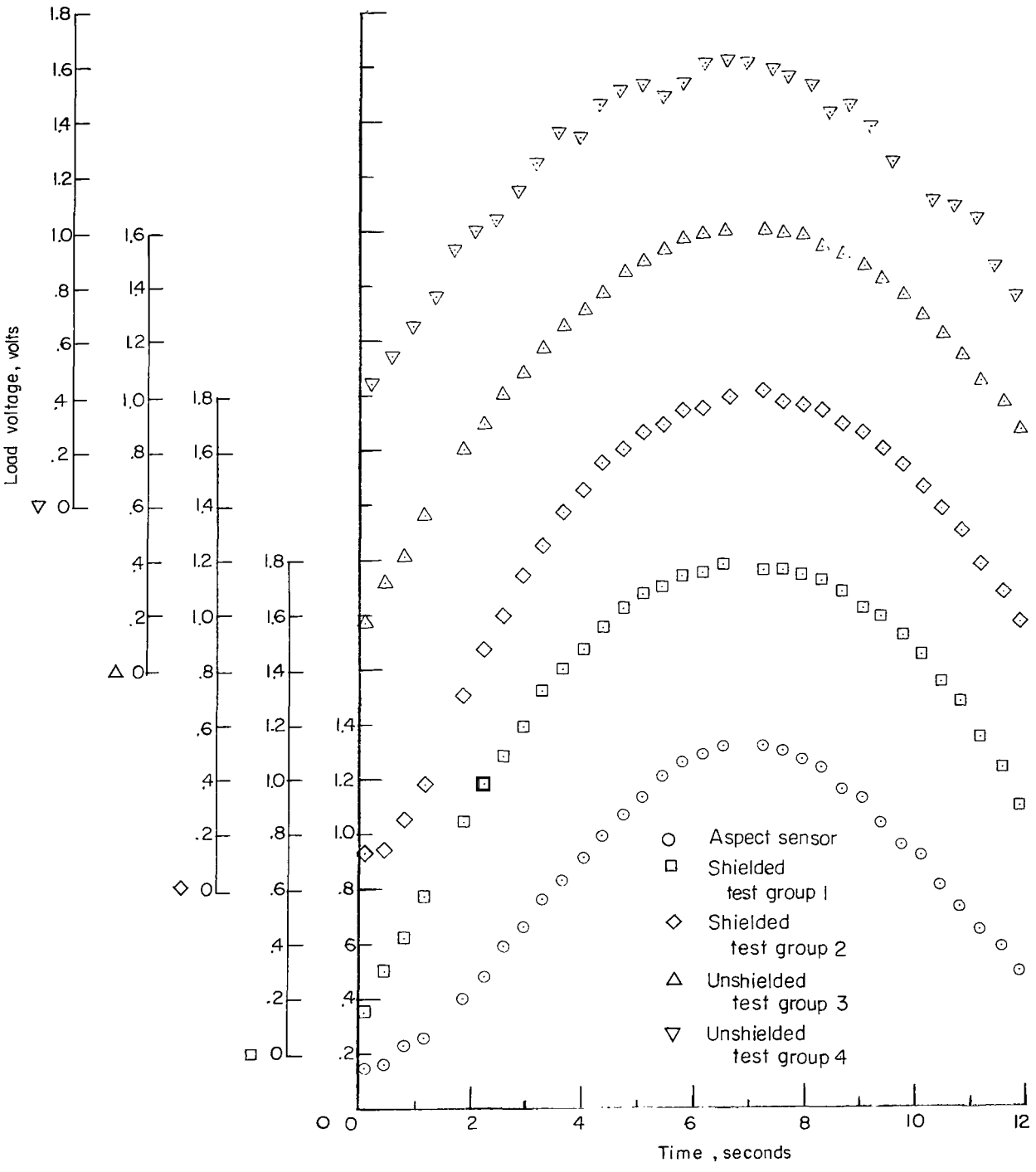

Figure VI-12.- Voltage output of test solar cells received at GMT 253:13:00:56, pass 4473, from Santiago station.

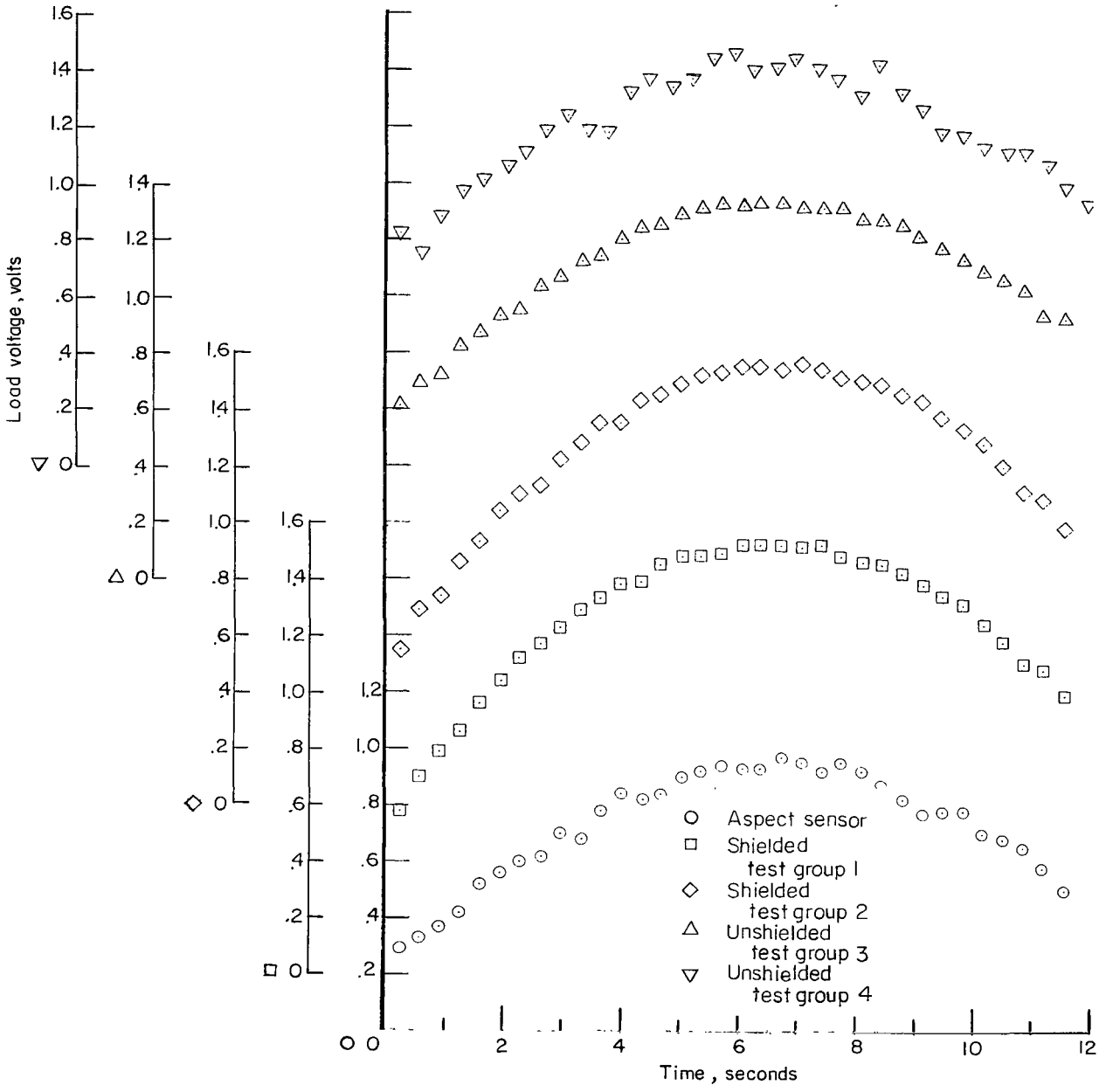

Figure VI-13.- Voltage output of test solar cells received at GMT 307:17:20:35, pass 5260, from Santiago station.

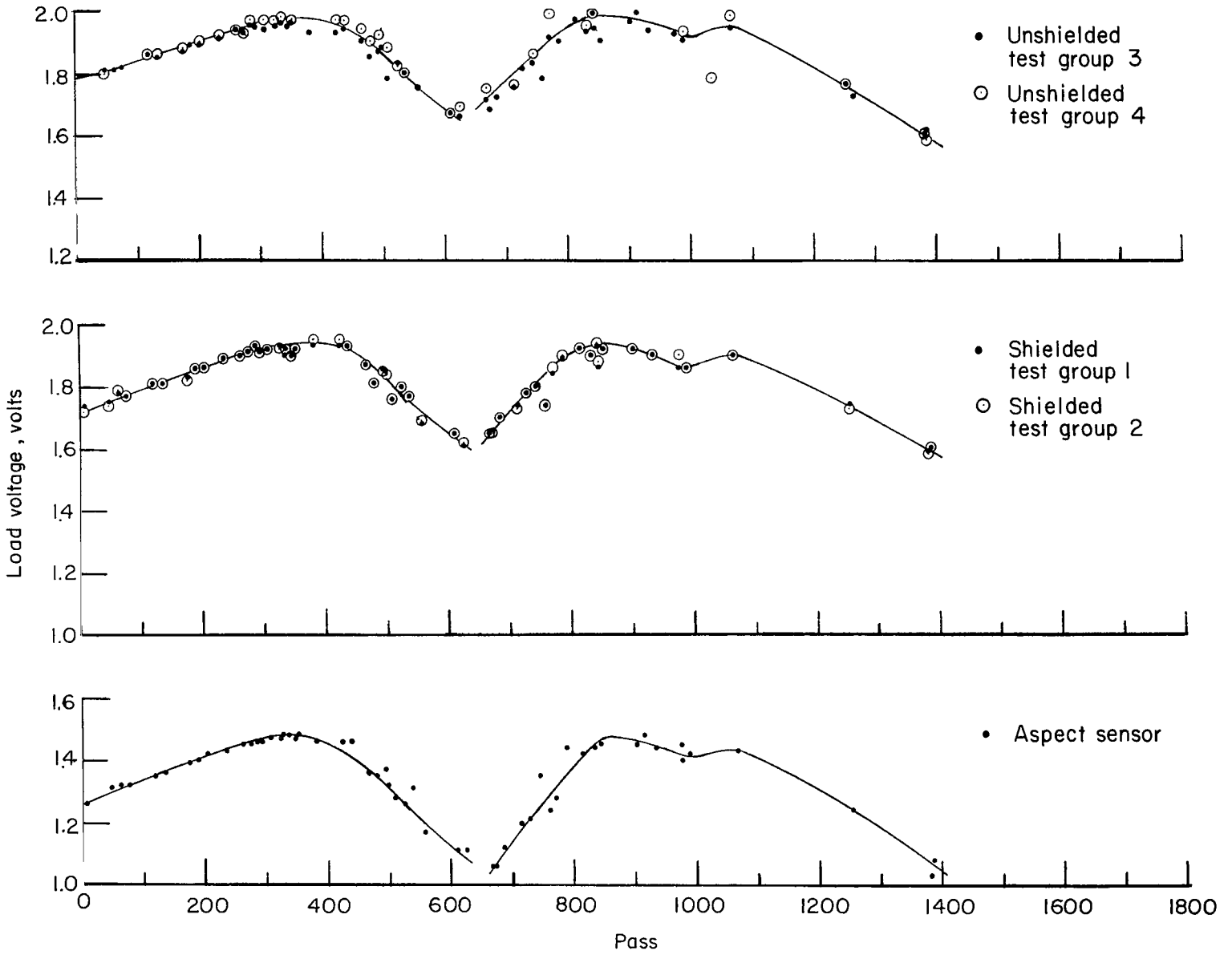

(a) Passes 0 to 1800.

Figure VI-14.- Uncorrected voltage output of test solar cells.

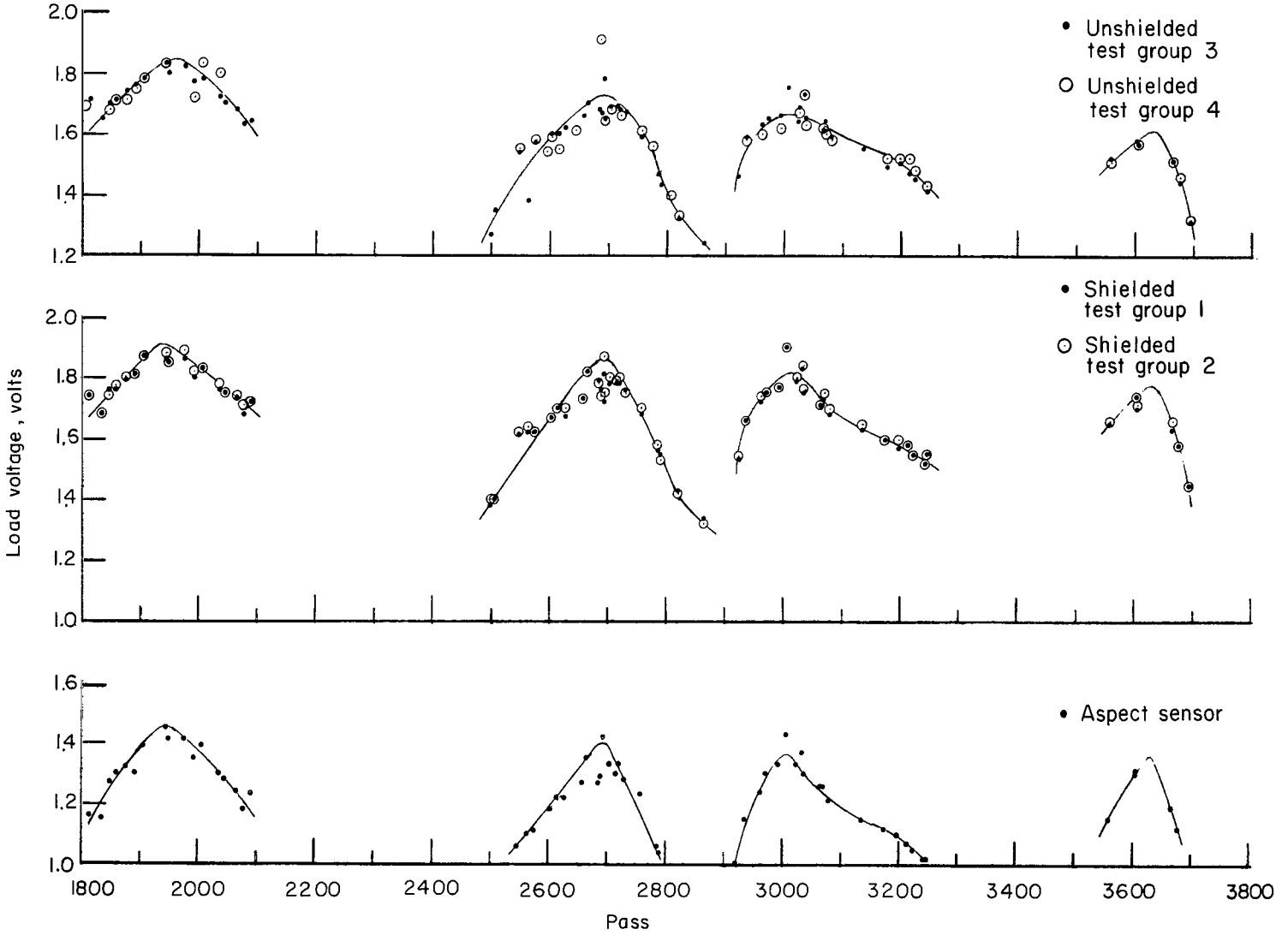

(b) Passes 1800 to 3800.

Figure VI-14.- Continued.

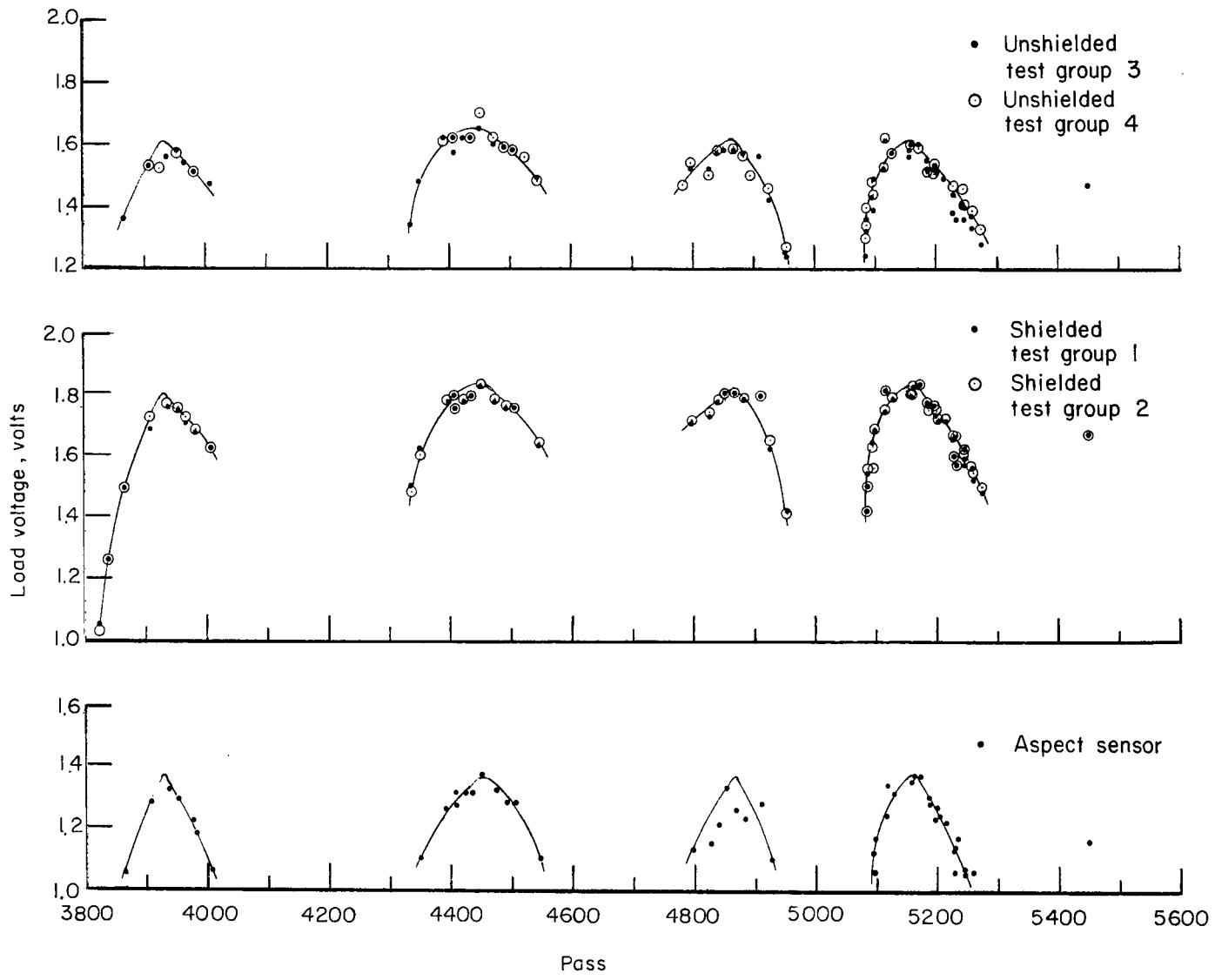

(c) Passes 3800 to 5600.

Figure VI-14.- Concluded.

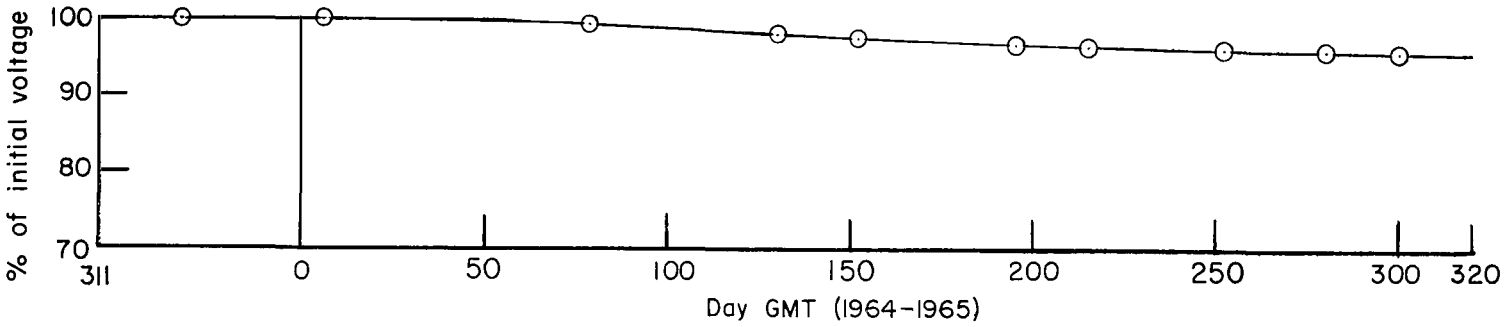

Figure VI-15.- Normalized voltage output of aspect sensor, corrected for solar-constant variation and angle of incidence.

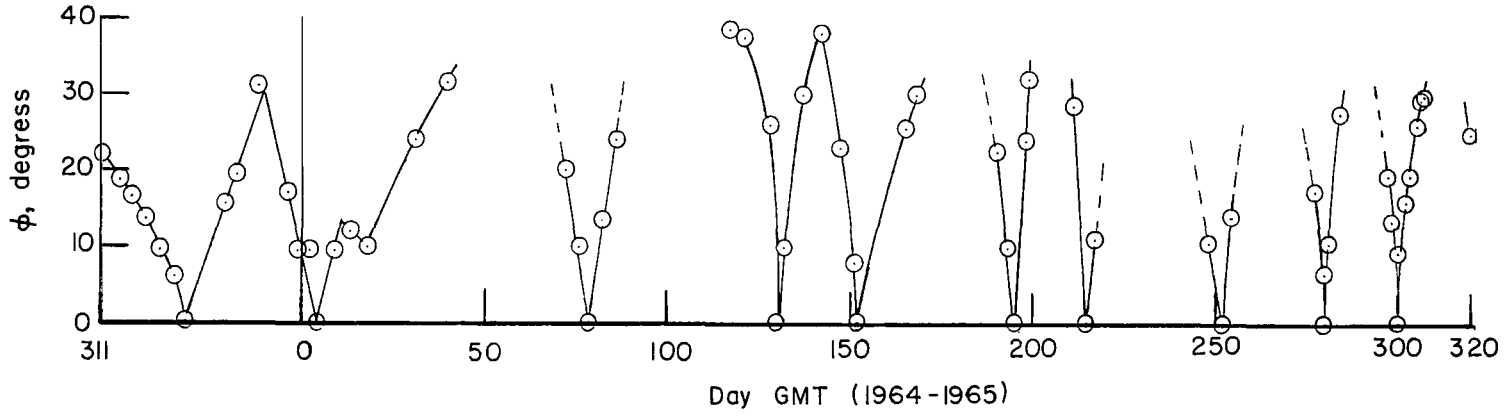

Figure VI-16.- Angle of solar incidence as indicated by aspect sensor.

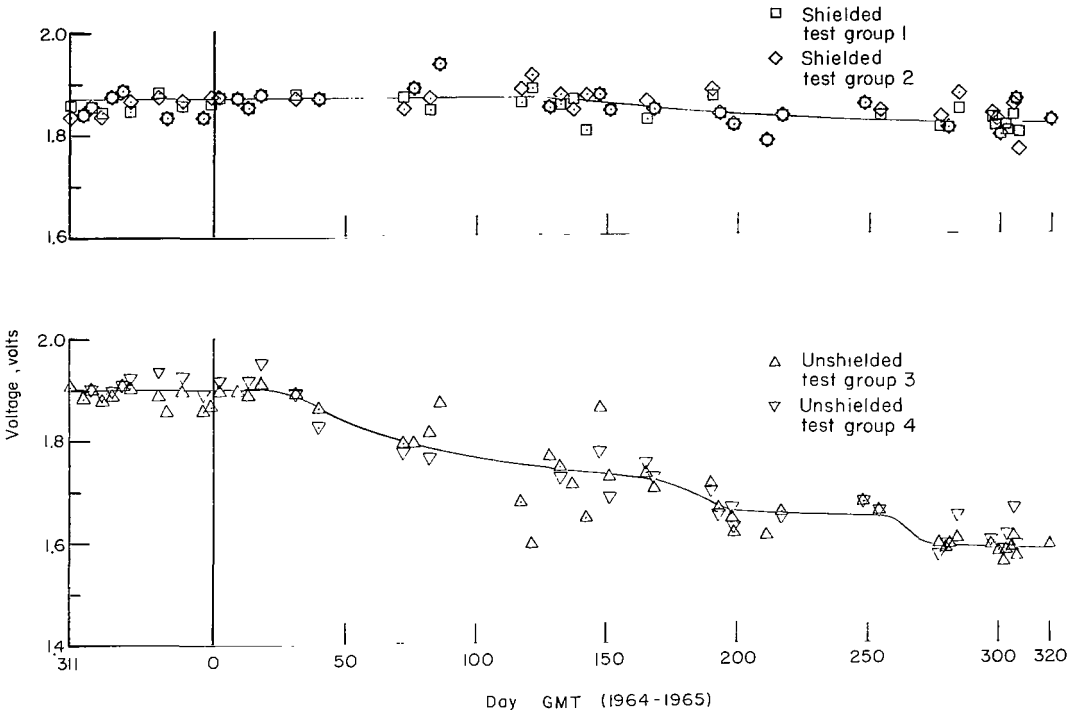

Figure VI-17.- Voltage output of test solar cells, corrected for solar-flux variation and angle of incidence.

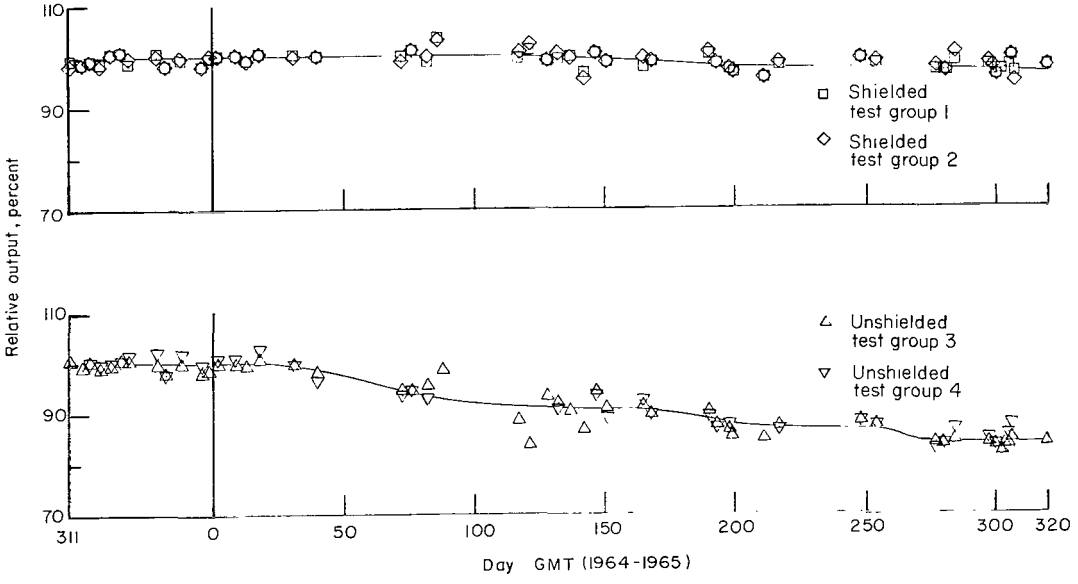

Figure VI-18.- Degradation of test solar cells during 1 year in orbit.

VII. PRELIMINARY METEOROID-PENETRATION MODEL

By Jose M. Alvarez
Langley Research Center

DEVELOPMENT OF MODEL

To date five satellites have measured directly the penetration flux of meteoroids in near-earth space. The two Explorer satellites (XVI and XXIII) exposed 25- and 50-micron beryllium copper and stainless steel and the three Pegasus satellites exposed 0.04-, 0.2-, and 0.4-mm aluminum. In chapter II the puncture rates measured by these satellites were compared with puncture rates predicted by Whipple. It can be concluded from this comparison that for the satellite thicknesses involved, these predictions do not adequately represent the measured meteoroid penetration flux.

The following analysis is used to define a meteoroid penetration flux curve from all the presently available penetration data. The flux model established is considered to be preliminary. Results of the sensor calibration program mentioned in chapter II and a better understanding of the zodiacal light and meteor data may provide a more confident definition of the meteoroid environment.

Disparities exist between the Explorer and Pegasus data since the experiments expose different materials and the construction and operation of the two types of penetration detectors are different. Data points representing the puncture rates as obtained from Explorer and Pegasus satellites are shown in figure VII-1. In plotting these data, material differences were not considered inasmuch as it was desired to obtain one conversion factor which takes into account both material and detector differences simultaneously. The two sets of data were correlated as follows.

Hypervelocity penetration theory and experiments obtain a relation to correlate the effective thickness of different materials of the form

$$t(a) = kt(b) \tag{1}$$

where k is a constant and $t(a)$ is the thickness of material a which is equivalent to $t(b)$, the thickness of material b, if identical types of detectors are used to measure penetration. Thicknesses are considered to be equivalent when they exhibit identical resistance to penetration.

The type of relation expressed in equation (1) was assumed to apply for different types of detectors having the same thickness and material construction; thus, the following equation may be used to correlate different types of detectors:

$$t(a,A) = k't(a,B) \tag{2}$$

where k' is a constant, $t(a,A)$ is the thickness of detector A made of material a, and $t(a,B)$ is the thickness of detector B made of material a. The use of this equation requires the assumption that the percent contribution of the dielectric material and foam to total penetration resistance is the same for any capacitor sensor data used in the analysis. From the foregoing definitions and equations, the relation

$$t(a,A) = k''t(b,B) \tag{3}$$

is obtained and correlates different detectors made of different materials. Figure VII-1 presents the satellite data as a function of $t(a,A)$ and $t(b,B)$ where (a,A) refers to Pegasus and (b,B) refers to Explorer.

The evaluation of k'' and the correlation of the Explorer and Pegasus data were performed as follows. It was assumed that the logarithm of flux was expandable in a power series as a function of the logarithm of thickness. For Explorer data,

$$\log \psi = \sum_{n=0}^{\infty} a_n \left(\log^n t(b,B)\right) \tag{4}$$

where ψ is the meteoroid penetration rate $\left(\frac{\text{Penetrations}}{\text{m}^2\text{-sec}}\right)$, t is the material thickness (microns), and a_n are constants. Two Explorer and two Pegasus data points were used to define the puncture rate as a function of material thickness. The Pegasus data for the thinnest material are not included in the present analysis since the aluminum alloy used for the detector was different from that used for the other two Pegasus detectors. Also, the dielectric and foam are thought to contribute significantly to the resistance of that sensor to penetration.

The constant k'' in equation (3) was defined by using the first three terms of the expansion given in equation (4). The logarithm of the flux was therefore assumed to be of the form

$$\log \psi = a_0 + a_1 \log t(b,B) + a_2 \log^2 t(b,B) \tag{5}$$

for a range of material thickness to be specified. The Explorer data were used directly in equation (5) but the Pegasus thickness data (ref. VII-1) were converted to equivalent Explorer thicknesses by means of equation (3). The solution of the four simultaneous nonlinear equations for a_0, a_1, a_2, and k'' defined a parabola which represents the two Explorer data points and the two converted Pegasus data points. The two Explorer points represent an average of the beryllium-copper and the stainless-steel data. The result of the parabolic fit is shown in figure VII-1 and, in terms of stainless steel, is given by the following equation for $t(b,B)$ in microns:

$$\log_{10} \psi = -5.9657 + 1.3638 \log_{10} t(b,B) - 0.6831 \log_{10}^2 t(b,B) \qquad (6)$$

for $9.9\mu \leqq t(b,B) \leqq 8.4 \times 10^3 \mu$. The lower thickness limit (9.9μ) is obtained as the peak of the parabola. The upper thickness limit was obtained by requiring the equation to be consistent with ground-based meteor data of the form

$$\log \psi = p + q \log t(b,B) \qquad (7)$$

where p and q are constants and q is assumed to be -4 (ref. VII-2). Equation (7) was differentiated with respect to $\log t(b,B)$ and the parabolic relation was assumed to hold to the point where

$$\frac{d}{d \log t(b,B)} \log \psi = -4 \qquad (8)$$

which gives a thickness of 8.4×10^3 microns.

The evaluation of k'' establishes the relation between Pegasus thickness $t(a,A)$ and Explorer thickness $t(b,B)$ and is given by

$$t(a,A) = 0.82t(b,B) \qquad (9)$$

One possible means to extrapolate the flux relation beyond a thickness of 8.4×10^3 microns would be to assume that the curve continues in the form of equation (7). Such an extrapolation would be represented by

$$\log \psi = 4.5636 - 4 \log t(b,B) \qquad \left(t(b,B) > 8.4 \times 10^3 \mu\right) \qquad (10)$$

Figure VII-2 presents the flux curve in terms of aluminum. This plot was obtained by assuming that stainless steel and beryllium copper are twice as hard to penetrate as aluminum. The Whipple 1963 penetration model is included for comparison.

REFERENCES

VII-1. Naumann, Robert J.: The Near-Earth Meteoroid Environment. NASA TN D-3717, 1966.

VII-2. Whipple, Fred L.: On Meteoroids and Penetration. J. Geophys. Res., vol. 68, no. 17, Sept. 1963, pp. 4929-4939.

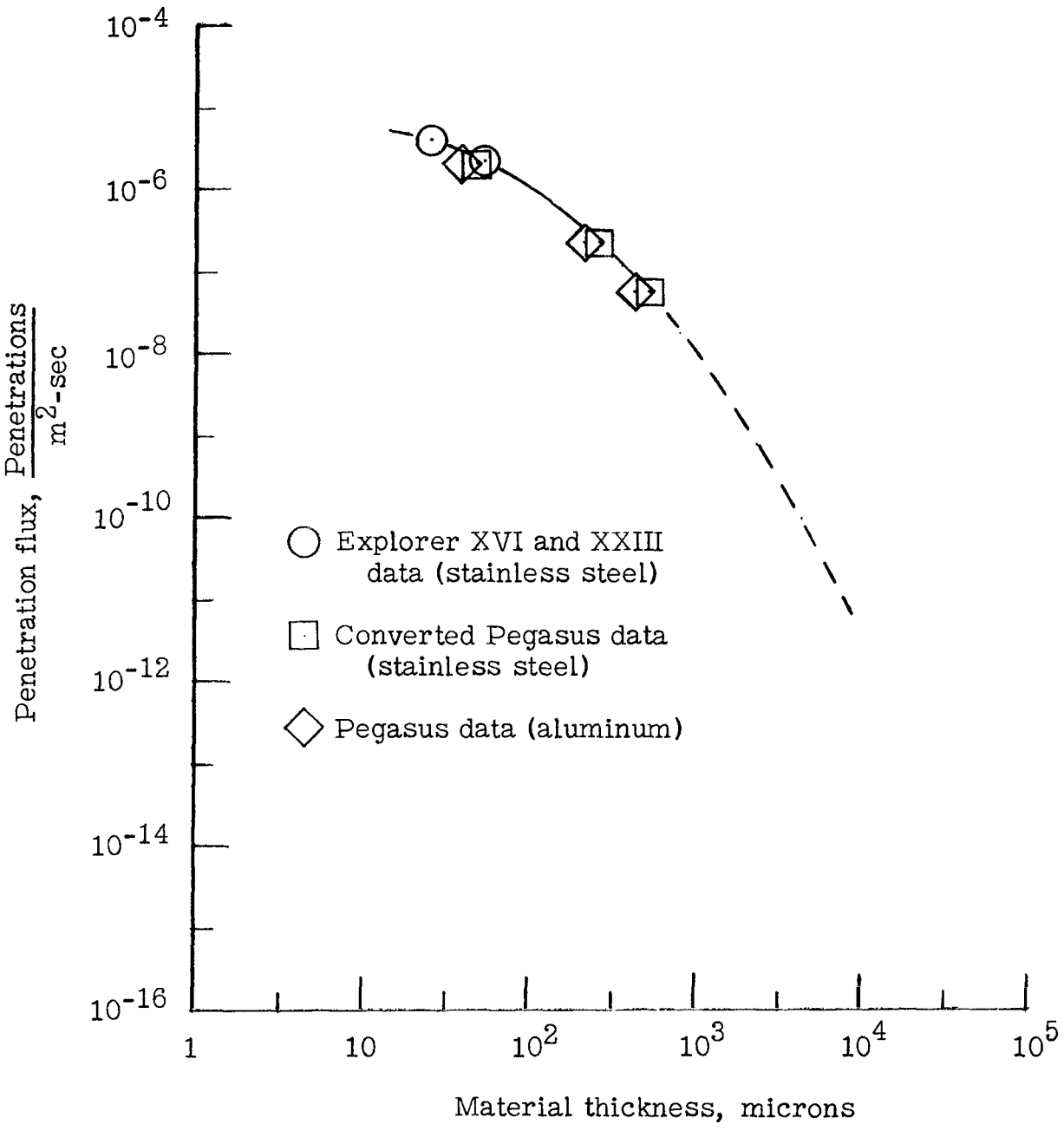

Figure VII-1.- Correlation of Explorer and Pegasus penetration data.

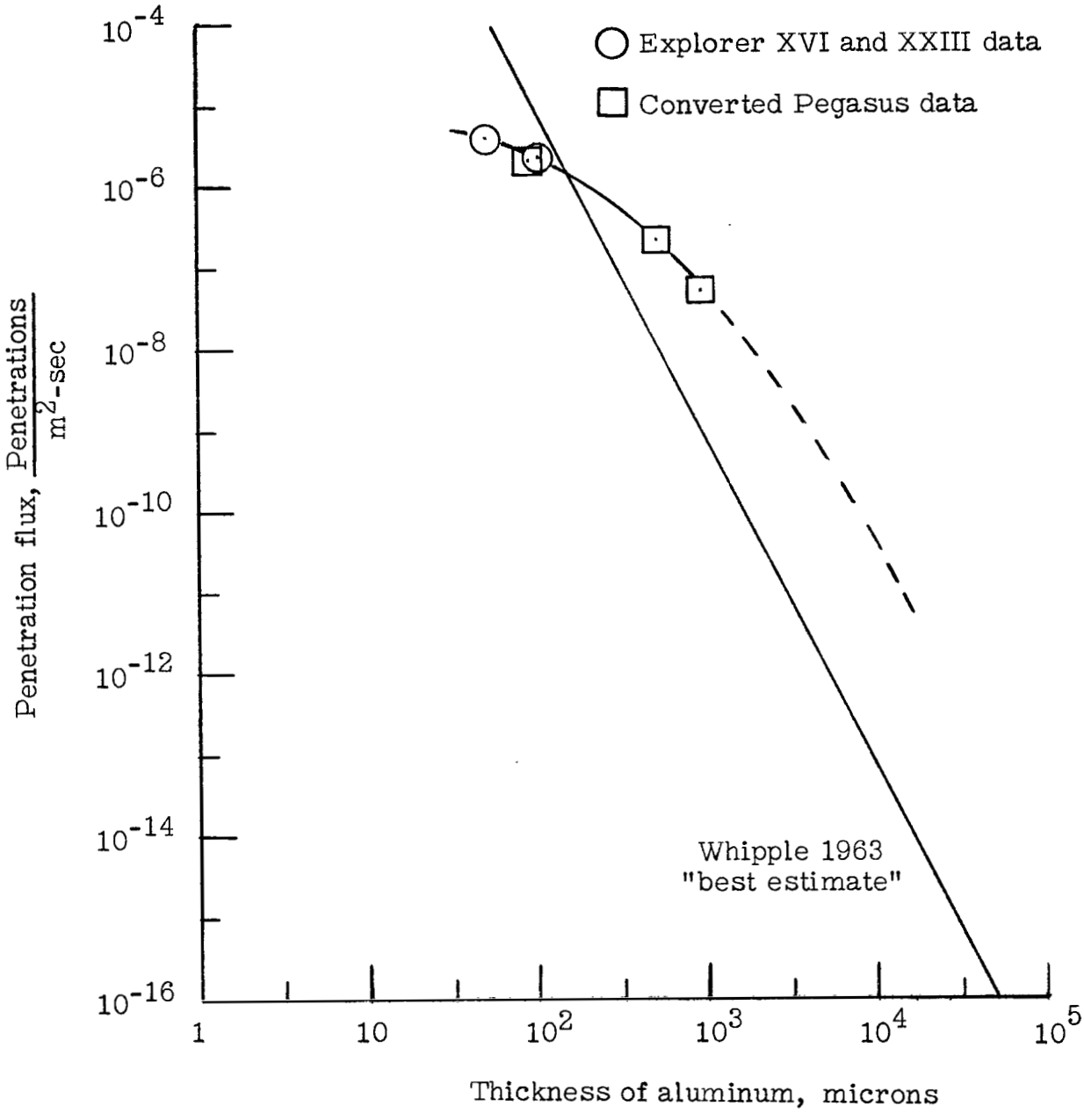

Figure VII-2.- Penetration flux in aluminum.

VIII. ORBITAL PARAMETERS AND SPACECRAFT MOTIONS

By Richard E. Turner
Langley Research Center

Explorer XXIII was launched on November 6, 1964, at 12:02:01 GMT (07:02:01 EST) on a Scout launch vehicle and was injected into orbit at 12:11:15 GMT. Nominal orbital parameters are shown in the following table along with actual orbital parameters measured on November 6, 1964:

Parameter	Nominal	Actual (Nov. 6, 1964)
Altitude at perigee, km . . .	458.30	463.39
Altitude at apogee, km . . .	999.67	980.30
Inclination, deg	51.99	51.95
Period, min	99.16	99.23

Earth oblateness caused the perigee to vary as much as 2.0 km and the apogee to vary as much as 3.0 km in the course of a year. At injection the spacecraft was spinning about the longitudinal axis which was inclined approximately 25° from the sun line.

Prior to fourth-stage ignition, the motor and payload were spun up about the longitudinal axis with four spin motors. Despin was not used. Signal-strength records taken at Antiqua, BWI, were used to estimate spin rates. The results are presented in the following table:

Time spin rate was measured	Time interval used to estimate spin rate, GMT, hr:min:sec	Spin rate, rpm
Between spin-up and fourth-stage ignition . . .	12:10:46.37 to 12:10:50.52	144 ± 1
After fourth-stage burnout	12:11:18.42 to 12:11:22.82	150 ± 1

The data in this table show an increase in spin rate during fourth-stage burning. Although this increase cannot be predicted accurately, it is expected as a result of momentum transfer between propellant and motor during the fourth-stage burning. The spin rate of 144 rpm after spin-up was much lower than the predicted value of 165 rpm. Inaccuracy in the determination of the moment of inertia used to predict the spin rate

could not account for this difference. Possible causes of the discrepancy are (a) one or more of the spin motors may not have performed as expected and (b) the spin-table bearing friction might have been higher than expected.

The solar aspect sensor indicated that approximately 11 hours after injection, the satellite longitudinal axis was coning about the angular momentum vector. The data from this sensor indicated the half-angle of coning was approximately 4^{o}. On the day 334 GMT or 23 days after launch a study of the aspect sensor data indicated the half-angle of coning had increased to approximately 26^{o}. Insufficient information was available to completely define the spacecraft motions beyond these data.

IX. THERMAL CONTROL SYSTEM

By Doyle P. Swofford
Langley Research Center

SYSTEM DESCRIPTION

The thermal control of the Explorer XXIII, like those in all previous S-55 series payloads, was entirely passive. Since the Explorer XXIII was built around the last-stage motor of the Scout (X-258-C1) and did not separate from that stage, it was necessary to provide protection for the spacecraft from the hot motor case just after burnout as well as to provide for maintenance of acceptable temperatures while in orbit.

A flight test of an X-258-C1 rocket motor, using the Javelin launch vehicle, had shown that motor-case temperatures as high as 440° C might be encountered shortly after burnout. In that test the rocket motor was radiating heat directly to space and the peak temperature was reached about 8 minutes after burnout. To reduce heat transfer from the hot motor case to the Explorer XXIII payload, a layer of aluminum foil was bonded to the motor case and a 20-layer blanket of aluminum foil was placed between the motor case and the payload. Motor-case temperatures were expected to reach about 540° C on the side wall and about 425° C on the dome. The insulation reduced heat dissipation from the rocket motor and caused higher motor-case temperatures than those for the noninsulated Javelin motor.

FLIGHT RESULTS

Figures IX-1 and IX-2 show calculated temperatures, after burnout, for the telemeter canisters and battery modules for a peak temperature of 425° C on the forward dome of the motor. The actual recorded temperatures are also shown in these figures and are about 10° C below the calculated values.

The pressurized-cell detectors are arranged in seven rows around the spacecraft. (See chapter II.) Two thermistors are mounted under the fourth row from the nose and one under the sixth row. Figures IX-3 and IX-4 show the calculated post-burnout temperature histories for the fourth and sixth rows of pressure cells for peak temperatures of 540° C and 650° C on the entire cylindrical section of the motor case. Except for a small section of the cylinder, the temperature on the motor case will remain much lower than these peaks. Because the peak temperatures were used in the calculations, the actual temperatures are lower. The highest recorded pressure-cell temperature for each row was between the two curves and closer to the higher one. The recorded

temperature dropped off more rapidly than predicted, but this dropoff is at least partly due to assuming in the calculations of the predicted temperatures that the motor case radiated heat only to the payload and thus neglecting loss of heat by radiation through the nozzle.

Figures IX-5 to IX-7 show temperatures recorded from November 6, 1964 through November 5, 1965 for the telemeter canisters, battery boxes, and pressurized-cell detectors. The two horizontal lines on each figure represent the highest and lowest temperatures expected during the mission, with the exception of the period during which the motor-case heat was being dissipated and the spacecraft was attaining equilibrium with the environment (1 or 2 days after launch).

The Explorer XXIII thermal control system was designed for the spacecraft in tumbling motion about a transverse axis of rotation with a small residual spin about the longitudinal axis. Because of internal torques produced by flexing of the antennas and spacecraft structure, the initial spinning motion about the longitudinal axis undergoes a transition to tumbling motion in a plane perpendicular to the spin axis. The time required for Explorer XXIII to undergo this transition was estimated to be of the order of a few weeks. The apparent coning angle of the spacecraft motion took approximately 3 weeks to reach 26°. (See chapter VIII.) Transition is evident from the pressure-cell temperature (fig. IX-7), which was low during the first 3 weeks but which, after the first period of 100 percent time in sunlight was entered at about 6 weeks, never dropped back to this initial level.

While the spacecraft is still spinning about its longitudinal axis, the area of the cylindrical array of pressure cells projected to the sun varies as the sine of the solar aspect angle. In tumble, the area is proportional to an elliptic function of the solar aspect angle which varies by a factor of only $2/\pi$ from maximum to minimum. The maximum is the same for both spinning and tumbling motions and equals the total lateral area divided by π. The recorded temperatures indicate that the area projected to the sun remained at least 30 percent larger after 6 weeks than the minimum at 2 or 3 weeks after launch.

A computer program was used for all thermal analyses on Explorer XXIII. The spacecraft was analytically divided into 26 nodes, and the 26 simultaneous heat-flow differential equations were integrated by the Runge-Kutta method. The earth thermal radiation and albedo heat sources were accounted for in the computer program.

SUMMARY

In summary, pressure-cell temperature data measured on the satellite during the first several passes show good correlation with those calculated by using Javelin flight

temperature data. No damage to the payload resulted from the initial heating from the rocket case. Data presented show that, after dissipation of this heat, all temperatures agreed well with predictions and remained well within operating limits.

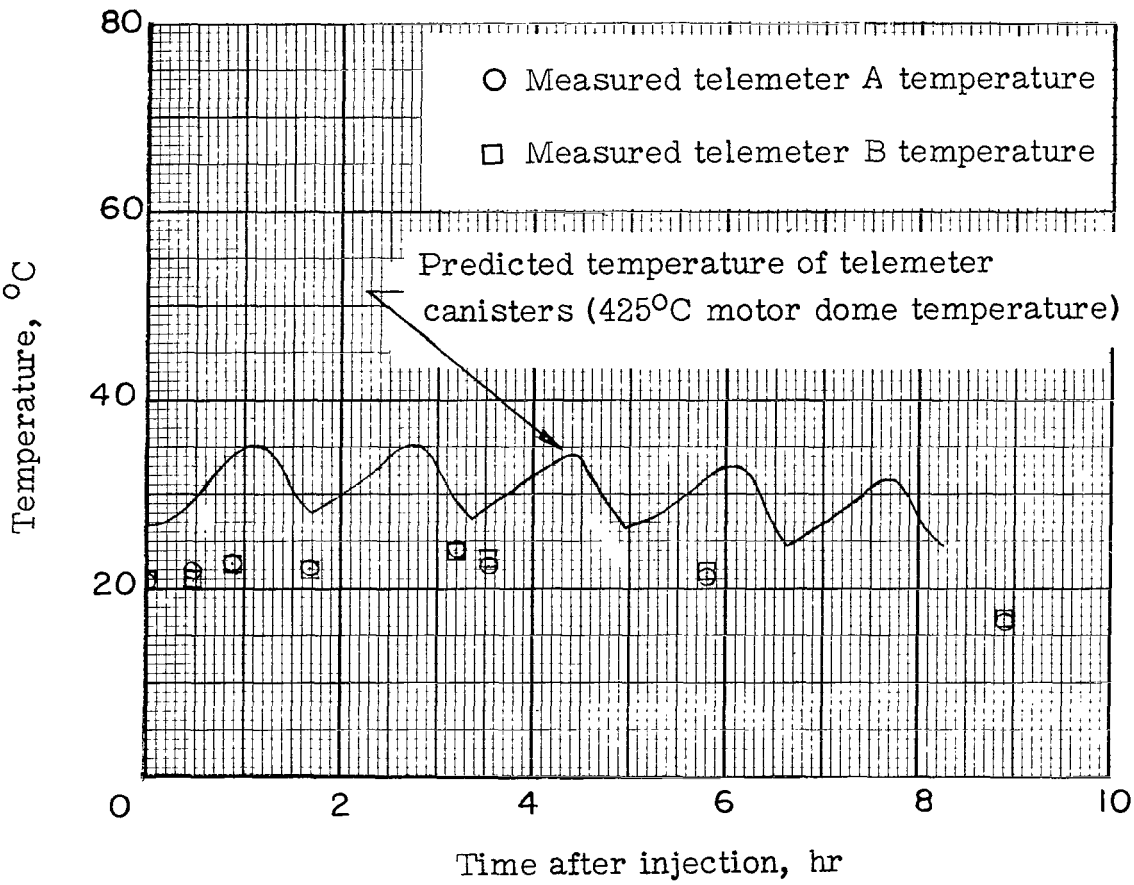

Figure IX-1.- Predicted and measured telemeter temperatures showing effects of rocket-motor heating.

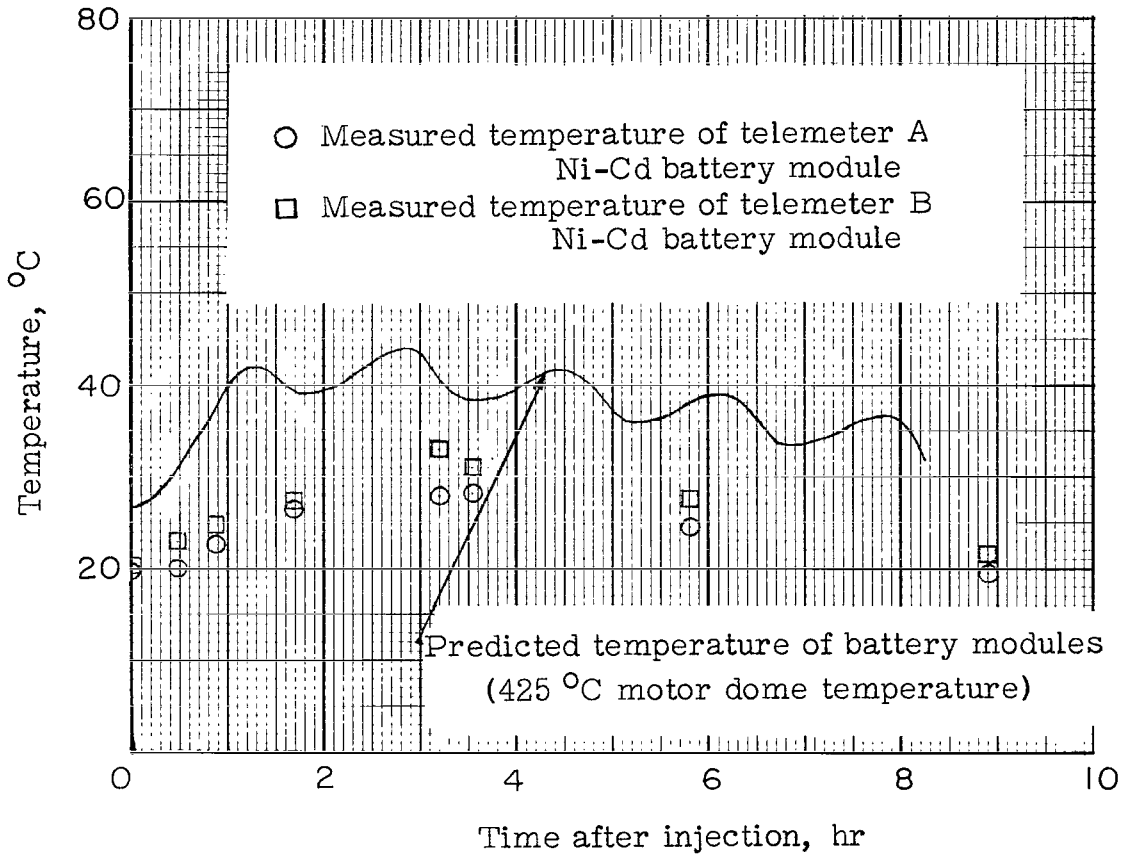

Figure IX-2.- Predicted and measured battery temperatures showing effects of rocket-motor heating.

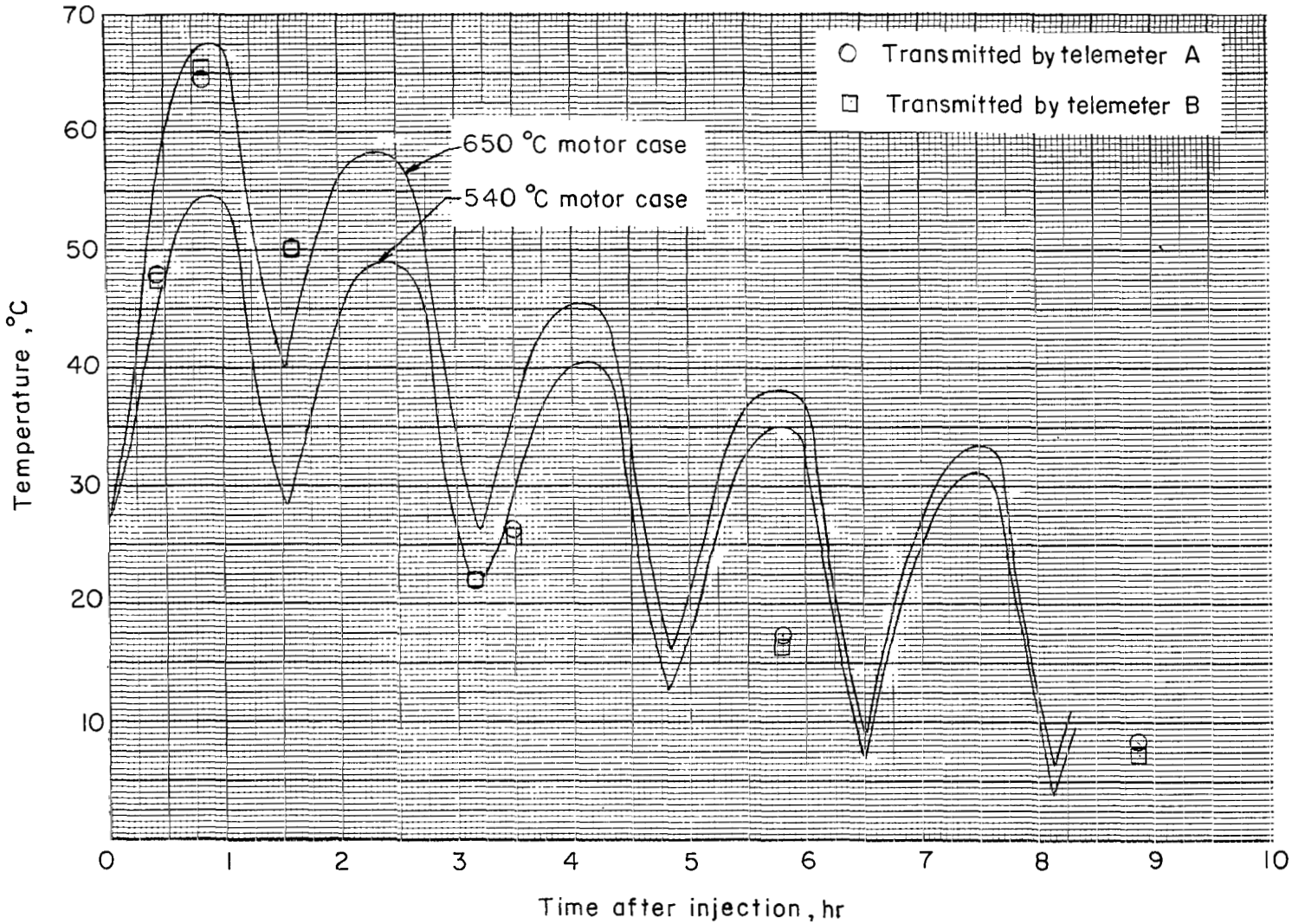

Figure IX-3.- Predicted and measured temperatures of the fourth row of pressure cells.

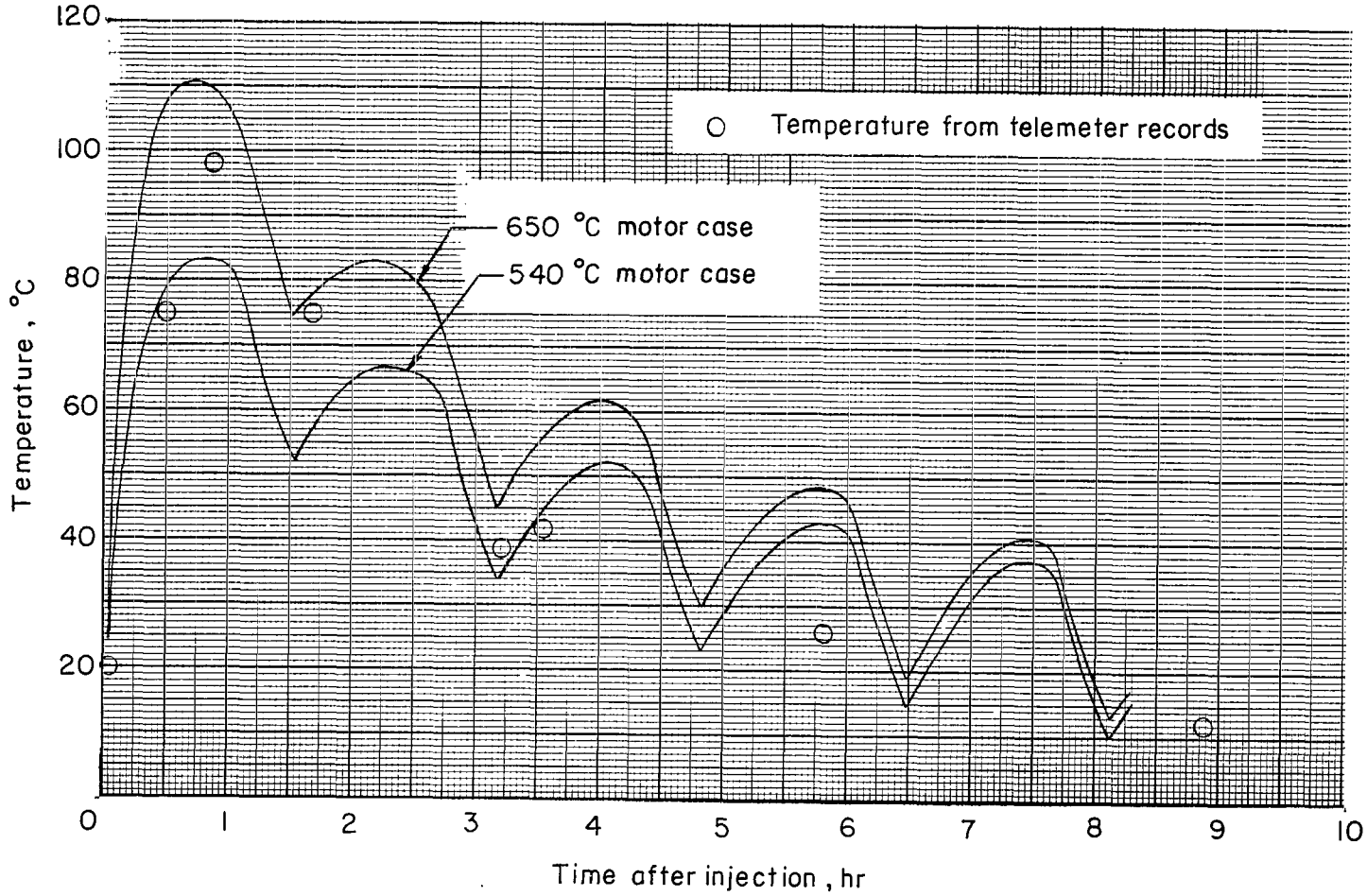

Figure IX-4.- Predicted and measured temperatures of the sixth row of pressure cells.

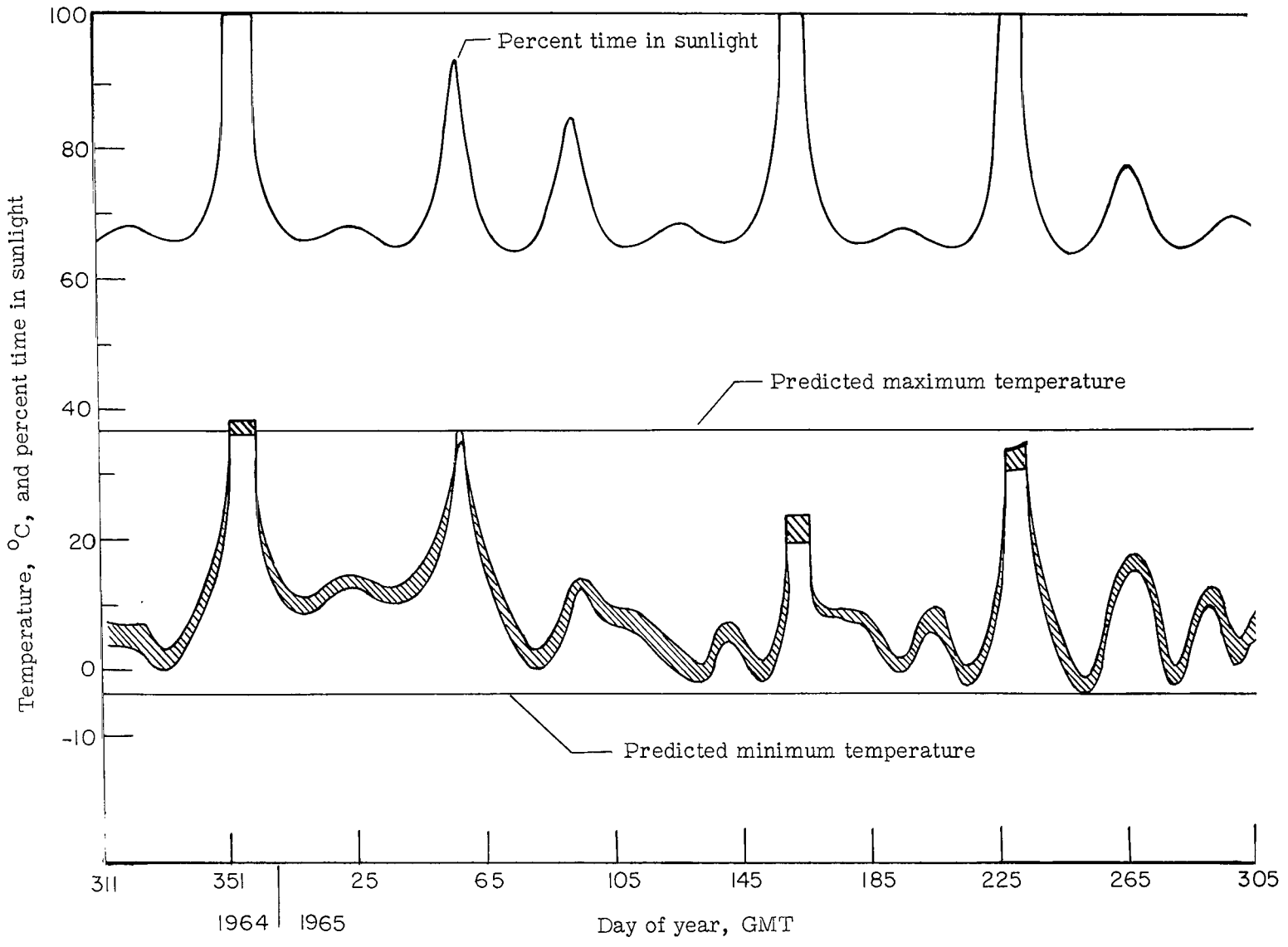

Figure IX-5.- Explorer XXIII telemeter temperatures compared with percent time in sunlight and predicted temperature limits.

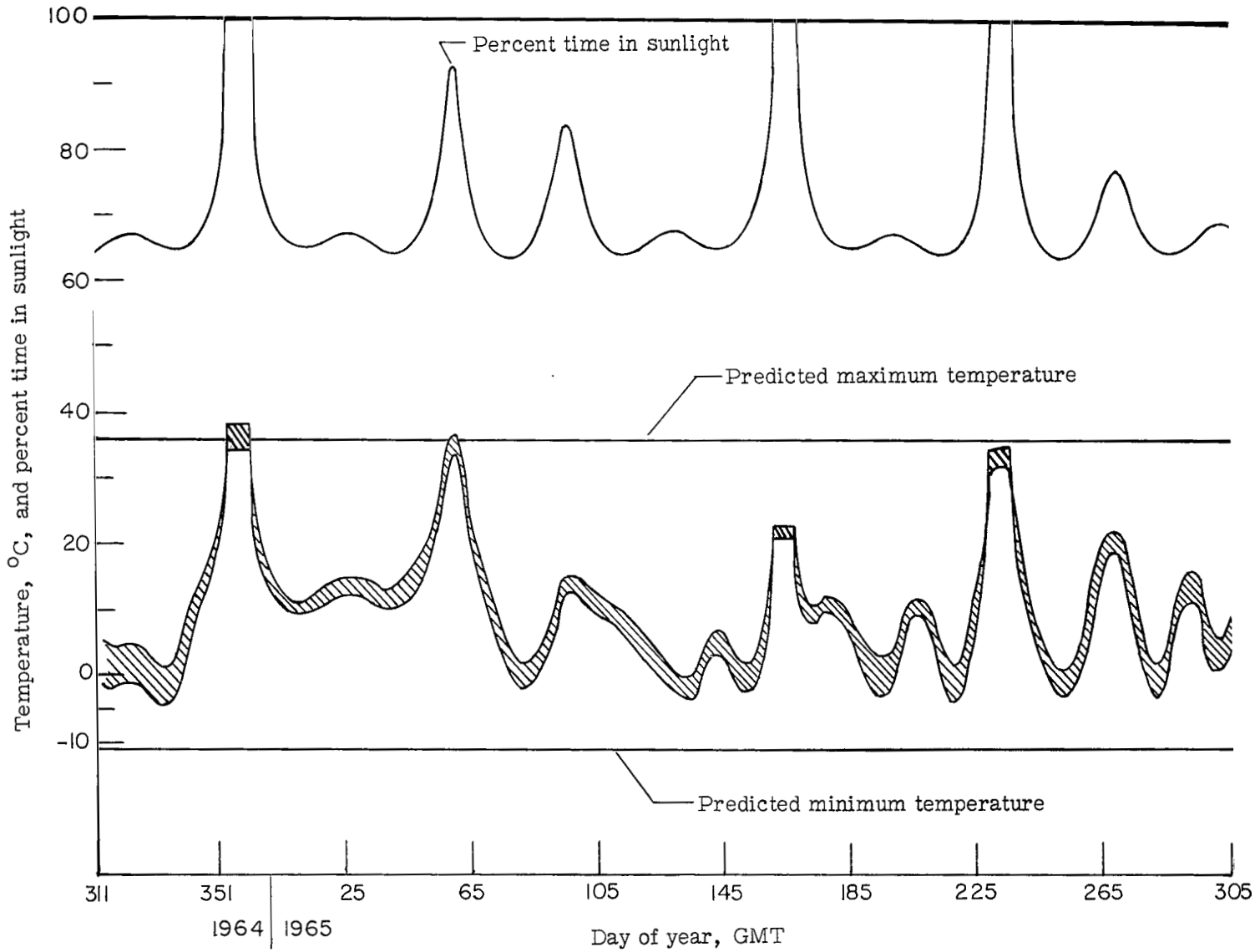

Figure IX-6.- Explorer XXIII nickel-cadmium battery temperatures compared with percent time in sunlight and predicted temperature limits.

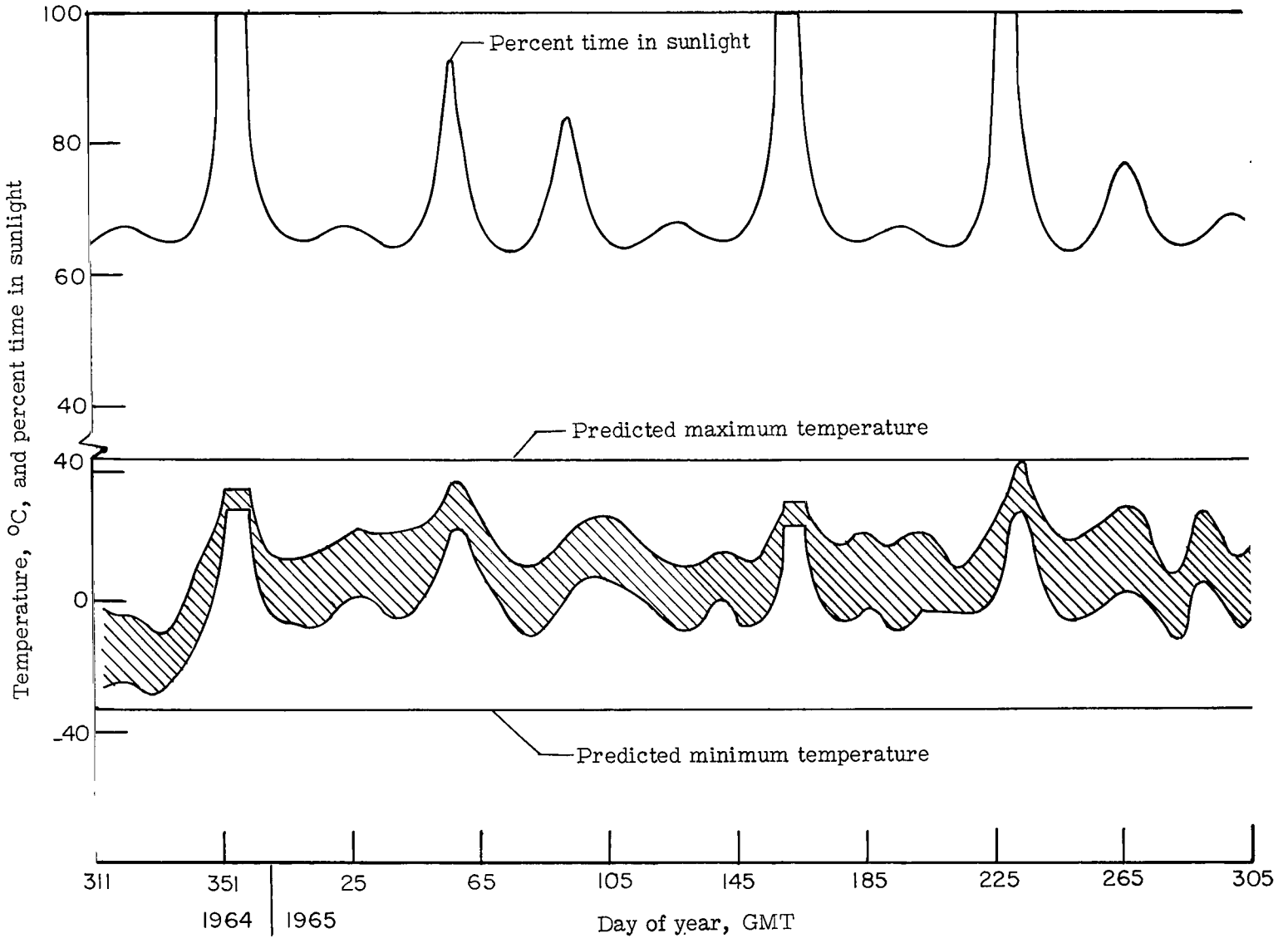

Figure IX-7.- Explorer XXIII pressure cell temperatures compared with percent time in sunlight and predicted temperature limits.

X. TELEMETRY SYSTEM

By Leon V. Taylor
Langley Research Center

DESCRIPTION

The telemetry system for the Explorer XXIII consisted of two separate and independent telemeters for telemetering data and of a radio beacon for initial tracking of the satellite. The various sensors were divided into two groups as nearly equal as possible and were telemetered separately. Any given sensor was connected to only one system so that the same piece of information was telemetered only once, but the division was made so that the same types of information were transmitted by both systems. Accordingly, if one telemeter failed, the subsequent data from each experiment would be approximately halved. The telemetry system was in two pressurized canisters mounted on a bulkhead inside the nose section of the spacecraft.

The two telemeters were of the data-storage, command-readout type, wherein data were collected during orbit and read out when within range of a Space Tracking and Data Acquisition Network (STADAN) station. Data readout was nondestructive so that noisy receptions could be discarded and the data obtained by later readouts. It was necessary to use two-frequency links for data transmission, but only one frequency, which was common to both command receivers, was used for commanding the readout.

The two telemeters were constructed as independently as possible. Separate solar cells and batteries were used to supply power to each telemeter. Redundancy was provided in the command system by connecting the two command receivers so that either command receiver could turn on both telemeters. A common antenna system was used for both telemeters. However, the two telemeters were electrically isolated by a hybrid junction.

A block diagram of the telemetry system is shown in figure X-1. The pertinent characteristics of the telemetry system are presented in the following table:

Telemetry-system component	Type	Emission	Frequency, MHz	Power output, mW	Life-time, days	Power supply
Telemeter A	Pulse-duration modulation – frequency modulation – amplitude modulation; 48 channels	30A9 for 1 minute, upon interrogation only	136.080	500	365	Secondary batteries (Ni-Cd) recharged by solar cells
Telemeter B	Pulse-duration modulation – frequency modulation – amplitude modulation; 48 channels	30A9 for 1 minute, upon interrogation only	136.860	500	365	Secondary batteries (Ni-Cd) recharged by solar cells
Radio beacon	Master oscillating power amplifier	0A0	136.860	150	7	Primary batteries (Hg)

OPERATIONAL RESULTS

Telemetry data taken before and after launch indicate that the telemetry system performance after injection into orbit was satisfactory and that all sensors except the cadmium sulfide sensors were operating. Telemetry data recorded by Antigua, British West Indies, just after injection into orbit at 12 hours 11 minutes 37 seconds GMT (T + 9 minutes 36 seconds) indicate that both cadmium sulfide sensors were saturated with light.

The telemetry system of both telemeters operated satisfactorily for a period of over 1 year in a near-earth orbit without loss of any data channels. There was no measurable degradation over the 1-year period in either of the two telemeter systems or their power supply systems. The only area (to be discussed subsequently) in which a problem was experienced, the antenna system, caused no significant loss of data.

A special station was set up at Antigua to interrogate and record data at insertion in order to establish a zero reference for all sensors. From received-signal-strength records made at Antigua, it was determined that spin-up of the Scout fourth stage occurred at 12 hours 10 minutes 45.8 $\pm$ 1 seconds GMT and the spin rate was 144 $\pm$ 1 rpm. Spin rate after fourth-stage burnout was 150 $\pm$ 1 rpm.

The radio beacon used to facilitate tracking was designed to operate for a minimum of 7 days. Reports from STADAN indicated that the beacon was still usable but very weak on the 12th day after launch, November 18 (day 323 GMT), 1964. Johannesburg, Republic of South Africa, reported that there was no beacon at 12 hours 13 minutes GMT on November 20 (day 325 GMT), 1964.

Received-signal-strength records from STADAN indicate signal strengths were from -88 to -130 dBm with most of the recordings from -90 to -100 dBm (where dBm is the power ratio in decibels in which the reference power is 1 milliwatt). Automatic data analysis required a signal strength greater than -110 dBm.

A total of 1521 interrogations of Explorer XXIII were scheduled for STADAN during the period from launch until 24 hours GMT on November 5 (day 309 GMT), 1965. A breakdown of the interrogations that were of sufficient quality to allow transmissions to be processed is as follows: (1) transmissions were totally processable in 53 percent of the scheduled interrogations; and (2) transmissions for at least one of the telemeters were processable in 72 percent of the interrogations (the loss of processable transmissions for the remaining 28 percent can be attributed to spacecraft antenna degradation, station errors, and errors in processing data, but some of the nonprocessable transmissions could have been recovered by hand reducing the raw transmissions, had it become necessary).

Data listings analyzed through November 5 (day 309 GMT), 1965, indicate that telemeter performance was still satisfactory. Figures X-2 and X-3 are plots of telemeter nickel-cadmium (Ni-Cd) battery temperature and voltage and of telemeter temperature. Each band represents the upper and lower limits measured for the respective function. The telemeter temperatures remained within system calibrations, -10° C to 50° C, and roughly followed the profile of spacecraft percentage time in sunlight. The decrease in battery voltage with increasing battery temperature was normal. No measurable degradation in battery voltage had occurred through November 5 (day 309 GMT), 1965.

During the first 5 days in orbit, reports were received from STADAN that spurious data transmissions were occasionally being received from Explorer XXIII. The spurious transmission in some instances was only one transmission from one telemeter. In other instances, it consisted of multiple interrogations from both telemeters. These spurious transmissions continued throughout the experimental life of Explorer XXIII. Because of the automatic turnoff system built into the satellite and the overcapacity of the power supply system, these interrogations did not adversely affect the operation of the satellite. These spurious interrogations are attributed to the spurious response modes of the command receivers and the lack of an integration circuit on the tone detectors.

Data recordings taken on orbit 82 (November 12 (day 317 GMT), 1964), on orbit 273 (November 25 (day 330 GMT), 1964), and on orbit 287 (November 26 (day 331 GMT), 1964) indicated that severe crosstalk (10 to 50 percent) from telemeter A was appearing on telemeter B. Also present were unusually deep nulls (10 to 30 decibels) in received-signal-strength records analyzed. For all three orbits the crosstalk and deep nulls were present only during those orbits and not in the interrogations that immediately followed. However, during later orbits the crosstalk and nulls reappeared and remained. The crosstalk on telemeter B was only present in certain portions of the received signals and was only 5 to 10 percent in amplitude of the received signal. The nulls were still 10 to 30 decibels and would occur once per revolution of the spacecraft. The nulls and crosstalk are thought to be the result of an intermittent fault in the antenna system (either in the hybrid junction or the antennas themselves) which later reappeared and remained. Similar nulls and crosstalk were duplicated on the prototype spacecraft by inducing any of several faults in the antenna systems. The effect of crosstalk and nulls resulted in a small percentage of transmissions that could not be automatically processed.

The telemeter A canister lost pressurization between January 17 (day 017 GMT), 1965 and January 18 (day 018 GMT), 1965, after 72 or 73 days in orbit. The loss of pressurization did not affect the operation of the telemeter. Telemeter B still indicated canister pressure on November 5 (day 309 GMT), 1965.

Explorer XXIII was equipped with a 1-year termination switch. The switch was scheduled to operate on October 29 (day 302 GMT), 1965 $\pm$ 4 days. Data transmission was

still being received from Explorer XXIII as late as December 31 (day 365 GMT), 1965, when STADAN was requested to cease normal interrogations. It was not possible to determine the reason for the failure of the termination switch to operate.

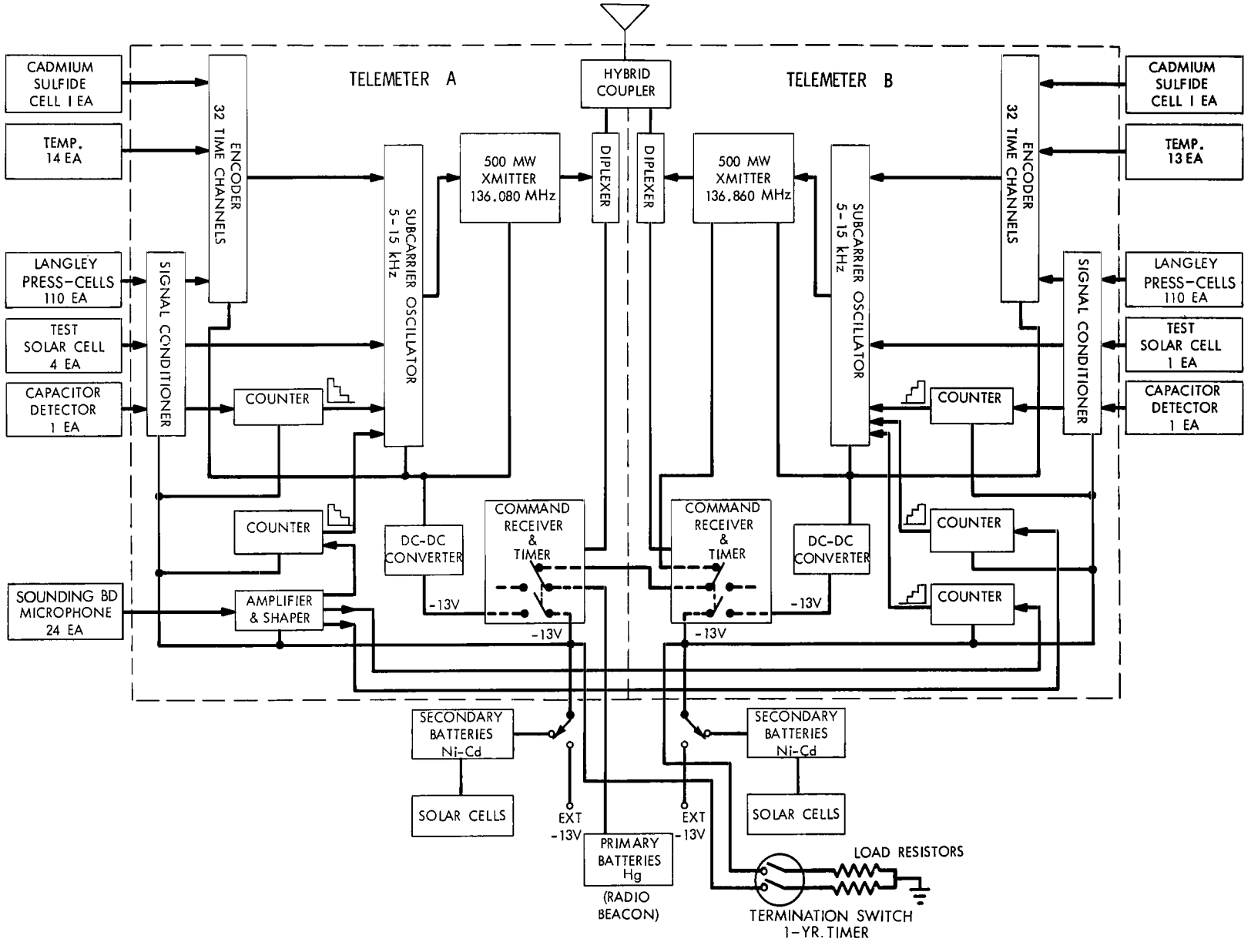

Figure X-1.- Block diagram of telemetry system.

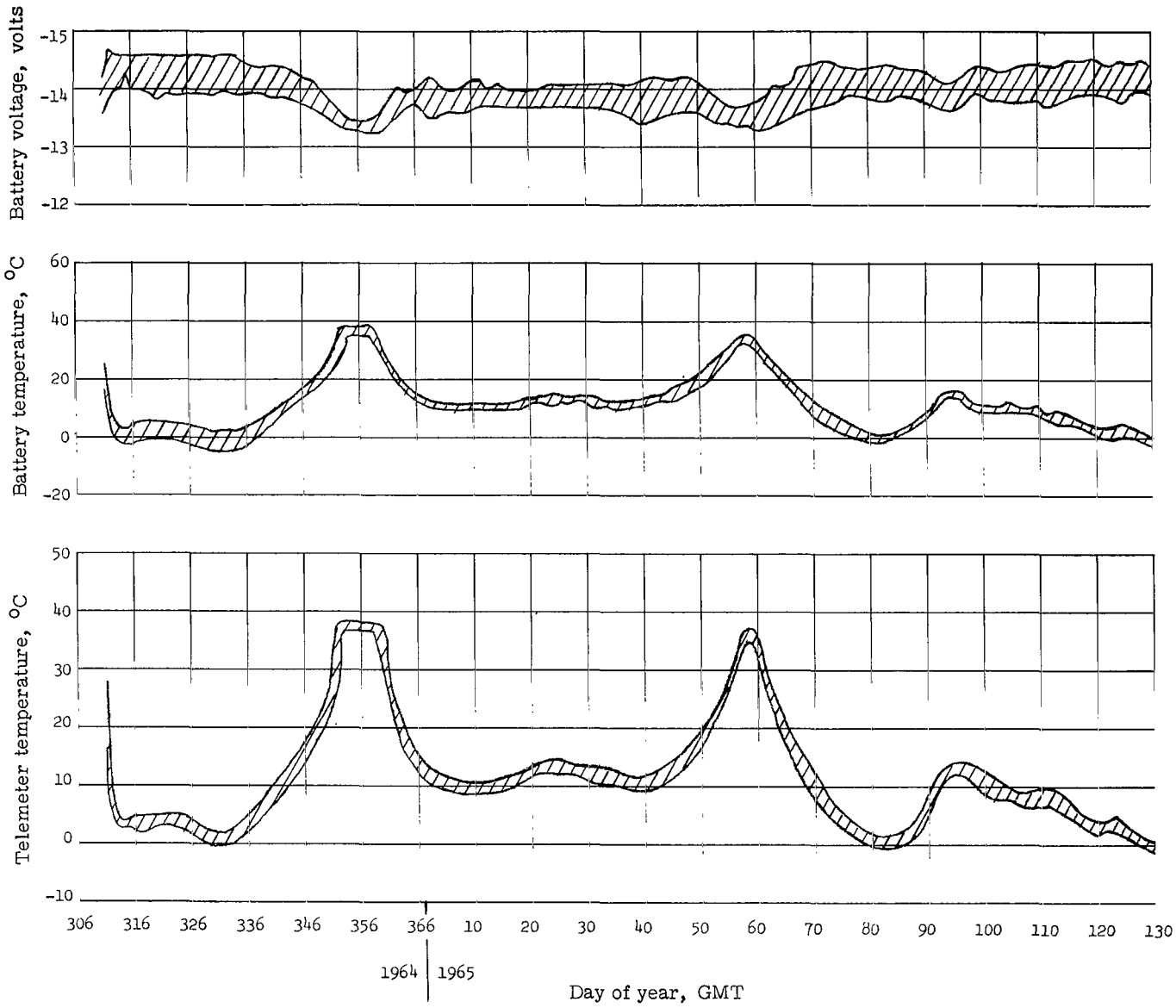

Figure X-2.- Nickel-cadmium battery voltage and temperature and telemeter temperature for telemeter A.

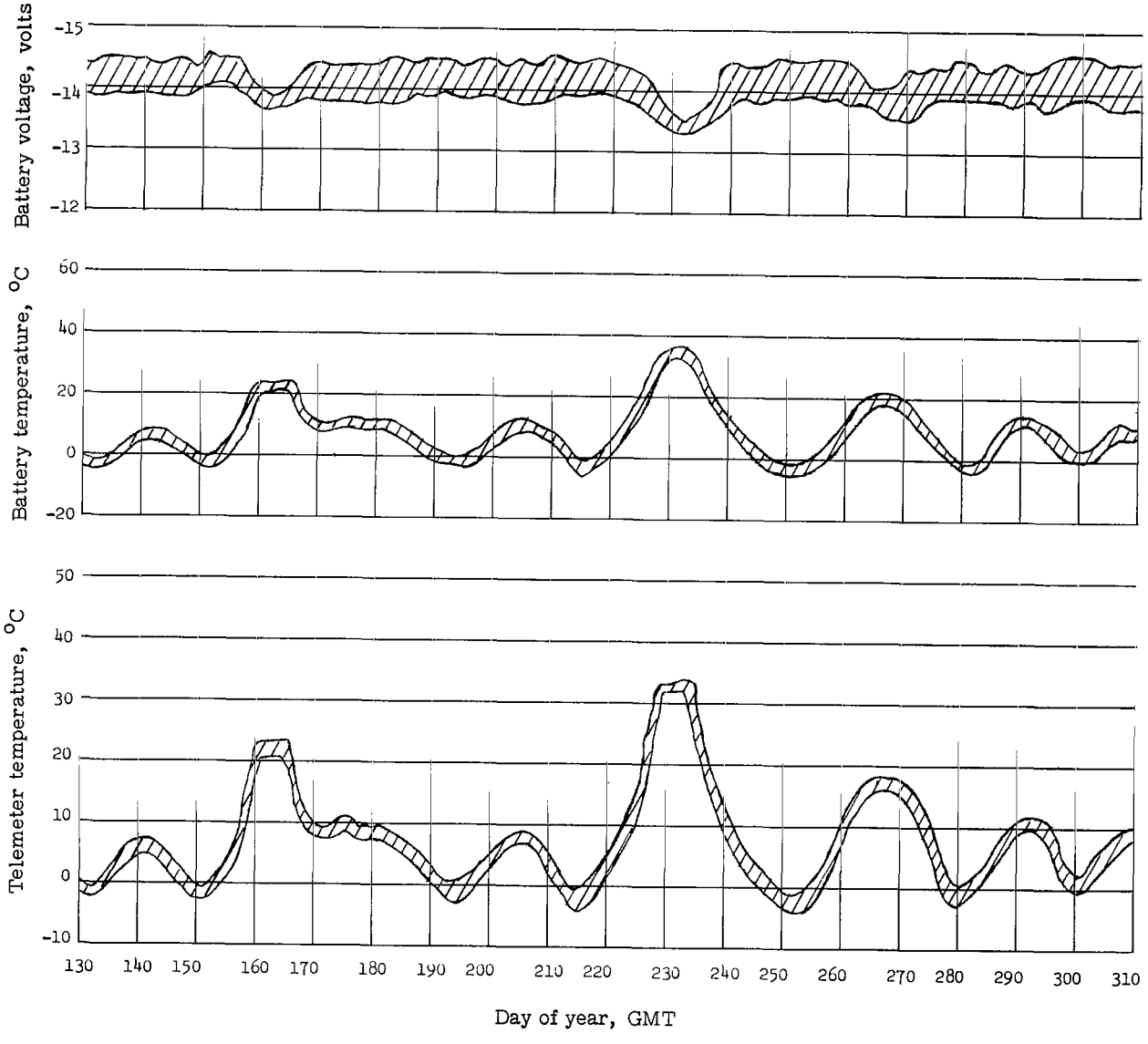

Figure X-2.- Concluded.

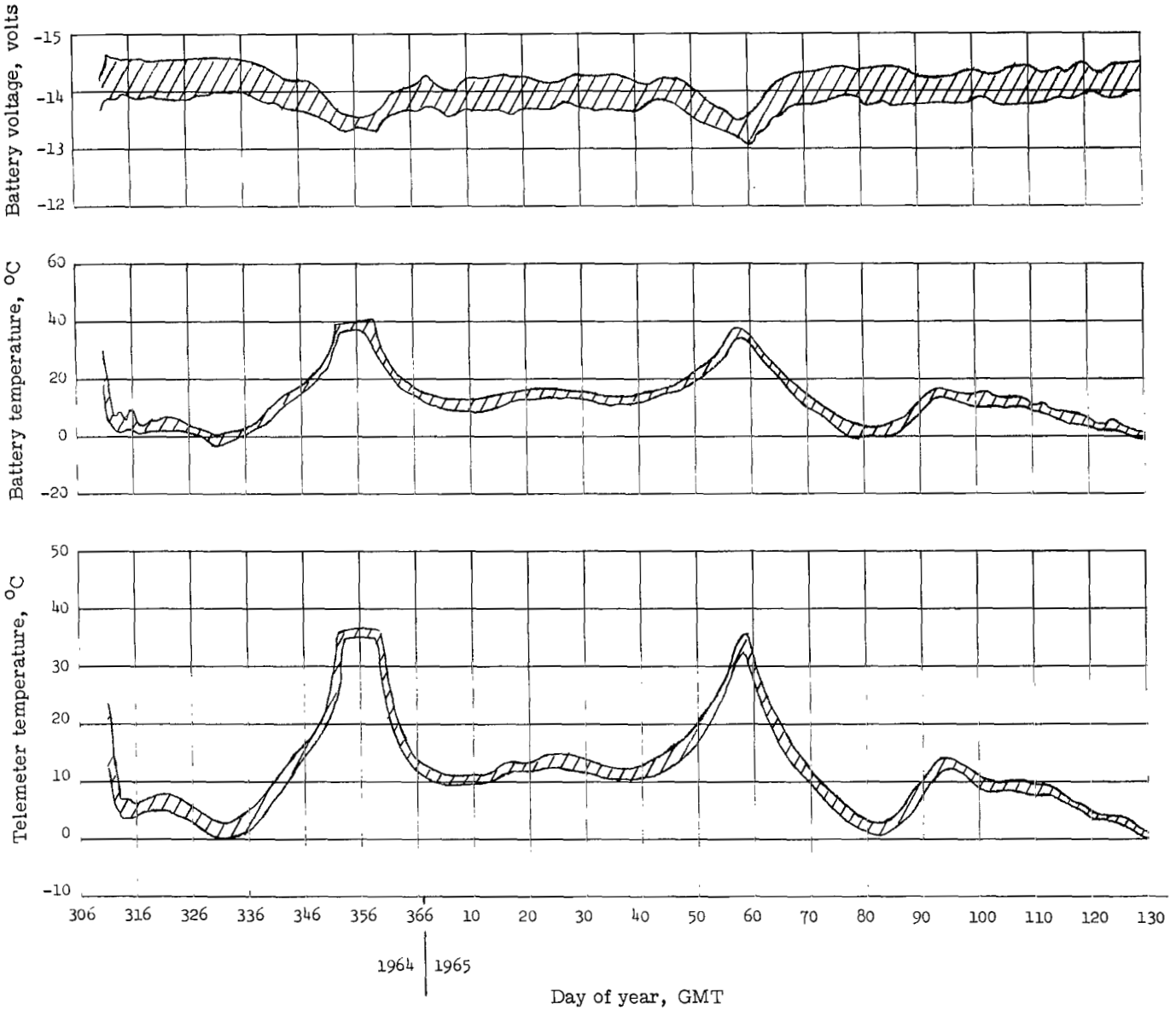

Figure X-3.- Nickel-cadmium battery voltage and temperature and telemeter temperature for telemeter B.

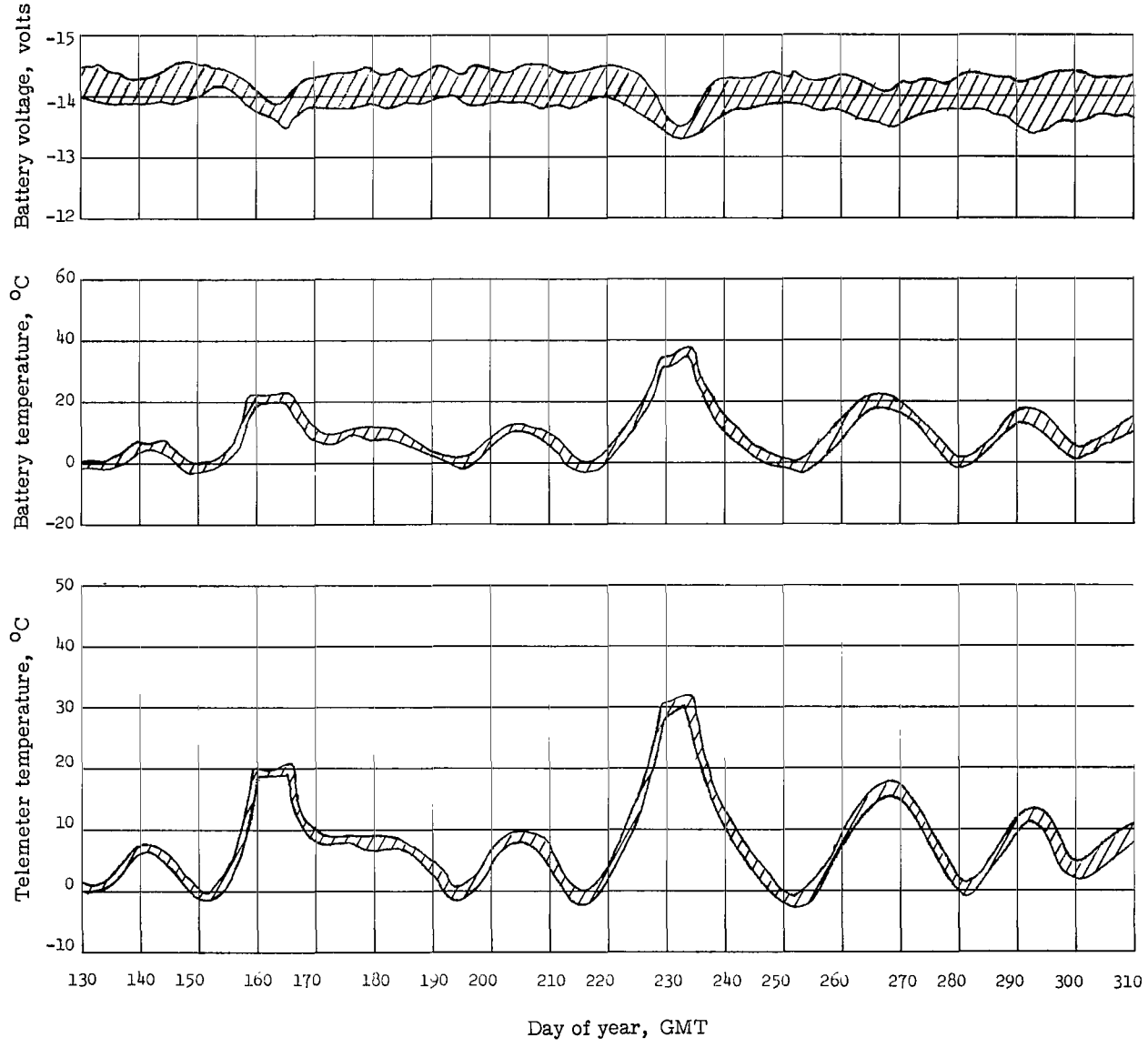

Figure X-3.- Concluded.

"The aeronautical and space activities of the United States shall be conducted so as to contribute . . . to the expansion of human knowledge of phenomena in the atmosphere and space. The Administration shall provide for the widest practicable and appropriate dissemination of information concerning its activities and the results thereof."

—NATIONAL AERONAUTICS AND SPACE ACT OF 1958

NASA SCIENTIFIC AND TECHNICAL PUBLICATIONS

TECHNICAL REPORTS: Scientific and technical information considered important, complete, and a lasting contribution to existing knowledge.

TECHNICAL NOTES: Information less broad in scope but nevertheless of importance as a contribution to existing knowledge.

TECHNICAL MEMORANDUMS: Information receiving limited distribution because of preliminary data, security classification, or other reasons.

CONTRACTOR REPORTS: Scientific and technical information generated under a NASA contract or grant and considered an important contribution to existing knowledge.

TECHNICAL TRANSLATIONS: Information published in a foreign language considered to merit NASA distribution in English.

SPECIAL PUBLICATIONS: Information derived from or of value to NASA activities. Publications include conference proceedings, monographs, data compilations, handbooks, sourcebooks, and special bibliographies.

TECHNOLOGY UTILIZATION PUBLICATIONS: Information on technology used by NASA that may be of particular interest in commercial and other non-aerospace applications. Publications include Tech Briefs, Technology Utilization Reports and Notes, and Technology Surveys.

Details on the availability of these publications may be obtained from:

SCIENTIFIC AND TECHNICAL INFORMATION DIVISION

NATIONAL AERONAUTICS AND SPACE ADMINISTRATION

Washington, D.C. 20546